Real-Time 3D Characterization of Antenna Systems

MSc Thesis

F.A. Musters

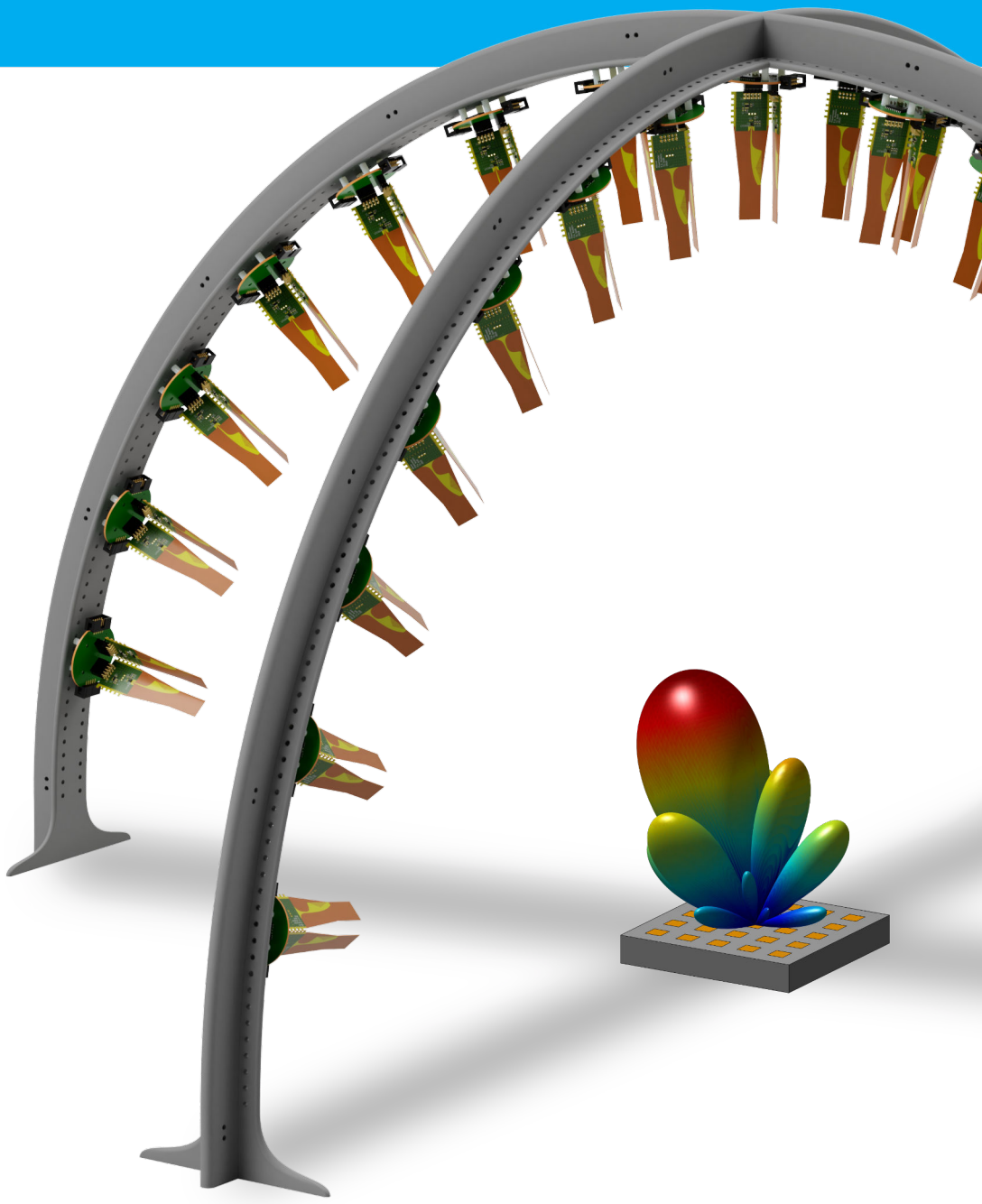

TU Delft

Real-Time 3D Characterization of Antenna Systems

Master Thesis

by

F.A. Musters

to obtain the degree of Master of Science in Electrical Engineering,
track Microelectronics, specializing in RF/Wireless Design,
at the Delft University of Technology,
to be defended publicly on Thursday August 29, 2019 at 14:00

Student number:	4460685	
Project duration:	September 3, 2018 – August 29, 2019	
Thesis committee:	Prof. dr. E.W. McCune Jr.	Full Professor, ELCA, TU Delft, supervisor
	Dr. M. Spirito	Associate Professor, ELCA, TU Delft, supervisor
	Dr. ir. M.A.P. Pertijs	Associate Professor, EI, TU Delft

TU Delft

NXP

Abstract

The recent development of commercial phased array antennas for 5G at mm-wave frequencies (20 GHz to 60 GHz) introduces new challenges for radiation pattern characterization. Since these systems aim to employ active beamforming to steer the datastream to specific users, a single base station should be capable of deploying multiple beams simultaneously and electronically steer them to track the user. This introduces the need to characterize a large set of parameters and configurations.

As these modules become more cointegrated with the underlying transceiver chain, its internal moduls are becoming less accessible and the device should be considered a unique black box for characterization purposes. Since the difficulty of sub-component testing increases, verifying antenna systems must be performed in an over-the-air (OTA) setup for the entire module.

Current antenna characterization utilizes a single probe, which relies on mechanical rotation to move the sensor around the antenna under test (AUT). This is a proven method, but typically takes several hours, depending on the required resolution. This becomes tedious and commercially unaffordable when multiple measurements are required. Furthermore, these systems require additional instruments, e.g. a vector network analyzer (VNA), which significantly increases the cost of the setups.

The concept proposed in this work avoids these drawbacks. It employs a large number of fixed sensing elements, enabling real-time radiation pattern acquisition. This has the potential to significantly reduce measurement time of 5G antenna systems. A key factor is the sampling of the signal right at the antenna probe, in contrast to the expensive VNA commonly used. This results in a lower complexity and cost, since there are significantly less high frequency components compared to other setups.

A prototype of this concept has been developed for two cross-sections of a dome, which provides real-time antenna pattern tracking capabilities. The high level of flexibility allows easy adaptation to different antenna systems. The sensing probes provide direct downconversion at the antenna, eliminating the need for a VNA. Furthermore, an algorithm is made that calculates the required number of sensor nodes depending on the antenna system under test. The high speed, modularity and low cost allow this setup to be an effective option for instantaneous verification of beam-steer capable antenna systems in the development and fabrication. This can ease the predicted antenna measurement bottleneck expected for the broad employment of small-cell 5G networks. The concept can be expanded to include features such as jammer injection and instantaneous error vector magnitude (EVM) measurement.

Keywords: *Antenna array, characterization, millimeter wave measurement, multiple-input–multiple-output (MIMO), over-the-air (OTA) testing, multiprobe, 5G*

Preface

This thesis displays the research performed on a new method to characterize antenna radiation patterns with the use of a static multi-probe measurement array. It is executed in the nominal period of a full acacdemic year.

The topic for my thesis found its roots with supervisor Earl McCune. He noticed that companies are limited by the current over-the-air measurement techniques used in typical antenna development. The time and money required to perform this are very high, considering the rise of products with the expected 5G NR (new radio) revolution in mobile communication. He proposed to get rid of all moving parts involved in these measurements and make use of a completely static setup by employing many measurement probes, with the ultimate goal to measure radiation patterns in seconds instead of hours.

This concept immediately grabbed my attention and it was not much later that I started to dive in this topic. The integration of multiple disciplines within the electronics field has always fascinated me. This, in combination with the practical aspect of realizing a physical setup was enough reason for me to make this the concluding work of my masters degree.

And this choice turned out to be very worthwhile. I had a great time during the analysis, design and realization of this concept. The good balance of freedom and guidance at the TU Delft allowed me to give my own twist to the implementation. In this process, I have learned about many aspects of the RF engineering spectrum. This ranges from fundamentals such as phased array systems to measurement techniques and antenna design. Furthermore, I faced a lot of challenges which required me to plan and execute proper engineering approaches. These include semi-mass production of powermeter sensor design, custom PCB designs, realizing an effective communication protocol and even 3D printing.

I am very happy to claim that the proposed goal is reached by the delivery of a fully operating prototype. A setup capable of measuring radiation patterns within a second is shown in this report. Obviously, in this process some well-considered trade-offs were made to realize the prototype within the given time frame. Nevertheless, this concept has great potential to revolutionize over-the-air testing speed of antenna systems.

With this report, I would like to show you two things: why this work is good enough to obtain my masters degree and the added value of this project to the scientific community. In writing this document, I have carefully considered which parts should be included to convey both messages properly. I hope you find as much pleasure in reading this report as I had realizing it!

Ferry Musters

Delft, August 2019

Acknowledgments

First of all, I would like to thank the Delft University of Technology for granting me the opportunity to study here and follow my passion. The freedom of education has always been very important to me and preserving this will remain a high priority for me. The completion of this thesis could not have been possible without the support of many people. I would like to thank the following people in specific:

I would like to express my gratitude to prof. dr. Earl McCune, dr. Marco Spirito and MSc Satoshi Malotaux for their supervision and feedback throughout the project. The opportunities you gave me have enabled me to learn many new skills and further develop myself as an RF engineer. Of course, I also would like to thank my fellow students and many friendly colleagues at the ELCA department of EEMSC, for both the technical support and the casual talks. Furthermore, I want to thank dr. Ulf Johannsen and Ad Reniers from TU Eindhoven for the use of their antenna measurement setup and the support during the probe development. Also, I would like to thank NXP Semiconductors for financially supporting me throughout the project.

Lastly, but perhaps the most important, I am grateful for my family and friends who have supported me during the project. In particular, the care, encouragement and advice my girlfriend Esther gave me were a big motivation for me to keep working.

Contents

1

Introduction

In recent years, the amount of wireless data communication has been growing rapidly. Cisco's latest Visual Networking Index (VNI) reports that *"Globally, mobile data traffic will increase sevenfold between 2017 and 2022"* [1]. Therefore, the current 4G LTE standards will soon reach their limit [2]. One of the proposed solutions for 5G is to increase throughput by the use of millimeter wave (mm-wave) frequencies, i.e. above 24 GHz, as these bands are less occupied and offer larger bandwidths, as bandwidth tends to be proportional to the carrier frequency [3]. An property of these increased frequencies is high signal decay, which results in lower coverage. Therefore, there is a desire for more gain in the transmitter and receiver chain, such that this path loss is compensated. Actively amplifying the signal goes paired with increased energy consumption, which is not only expensive in terms of power usage, but also requires more thermal management. Therefore, achieving several decibels of passive gain in the antenna by making it more directive enables the transmission of power to where it is actually needed.

To achieve this directivity, the concept of beamforming is being implemented; instead of sending out a signal in all directions, a narrow directive beam focuses the transmitted power more efficiently to a specific user, as shown in Fig. 1.1. By employing beamsteering and -tracking, the beam is electrically steerable such that it is aimed towards the receiver. This technique has mostly been applied in military and scientific fields [4–7], but is now finding purpose in commercial applications. To serve many users, multiple independent beams are created in parallel to increase frequency reuse [8].

Currently, the dominating technique in literature to realize beamforming in multi-user communication systems, e.g. 5G, is the use of phased array antennas [9–11]. These consist of an array of (patch) antennas which are each exited with a controlled relative phase shift. An example of this is shown in Fig. 1.2. The signals constructively add up in a specific direction, which results in a more directive (i.e. higher gain) antenna. These devices are more time-consuming to develop as the close proximity re-

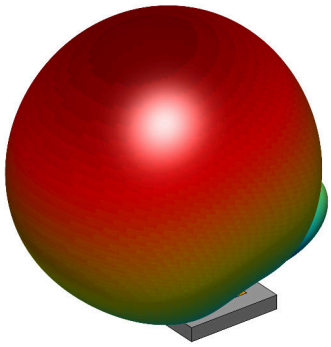

(a) Example of an antenna with broad coverage. Since this angle is very wide, a receiver is almost always within range.

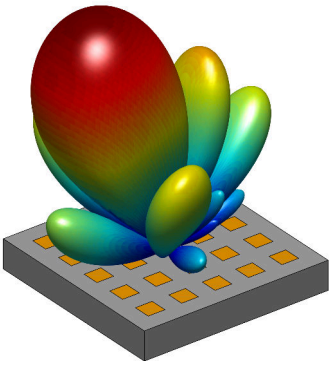

(b) Example of a radiation pattern of an antenna with beamforming capabilities. The beam is controllable to various angles, such that the receiver always receives a strong signal.

Figure 1.1

Figure 1.2: Example of a phased array antenna for 5G applications. Currently being developed at TU Eindhoven.

sults in cross coupling between antenna elements. This coupling gives rise to an injected reverse-flow current into the neighboring points, which is visible as a load impedance change. This results in non-linear distortion and thus non-optimal performance. Furthermore, the implementation of beamsteering allows for many possible configurations for the system. Since these systems will become mass produced consumables, verification for a fraction of the cost compared to custom-built systems is needed. And thus, the wireless community is expecting a measurement bottleneck to arise as more and more systems will come into commercial use and need to be tested [12].

Many of these properties are measured by characterizing the radiation pattern. The typical method of measuring antenna radiation patterns involves setting up an RF anechoic chamber with a single probe scanning at every angle, which results in a measurement time of approximately half a day and therefore limiting device characterization to only one measurement. Examples of these systems are shown in Fig. 1.3. Upcoming modern antenna systems typically have many parameters to be verified (e.g. various beam steering angles, null pattern shifting). Therefore, a faster characterization improves the development time and verification quality of these systems, while reducing cost due to shorter occupancy.

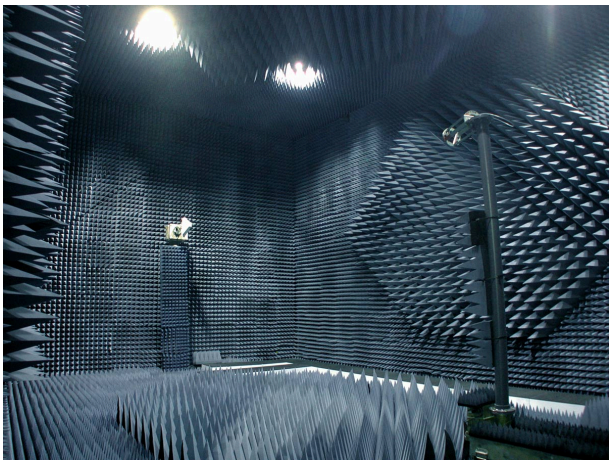

(a) A typical anachoic chamber setup. In practice, either the transmitting or transmitting antenna rotates over all angles with motors. Source: [13]

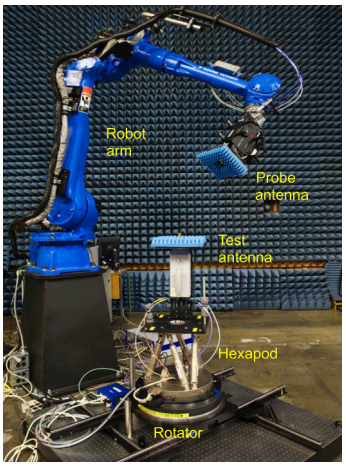

(b) A high end robot arm setup to characterize radiation patterns. Source: [14]

Figure 1.3: Two setups used for characterization of antennas, both using rotating components.

1.1. Application

The focus of this project is to develop a system that allows for rapid antenna system characterization to partly alleviate the expected mm-wave antenna characterization bottleneck. Therefore, the antenna under test (AUT) systems of interest are phased array antenna systems which are currently being developed for the fifth generation new radio (5G NR) standard, specifically the mm-wave frequencies indicated by Frequency range 2 (FR2). These systems use frequency bands in the range of 24 GHz to 60 GHz and directive beams, i.e. more than 10 dBi. The proposed setup offers an alternative to setups such as shown in Fig. 1.3.

1.2. Deliverable

A measurement system is investigated and realized which significantly increases the characterization speed of antenna measurements to partly mitigate the expected 5G testing bottleneck. The aim of this thesis is to study the feasibility of realizing a faster, cheaper and modular method of characterizing complete antenna systems. The focus lies on measuring in seconds instead of hours. To achieve a functioning concept within the available time frame, some practical choices are made to minimize complexity while proving the working principle.

The measurement speed of traditional setups is limited by the physical scanning of the probe. Therefore, this project investigates the effectiveness of omitting any moving parts by using a static array of probes. The proposed concept aims to measure the whole antenna (sphere or half sphere) at once, using an array of optimally spaced high speed direct downconverters.

To minimize cost of the setup, a stand-alone system is desired, which requires no additional instruments such as a vector network analyzer (VNA). Modern phased array signal generation and transmitting is being integrated into a complete solution [12]. It is preferred to measure without having access to the inner signal feeds. By designing the setup with a high degree of modularity, the measurement

setup is easily adapted and allows for characterization of different antenna systems. This is possible by changing the number of spatial sampling points and receiver front-ends.

1.3. Document Structure

The organization of this thesis is as follows: chapter 2 introduces all the antenna concepts which are used in this work and proceeds to provide an overview of the current state-of-the-art in antenna measurements. After this, After that, chapter 4 shows the development of a suitable sensing probe. These are used to build the full measurement setup, as discussed in chapter 5. Finally, the conclusion in chapter 6 reflects on the achieved milestones and proposes further improvements.

2

Antenna System Characterization

This chapter introduces the key concepts which establish the theoretical framework needed to understand the challenges for the developing an rapid antenna measurement setup. The fundamental properties of antenna operation are reviewed, reasoning from the physics of propagating waves. After this, commonly used measurement setups for antennas are discussed. To conclude this chapter, several examples of AUTs for this project are discussed.

2.1. Antenna Radiation

An antenna is a component which transfers electromagnetic energy from waves in a guided medium to free-space or vice versa, as visualized in Fig. 2.1. After transmitting, these waves propagate the transmitted power in a given directions. This directionality is always compared to the theoretical isotropic antenna, which is perfectly omnidirectional. This serves as the comparative reference for any antenna [15]. Since an isotropic antenna spreads out transmitted waves in all directions, the surface of a sphere with area $A = 4\pi R^2$ contains all the energy at a given distance. Thus as the distance R increases, the transmitted power P_T in watts is distributed over a larger area. This results in power intensity $W_{isotropic}$ of

$$W_{isotropic} = \frac{P_T}{4\pi R^2} \quad \left[\frac{\mathrm{W}}{\mathrm{m}^2}\right]. \tag{2.1}$$

From this, it follows that through a physical spherical surface A_{phys} at distance R, the observed power level P_o is given by

$$P_o = A_{phys}\frac{P_T}{4\pi R^2} \quad [\mathrm{W}]. \tag{2.2}$$

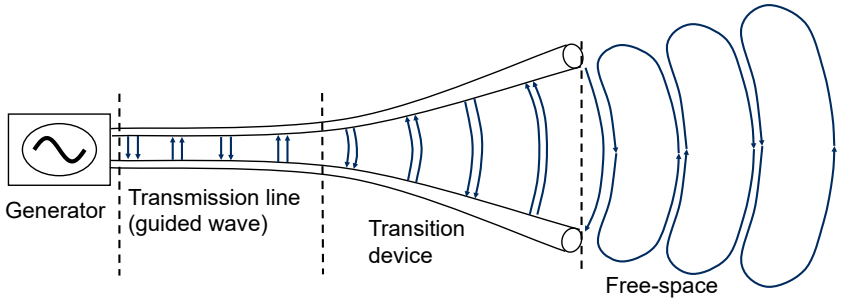

Figure 2.1: Basic function of an antenna.

In practice, an antenna never radiates all its energy equally. Therefore, the radiated signal is dependent on the spherical coordinates (θ, ϕ) such that the power density of Eq. 2.1 becomes

$$W(\theta, \phi) = \frac{P_T(\theta, \phi)}{4\pi R^2} \quad \left[\frac{\mathrm{W}}{\mathrm{m}^2}\right]. \tag{2.3}$$

Following the law of conservation of energy, the sum of the power available at a full sphere equals the total radiated power. This is mathematically expressed as

$$\int_{\frac{-\pi}{2}}^{\frac{\pi}{2}} \int_{0}^{2\pi} W(\theta, \phi)\, d\theta \sin(\phi)\, d\phi = P_T \quad [\mathrm{W}], \tag{2.4}$$

as stated in [15]. Since an antenna transmits stronger power levels into a specific direction, it essentially means that at some angles, the signal is stronger then at others. This power pattern is defined as the antenna gain G_A, which is calculated via

$$G_A(\theta, \phi) = \frac{W(\theta, \phi)}{W_{isotropic}}. \tag{2.5}$$

The antenna gain is defined along spherical coordinates, where the specified single value 'gain' of the antenna refers to the maximum value of the closed surface. Whenever this value is expressed on a logarithmic scale, the unit dBi is used, relative to the isotropic antenna.

Since an antenna is a passive device, the antenna gain is sometimes called passive gain. Unlike amplifier gain which adds power, passive gain describes the directivity of the antenna relative to an isotropic antenna. Equivalently, an antenna with passive gain can be considered as an isotropic antenna with a larger aperture. Therefore, the effective aperture A_e describes the apparent area at which

$$A_e = \frac{P_o}{W} = \frac{P_o}{\left(\frac{P_T}{4\pi R^2}\right)} \quad \left[\mathrm{m}^2\right]. \tag{2.6}$$

Even though the effective aperture is denoted in a physical quantity (m^2), it does not mean that a larger area is physically used. It shows that the antenna perceives a stronger signal, equivalent to an isotropic

antenna of this size. Furthermore, this leads to the definition of aperture efficiency, defined by

$$\eta_a = \frac{A_e}{A_{phys}} \tag{2.7}$$

With A_{iso} being the physical aperture of an isotropic antenna. This is found to be of value

$$A_{iso} = \frac{\lambda^2}{4\pi} \quad [\mathrm{m}^2], \tag{2.8}$$

as shown in [15]. This makes an important link to another physical property, namely the dependency on frequency f. This relates to the wavelength as $\lambda = \frac{c}{f}$ with c being the speed of light in free-space. With this new definition, another method of expressing the gain is found, being

$$G = \frac{A_e}{A_{iso}} \tag{2.9}$$

or, by substituting with Eq. 2.8

$$A_e = G\frac{\lambda^2}{4\pi} \quad [\mathrm{m}^2]. \tag{2.10}$$

It describes how much more power the antenna transmits or receives compared to an isotropic antenna. If we now consider the received power at surface A_R of a transmitting source at distance R with gain G_T, combining the previous equations yields the received power of

$$P_r = \frac{P_T}{4\pi R^2} G_t A_r. \quad [\mathrm{W}]. \tag{2.11}$$

Now, by relating the effective aperture A_r of the receiver to the gain G_r using Eq. 2.10, the relation for $R \gg \lambda$ is obtained that

$$\frac{P_R}{P_T} = \left(\frac{\lambda}{4\pi R}\right)^2 G_r(\theta,\phi) G_t(\theta,\phi). \tag{2.12}$$

This is well known as the Friis transmission equation [16]. It characterizes the power transfer from transmitter P_T to receiver P_R. It is often denoted in logarithmic values

$$P_R = P_T + L_{FS} + G_T(\theta,\phi) + G_R(\theta,\phi) \quad [\mathrm{dBm}], \tag{2.13}$$

with the realized gain of the transmitter and receiver G_T and G_R in dB. Furthermore, the term L_{FS} is often used to denote the free-space path loss (FSPL), which is given in logarithmic scale as

$$L_{FS} = 10\log_{10}\left[\left(\frac{\lambda}{4\pi R}\right)^2\right]. \tag{2.14}$$

This indicates that, at a minimum, the signal power gets weaker in an inverse squared fashion over distance, as is confirmed in Eq. 2.1. Note that this equation is very generic and does not include any attenuation of the signal such as cable losses and atmospheric absorption.

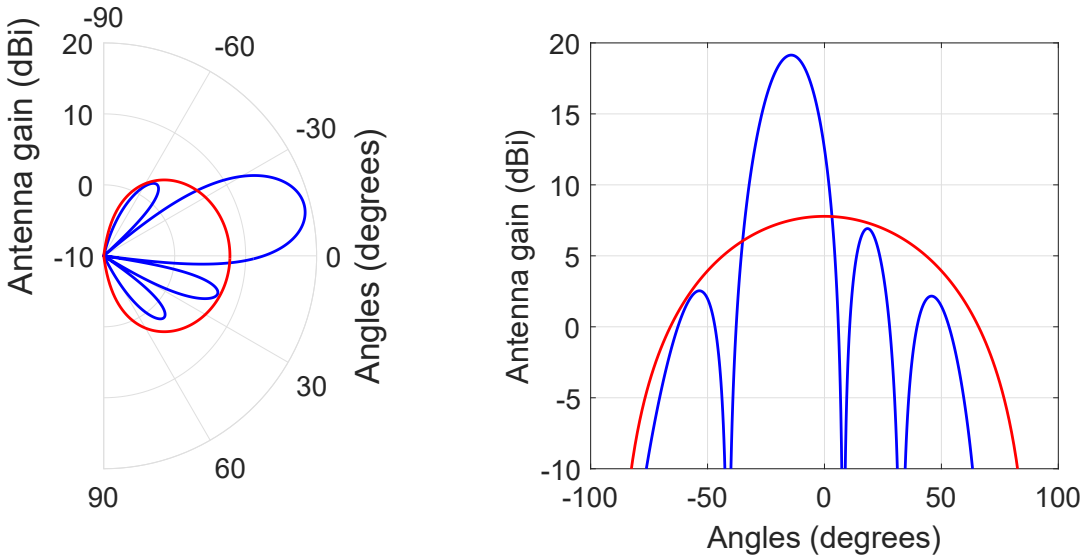

Figure 2.2: Cross-section of a high (blue) and low (red) gain antenna pattern, shown in the polar and unfolded cartesian representations.

Another property that describes the size of the antennas 'spotlight' is the directivity. The directivity is defined as the Half Power Beam Width (HPBW), which considers the angle where the signal strength is at most -3 dB below the maximum value [17]. This relationship between the gain and the angular beamwidth, i.e. directivity, θ in degrees to the gain is given by

$$G = \sqrt{\frac{2}{1 - \cos\left(\theta \frac{\pi}{360}\right)}}, \tag{2.15}$$

as stated in [15]. Logically, an isotropic antenna ($\theta = 360°$) corresponds to a gain of 1, or 0 dBi.

The radiation pattern $G(\theta, \phi)$ is a key parameter of any antenna, as it relates the directions in which the transmitted power is radiated and thus describing how energy is distributed over various angles. This is beneficial for applications where the position of the receiver is unknown. The downside, however, being that a significant portion of the transmitted power does not end up at the receiver. Thus a trade-off is visible between directionality of wireless nodes and efficient use of power.

Some applications make use of a focused beam which amplifies the signal in one direction at the cost of a weaker one in others. To distinguish these from other antennas, the phrases low and high gain are used, as shown in Fig. 2.2. The antenna gain describes how effective the antenna transmits power to its intended target relative to the isotropic reference, assuming they are aligned.

Although the polar representation is the most natural way of expressing the pattern, extra attention is needed whenever this plot is shown the logarithmic domain; since this range has no lower limit, the lowest value is free to choose resulting in possible loss of information. For example, if the amplitude of Fig. 2.2 is plotted for the gain range of 0 dBm to 20 dBm, many details of the high gain antenna would be hidden and appear to be nonexistent. Throughout the rest of the document, radiation patterns are shown in a cartesian plot.

For directive antennas, the angle in which most of the power is directed, is called the main beam [18]. The angular span of this main beam is expressed as the HPBW. Any peak that is not the main beam is called a side lobe and is almost always an unwanted side effect of high gain antennas. A parameter to indicate the strength of these side lobes is called the Side Lobe Level (SLL), which is the strength of the highest side lobe relative to the main beam. For example, when designing an antenna system, a goal could be to achieve SLL $< -20\,\text{dB}$. Valleys between the lobes at which the power asymptotically goes to zero are called nulls.

The antenna gain, which is sometimes called absolute gain, does not consider any mismatch. In reality, it is not possible to transfer all the power to the antenna due to reflections and material losses in the antenna. This is expressed by the ratio of incident V^+ and reflected V^- complex voltages, called the reflection coefficient Γ and is given by

$$\Gamma = \frac{V^-}{V^+} = \frac{Z_L - Z_S}{Z_L + Z_S}, \tag{2.16}$$

with load and source impedances Z_L and Z_S, or in this case, antenna impedance Z_L and signal generator impedance Z_S. In order to minimize reflections, Γ should be made as close to zero as possible, which is achieved by designing the antenna impedance for the conjugate match condition $Z_L = Z_S^*$. In the often used $50\,\Omega$ systems, this simply means that a resistive load of $50\,\Omega$ is required. To include these losses into a total gain of the antenna, the term realized gain is used. It describes the gain including impedance mismatching, given as

$$G_{re}(\theta, \phi) = \left(1 - |\Gamma|^2\right) G_A(\theta, \phi). \tag{2.17}$$

It is a more practical representation from a system perspective, since it shows how much gain is available from input to output. Since mismatching always reduces performance, the realized gain is inherently lower than the absolute gain. Note that this gain is expressed in dB and no longer in dBi.

2.1.1. Polarization

The findings of Eq. 2.1 show how the power intensity distributes, reasoning from the underlying physical properties. One way to express this in the electromagnetic (EM) domain is by the Poynting vector. This field vector $\mathbf{S}$ shows the directional energy transfer by

$$\mathbf{S} = \mathbf{E} \times \mathbf{H} \quad \left[\frac{\text{W}}{\text{m}^2}\right], \tag{2.18}$$

where $\mathbf{E}$ and $\mathbf{H}$ are the complex, time dependent electric field in V/m and magnetic field in A/m [19]. To describe the fields in a time independent sense, the time-average Poynting vector is used

$$\mathbf{S}_{av} = \frac{1}{2}\text{Re}\left(\widetilde{\mathbf{E}} \times \widetilde{\mathbf{H}}^*\right) \quad \left[\frac{\text{W}}{\text{m}^2}\right], \tag{2.19}$$

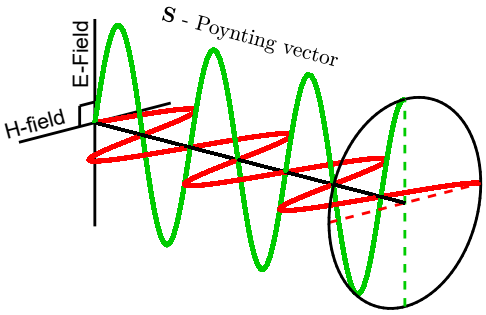

Figure 2.3: Linearly polarized fields, showing the fields related to the Poynting vector.

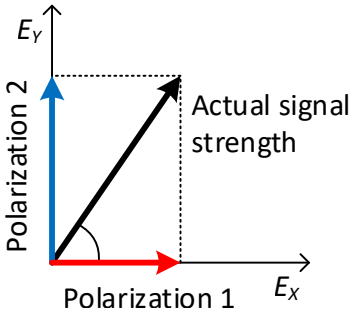

Figure 2.4: Decomposition of a the E-field signal into two distinct polarization directions.

where $\widetilde{\mathbf{E}}$ and $\widetilde{\mathbf{H}}$ are the phasor components, such that $\mathbf{E} = \widetilde{\mathbf{E}}e^{j\omega t}$ and $\mathbf{H} = \widetilde{\mathbf{H}}e^{j\omega t}$. The factor $\frac{1}{2}$ is introduced since the peak values $\widetilde{\mathbf{E}}$ and $\widetilde{\mathbf{H}}$ are converted to their RMS values. Note that $\mathbf{S}_{av}$ is the field equivalent of power intensity W in Eq. 2.1 and Eq. 2.3. Furthermore, whenever the orientation of a wave is described without distinguishing between E and H, it is assumed that the E-Field is described.

The Poynting vector shows that the electric and magnetic field are aligned and are both orthogonal to the direction of propagation $\mathbf{S}$, as visualized in Fig. 2.3. In free-space, these fields are not necessarily polarized, meaning that the waves have arbitrary field orientations. In the case of linear polarization of a wave, the electric and magnetic field are in phase with each other and strictly follow the same orientation. When the $\mathbf{E}$ and $\mathbf{H}$ fields are 90° out of phase from each other, a circularly polarized wave is generated.

In practice, an antenna typically transmits in one specific polarization. The field observed in this polarization axis is called the co-polar signal, whereas the orthogonal, 90° offset fields are the cross-polar ones. Generally, antenna systems benefit from having full isolation between these two axis such that they are treated as independent signals. To denote how strong the cross-polar signal feeds through, the term cross polar discrimination (XPD) is used. This states for a given angle what the ratio between the co- and cross-polar signals is.

For any communication link it is essential that the orientation of a transmitted wave aligns with the receiving antenna [18]. Therefore, base stations generally have both horizontal and vertical polarized antennas, such that the receiver always observes a signal.

For measurement setups, similar precautions must be taken. The transmitted signal of the AUT needs to be aligned in polarization with the AUT. This way, the signal is always fully received. Alternatively, the use of two perpendicular probes, i.e. one in x and one in y, allows any incoming wave to be detectable. If the signal is in between the two polarizations, e.g. 45°, both probes receive the projection of this signal on their axis, as shown in Fig. 2.4. By calculating the linear combination of the measured vectors, the actual amplitude is obtained.

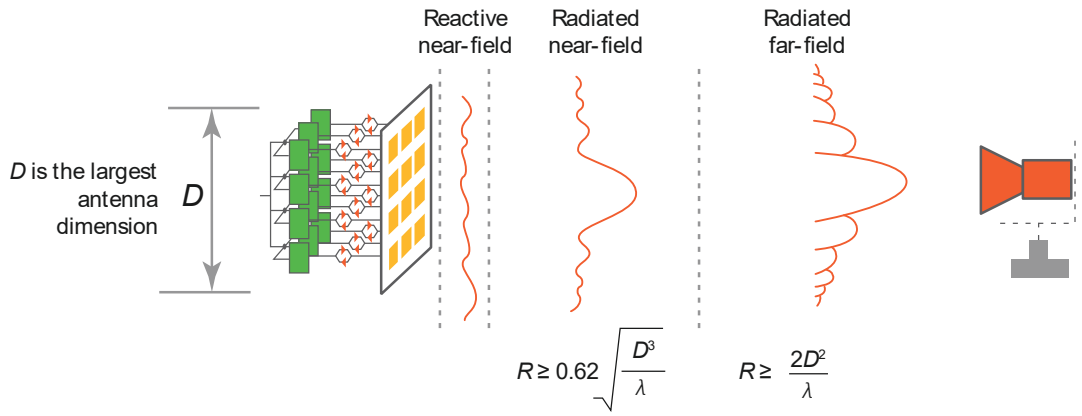

Figure 2.5: Graphical representation of the various radiation zones of an antenna. Adaptation to image courtesy of Keysight [20].

2.2. Radiation Field Regions

As the waves radiated by an antenna propagate radially, they become more and more planar. This is distinguished into multiple regions, depending on their wave properties: the near field and far field, with the near field consisting of a reactive and radiative part. These terms are visualized in Fig. 2.5.

The near field (NF) is the region in which the field distribution is not planar. When an observer is relatively close to the antenna, the transmitted wave approaches from different angles and with varying phases. Therefore, the near field radiation pattern is not consistent over distance. The near field is divided into two regions. The reactive region is the area closest to the antenna, in which the radiated fields are varying strongly. It is often defined as distance R being

$$R < 0.62\sqrt{\frac{D^3}{\lambda}} \quad [\mathrm{m}]\,, \tag{2.20}$$

with D being the antenna dimension, i.e. largest aperture diagonal (not width or length), and λ the wavelength, all in meters [18]. This region is used for power transfer such as wireless phone chargers and transformers. For characterization, this region is not suitable, as the insertion of any object, such as a probe, influences the behavior of the device and thus give an invalid measurement.

When leaving the reactive region, the observer is in the radiative region, also known as the Fresnel region. In this area, all the waves radiate spherically. Nevertheless, when a probe is placed in the near field, waves are able to reach the observer from various angles, thus not creating real plane waves. The solution for this is to move far away from the transmitter such that the transmitter appears as a single point source. The transition between the near and far field is not a hard one; it is considered a gray zone. Since vague boundaries are very inconvenient for design, the Fraunholer distance is generally accepted as the separating parameter between these regions [18, 19, 21]. It is calculated by allowing the actual spherical wave to have a deviation of at most $\frac{\pi}{8} = 22.5°$ from a true plane wave [18, 21].

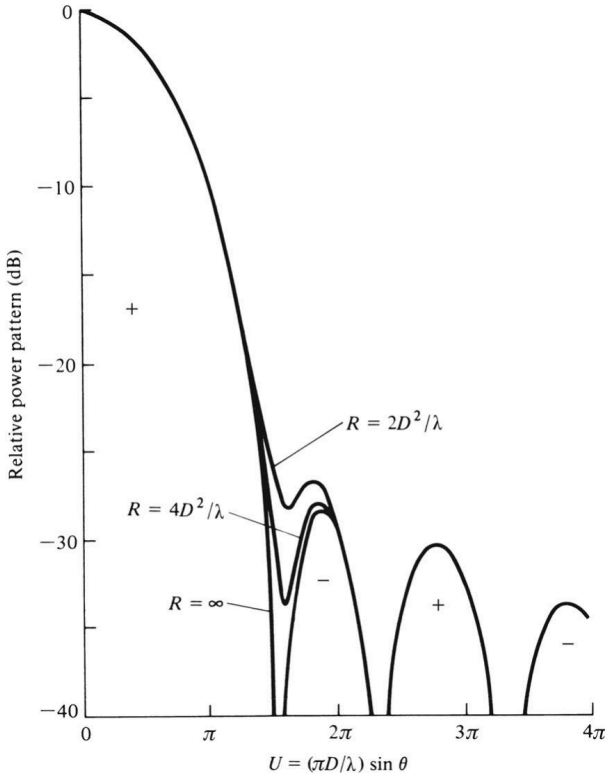

Figure 2.6: Observed radiation pattern at the Fraunholer distance, the double of this and infinity. Source: [18, 22].

This results in the boundary for antennas with $D \gg \lambda$ to be

$$R \geq \frac{2D^2}{\lambda} \quad [\text{m}]\,. \tag{2.21}$$

using the same value for D as in Eq. 2.20. This means that the radiative near field is bound between Eq. 2.20 and Eq. 2.21. At this distance, the radiation pattern is almost identical to that at $R = \infty$. However, in Fig. 2.6 we can see that between the main lobe and first sidelobe there is still some deviation.

The radiation pattern of an antenna always represents the radiated power in the far field, because it is independent of the distance. Therefore, the most trivial way of measuring a pattern is in this domain. Most communication links are set up in far field as the distance is not within near field.

An antenna measurement takes either place in the near field (NF) or the far field (FF). Since the radiation patterns are defined in the far field, the most direct solution would be to measure in this domain. This is, however, not always practical as the distance of the far field could make the measurement inefficient. Furthermore, at high frequencies the path loss are substantial. For example, by using Eq. 2.21 we find that for a 60 GHz antenna array of 10 cm × 10 cm, the far field is at 4 meter with a corresponding path loss of 80 dB, which is very large for most setups. For this reason, near-to-far field transformations are performed in various measurement setups [23–25]. This transformation makes use of the Fourier transform to get the far field representation from near field samples.

The disadvantage of acquiring far field patterns by means of this transformation is that there are

more requirements on the measurements. That is, the use of the Fourier transform requires the samples to have both amplitude and phase information. The acquisition of the phase is troublesome if the AUT is not controllable, for example when the AUT uses an integrated circuit to generate the signals. There do exist several techniques to omit the need for absolute phase in near field antenna testing [26, 27], but these still require a phase measurement. Furthermore, to satisfy the sampling theorem there is a maximum allowed spacing between samples, being

$$\Delta x = \Delta y = \frac{\lambda}{2}\,[\mathrm{m}]\,, \tag{2.22}$$

or, in a spherical setup,

$$\Delta\phi = \Delta\theta = \frac{\lambda}{2\,(a+\lambda)}\,[\mathrm{rad}]\,, \tag{2.23}$$

with $\Delta\phi$ and $\Delta\theta$ the angular spacing between nodes in rad, λ the wavelength and a the largest dimension of the AUT [18]. When considering the frequency range 28 GHz to 60 GHz and typical antenna sizes of 1 cm × 1 cm to 10 cm × 10 cm, Eq. 2.22 yields a required planar step size of approximately 5 mm to 10 mm, or in the case of Eq. 2.22 between 0.5 deg and 3 deg. This is feasible with a scanning (single) detector setup, but would require a exceedingly high amount of detectors in a static array measurement. Therefore, the option to measure in the near field is ruled out and the measurements for this project are performed in the far field.

2.3. Measurement Distance

In order to measure the radiation pattern, an over-the-air (OTA) characterization is required. This involves the use of a probe antenna that measures power at a known angle. To keep the measurement setup reasonable in size, a short distance between AUT and the probes is preferred. On the other hand, the probe needs to be in far field, following Eq. 2.21, in order to measure an accurate pattern. This results in a trade-off between setup size and antenna aperture size.

To understand the distances that are allowed at the various frequencies and array sizes, the equation $R \geq \frac{2D^2}{R}$ is rearranged such that it gives a more intuitive understanding of its constraints. The most general approach is to express both R and D in terms of wavelength. If we choose $R = \lambda r$ and $D = \lambda d$ such that

$$r\lambda \geq \frac{2N^2\lambda^2}{\lambda}, \tag{2.24}$$

the wavelength dependency cancels out, yielding

$$r \geq 2d^2. \tag{2.25}$$

This simple equation gives a universal overview for the far field distance independent of frequency. This curve is visualized in Fig. 2.7a. This means that an antenna with, for example, a size of 3λ corresponds to a far field distance of 18λ.

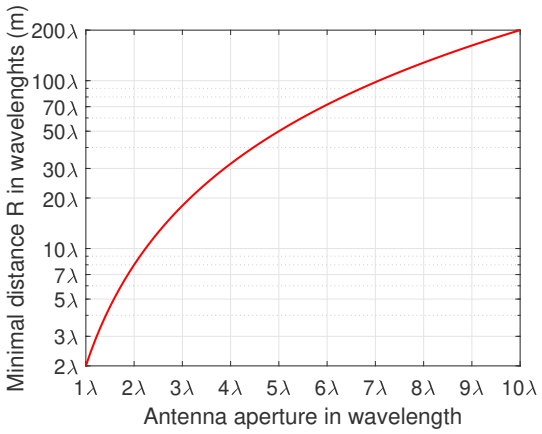

(a) Far field distance expressed in terms of wavelength, for an antenna aperture of a given wavelength. This results in the same curve for all frequencies.

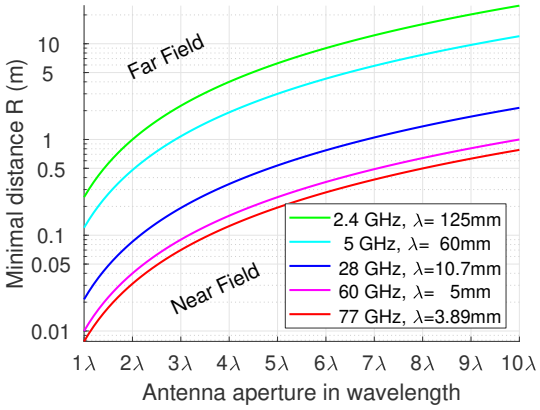

(b) The required far field for various frequencies versus antenna size in relative to the frequency wavelength. Note that only the y axis is in logarithmic scale.

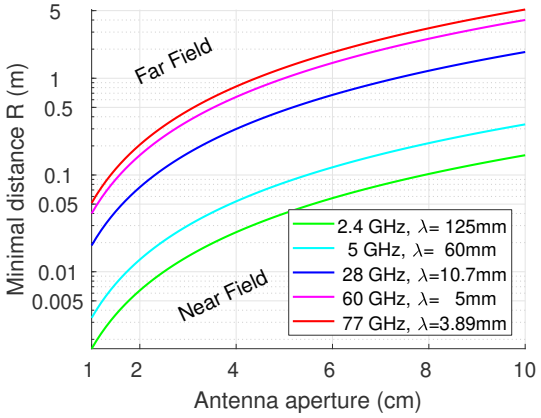

(c) The required far field for various frequencies versus physical antenna aperture size. Note that both axis are in logarithmic scale.

Figure 2.7: Minimal distance to be in far field following Eq. 2.21. Note that all the vertical axis are shown in logarithmic scale.

To relate these properties to a more tangible dimension, the far field is expressed as physical distance in meters for a given aperture size in wavelengths. This follows the equation

$$r \geq 2d^2\lambda \tag{2.26}$$

and is visualized in for multiple frequencies in Fig. 2.7b. If we examine the physical antenna, higher frequencies require a larger distance to be in the far field. Finally, the far field equation is shown for both a physical far field distance and an aperture size in meters, following Eq. 2.21 in Fig. 2.7c. These figures suggest that a good consideration on the largest antenna size is required since it quickly increases the required far field distance.

As a reference for antenna sizes for the measurement, the recent 3GPP standard TR38.810 is considered [28]. It contains definitions for OTA measurement setups, in particular aimed at mm-wave frequencies for 5G. There are three catagories for defined for AUT sizes, here called device under test (DUT). The categories are shown in Fig. 2.8.

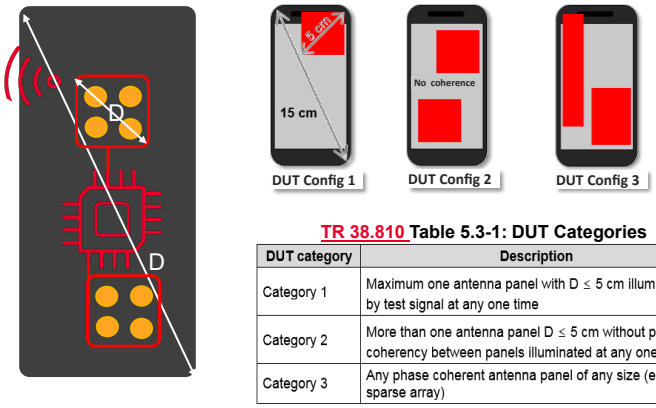

TR 38.810 Table 5.3-1: DUT Categories

DUT category	Description
Category 1	Maximum one antenna panel with D ≤ 5 cm illuminated by test signal at any one time
Category 2	More than one antenna panel D ≤ 5 cm without phase coherency between panels illuminated at any one time
Category 3	Any phase coherent antenna panel of any size (e.g. sparse array)

Figure 2.8: AUT catagories as defined by 3GPP standard TR38.810 [28]. Figure source: [20].

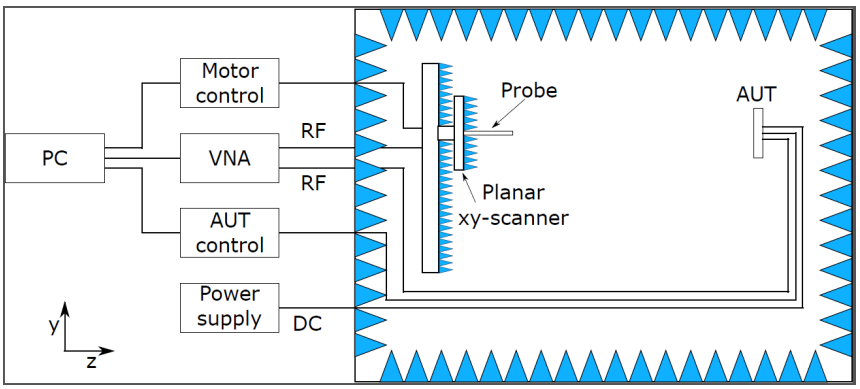

Figure 2.9: Schematic example of a typical scanning measurement setup. The scanning plane is either planar, cylindrical or spherical.

2.4. Available Measurement Setups

In most cases, the characterization of antenna radiation patterns is performed by means of a single scanning detector antenna which measures one angle at the time. By scanning various cross-sections, the full 3D radiation pattern is obtained. A schematic overview of a typical measurement setup is shown in Fig. 2.9. This method is widely used for mapping parameters such as radiation pattern and polarization. There are many publications regarding this type of measurement and it is applied widely in industry, a selection of these is shown in Table 2.1. This overview shows that both near field and far field measurement setups are employed in practice. A few publications are discussed in more detail.

The far field mm-wave antenna measurement setup developed by TU Eindhoven is shown in Fig. 2.10 [34]. It consists of a spherical anechoic chamber in which a ganty rotates around the AUT. A rotatable horn antenna operates as probe. Both antennas are connected to a VNA and the whole system is controlled with a LabVIEW program on a PC. When a single frequency is measured, the arm is moving continuously and each cross-section takes approximately two minutes, resulting in a complete measurement time of roughly one to two hours. In the case of a frequency sweep, the arm stops at every point which significantly increases time. The setup is capable of measuring on-wafer antennas with a wafer probe and stabilized table.

Table 2.1: Overview of publications on scanning measurement setups. Note that the measurement time are often estimations that strongly vary with the number of sampling points.

Publication	Near or far field	RX-TX dist. [cm]	Freq. [GHz]	Measurement time	Remarks
[26]	NF	<5	60-94	4 h	Using relative phase meas.
[27]	NF	≈20	9	Unknown	Phaseless NF meas.
[29, 30]	NF	70	33	8 h	For large antennas
[31]	NF	4	78	43 min	On-wafer meas.
[32]	FF	20	60	2 h	
[33]	FF	100	2-40	Unknown	On-wafer meas.
[34]	FF	30	24-110	2 h	On-wafer measurement

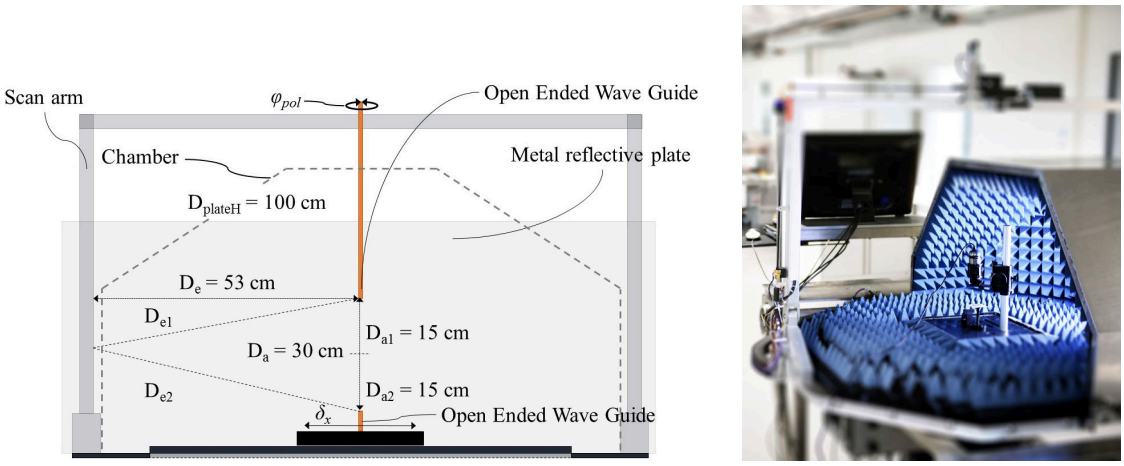

Figure 2.10: Scanning arm measurement setup by [34]. Half of the absorber cover is removed to show the inside.

An example of a near field scanning setup developed at the TU Delft is the one shown in Fig. 2.11 [26]. The arm on top is moved around in three dimensions, in a space of $500 \times 500 \times 350$ mm. It is controlled with a CNC machine using MATLAB and the data is acquired from a VNA. The setup is mainly used for on-wafer antenna measurements with the help of a wafer chuck, wafer probe and microscope for alignment. The typical probe used is an open ended waveguide (e.g. WR15 size). With the addition of a second probe, a relative phase measurement is performed instead of acquiring the actual AUT phase, which is convenient for systems with an embedded antenna that is not accessible for the VNA.

2.5. Phased Array Antennas

Phased array concepts are used to build the Massive MIMO (Multiple-Input Multiple-Output) communication systems for 5G. The conventional, passive phased array system, shown in Fig. 2.12a consist of a single RF exciter, which is phase shifted using an analog beamformer. The digital phased array shown in Fig. 2.12b shows more potential for Massive MIMO, since it allows configuration of many properties. In contrast to the passive topology, every element generates an independent signal. By using appropriate digital signal processing (DSP), element weighting is applied to position the pattern nulls freely [9]. Furthermore, these systems are able to generate any number of beams by superimposing multiple

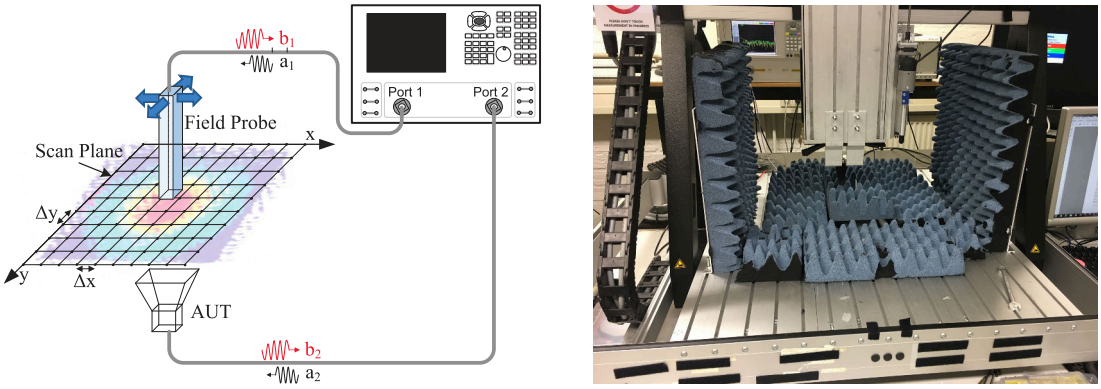

Figure 2.11: Scanning near field measurement setup by [26]. One antenna is mounted in the top frame and one centered on the bottom plate. This setup is build with absorbers, but there are many other configurations possible, e.g. including a frequency extender.

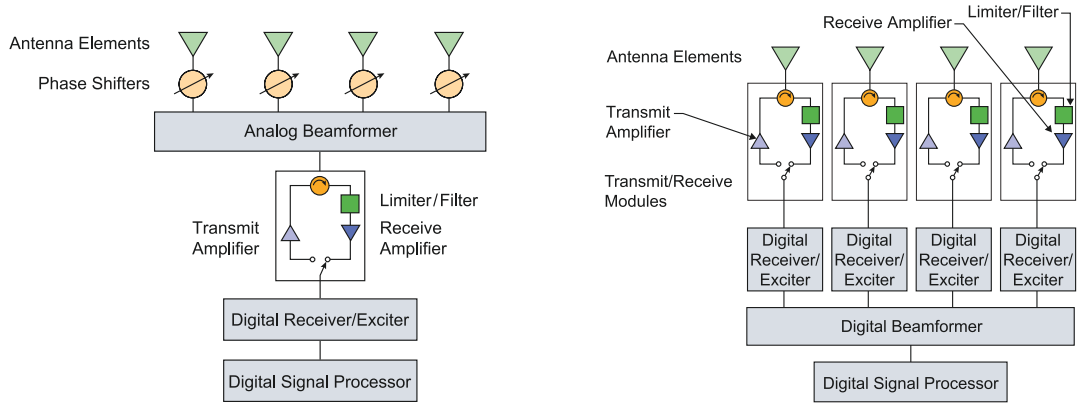

(a) Passive phased array architecture.

(b) Element-level digital phased array architecture.

Figure 2.12: Phased array system architectures, source: [9].

signals. With this, many users are served with one base station.

To get an indication of the sizes and properties of possible AUT's for the proposed measurement setup, a selection of state-of-the-art research is shown in this section. A comparison of novel phased array systems for 5G mm-wave communication is presented in Table 2.2 for 28 GHz and Table 2.3 for 60 GHz respectively. Note that these arrays are typically composed of multiple unit block (i.e. 4x4) antennas. Therefore, a subsystem could be tested if the dimensions would be too big to measure in a given setup. Furthermore, these publications are very recent and actual industrial products could differ from the described ones. For the construction of an antenna measurement setup the following properties of the devices are of importance:

- **Frequency:** Since everything in the electromagnetic domain scales with wavelength, frequency is a key parameter in any RF design. Also, the instruments need to be able to handle the frequency band.
- **Antenna aperture:** The physical size of the antenna relates to the far field distance.
- **Beam width (HPBW):** If the main beam is smaller it might be more difficult to measure.
- **Side lobe level:** If the side lobes are weaker, they are harder to acquire.

Table 2.2: Comparison of recent 28 GHz mm-wave phased-array antenna systems, with calculated far field distance based on Eq. 2.21.

	Kibaroglu '18 [35]	Sadhu '17 [36]	LG '17 [37]
Technology	0.18 µm SiGe BiCMOS	0.13 µm SiGe BiCMOS	28 nm CMOS
Total ant. elements	32	32	8
Ant. Array dimensions	40 mm × 25 mm	11 mm × 16 mm	11 mm × 22 mm
Bandwidth (MHz)	400	800	10
Modulation	256QAM	256QAM	64QAM
OTA Data rate	6 Gbps (16QAM @ 5 m)	2.5 Gbps QPSK	LTE 10 MHz @ 2.5 m
Beam steering	1° steps	1.4° steps	-
HPBW (deg)	12.8	11	63
Far Field distance	41.5 cm	7.0 cm	11.3 cm

Table 2.3: Two recent 60 GHz mm-wave phased-array antenna systems, with calculated far field distance based on Eq. 2.21.

	Zihir '18 [38]	Sowlati '18 [39]
Technology	0.13 µm SiGe BiCMOS	28 nm CMOS
Total ant. elements	32	144
Ant. Array dimensions	21 mm × 22 mm	42 mm × 45 mm
Bandwidth (MHz)	1760	1760
Constellation	16QAM	16QAM
OTA Data rate	1.5 Gbps (QPSK @ 100 m)	4.6 Gbps
Beam steering	<5° steps	3° steps
HPBW	6°	6°
Far Field distance	37 cm	150 cm

3

Multi-probe Measurement Array

This chapter describes various theoretical properties and design of a measurement setup that characterizes antennas in seconds without moving parts. It first covers optimal sensor distribution after which measurement topologies and existing research is discussed. Finally, an analysis is done on the required number of probes.

3.1. Sensor Arrangement

An antenna pattern is fully described if all of its maxima, the main lobe, side lobes and intermediate nulls are captured. To achieve this, either the sensor(s) are moved mechanically around the AUT, or an adequate amount of static sensors is employed in a proper distribution. This latter option is researched in this thesis, since mechanical scanning options are slow and costly [20], due to the need for accurately moving parts. In contrast, a properly distributed multi-sensor array is able to instantly capture each setting of an AUT. Of course, as with its mechanical equivalent, taking more samples is necessary when multiple patterns of an AUT need to be characterized.

When choosing a distribution, options are to choose for a planar (i.e. flat) or spherical array, as shown in Fig. 3.1 and Fig. 3.2. A third option is the use of a cylindrical topology, but since it experiences the disadvantages of both planar and spherical, it is not discussed. The planar array is more straightforward in terms of construction complexity, but shows multiple disadvantages compared to the spherical setup. These are grouped in positioning, path loss and non-uniformity.

One issue with a planar array is that the main beam of the detectors is not orthogonally aligned with the AUT when they are mounted identically. This could be compensated by using omnidirectional probe antennas, with the downside that less power is received from the AUT. Another possibility would

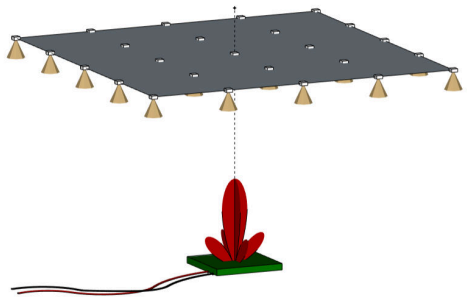

Figure 3.1: Example of a planar measurement array.

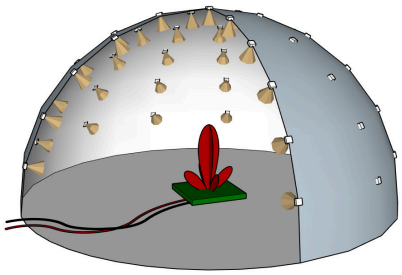

Figure 3.2: Example of a spherical measurement array.

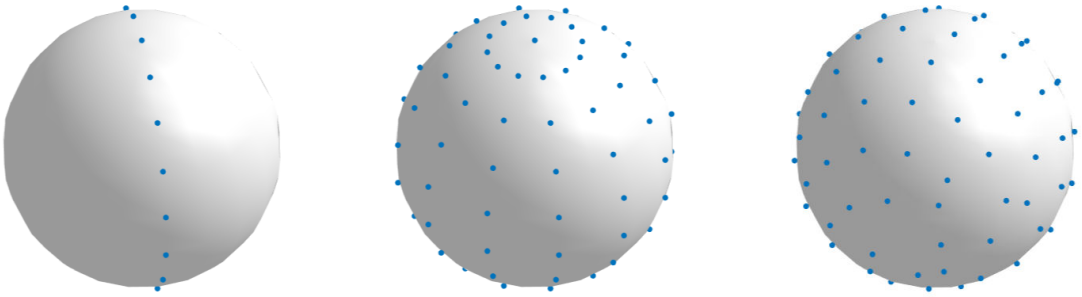

(a) Linearly distributing over a single cross section.

(b) Distributing points at fixed azimuth lines.

(c) Pseudo-random method of placing points over a sphere.

Figure 3.3: Methods of distributing points over a sphere.

be to position the detectors such that they all face straight towards the AUT, which would rely heavily on fabrication precision and does not resolve blind spots at wider angles. Also, the varying distance from the sensor to the AUT have to be accounted for by calibration and compensation in post-processing and also results in the need for detectors with higher dynamic range.

In the spherical configuration all the detectors are orthogonally aligned to the AUT, are equidistant and are able to cover all required angles. Therefore, spherical has many advantages as it simplifies the system at the cost of a slightly more complex construction.

In the case that the antenna beam is unknown or has multiple settings, a higher density of probes could be positioned. Therefore, the most logical distribution would be a linearly spaced one. An example of a single arc with a spherical topology is shown in Fig. 3.3a. When this line distribution is replicated for multiple cross-sections to achieve a full sphere coverage, the topology shown in Fig. 3.3b is obtained. This is not an optimal method of setting up sample points, as the cross-sections get closer to each other at higher angles, but is more convenient for constructing since it consists of multiple arcs.

If there is a need to distribute detectors more equally, other methods have to be considered. One way to do this is a Fibonacci lattice to spread out a number of points evenly over a sphere, as shown in Fig. 3.3c. This is achieved by rotating every sample by 2.4 rad (approximately 137°) and fitting this angle on the sphere, essentially following a (very tight) helix shape from top to bottom. This method results in a distribution which is more uniform than the linearly spaced one. The disadvantage of this is that there is not a suitable grid to assemble the detectors on, which makes the assembly more complicated.

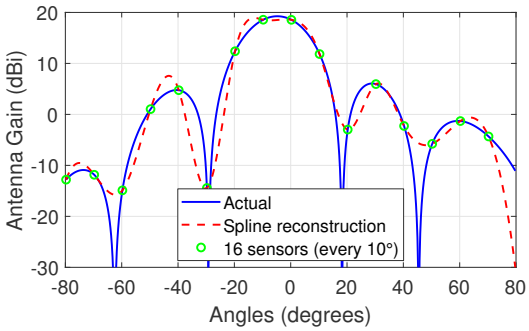

Figure 3.4: A radiation pattern (blue) is sampled on the marked points (green) and is reconstructed (red) in the shown logarithmic domain.

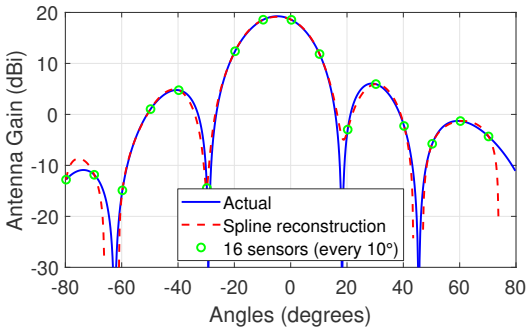

Figure 3.5: A radiation pattern (blue) is sampled on the marked points (green) and reconstructed on the linear scale and converted back to the shown logarithmic pattern (red).

3.2. Number of Detectors

An important factor for the feasibility of the setup is the number of detectors that are required to measure a given device. As the intention of the project is to get a flexible setup, there is not an universal answer to this question. To still get an indication of this, it is necessary to understand how accurate the radiation pattern reconstruction needs to be. This is dependent on the parameters that need to be measured.

First of all, the measured points need to be connected to create a continuous pattern. This is implemented with the polynomial interpolation method `interp1()` of MATLAB. In particular, the spline type interpolation results in the most accurate reconstructions. Furthermore, the interpolation is performed on the linear scale, instead of the displayed logarithmic scale. The difference is shown in Fig. 3.4 and Fig. 3.5. It is immediately clear that the typical parabolic-like shape of an antenna pattern is preserved when sampling on the linear dataset.

The most straightforward method of grading the reconstruction of a pattern would be by looking at the absolute or relative error of the reconstruction compared to the actual pattern, in either the linear or logarithmic scale. This, however, does not give an useful figure of merit to judge the reconstruction quality as the number by itself is not related to any design parameter of the antenna. For this reason, a list is made of parameters on which the reconstruction is graded:

- Main Beam
  - Power mismatch in decibel
  - Angle mismatch in degrees
  - Half Power Beam Width (HPBW) mismatch in degrees
- First Side Lobe
  - Power mismatch in decibel
  - Angle mismatch in degrees
- Null locations
  - First Null Beam Width (FNBW) mismatch in degrees

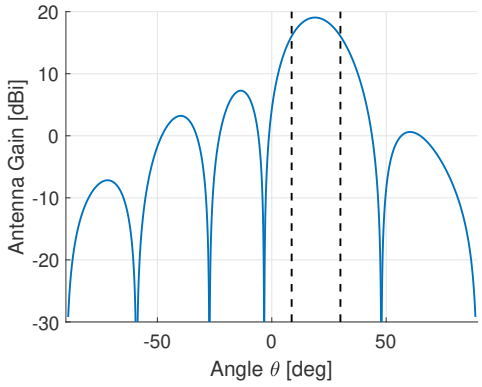

Figure 3.6: Used pattern for the given example, the −3 dB HPBW boundary is shown (dashed).

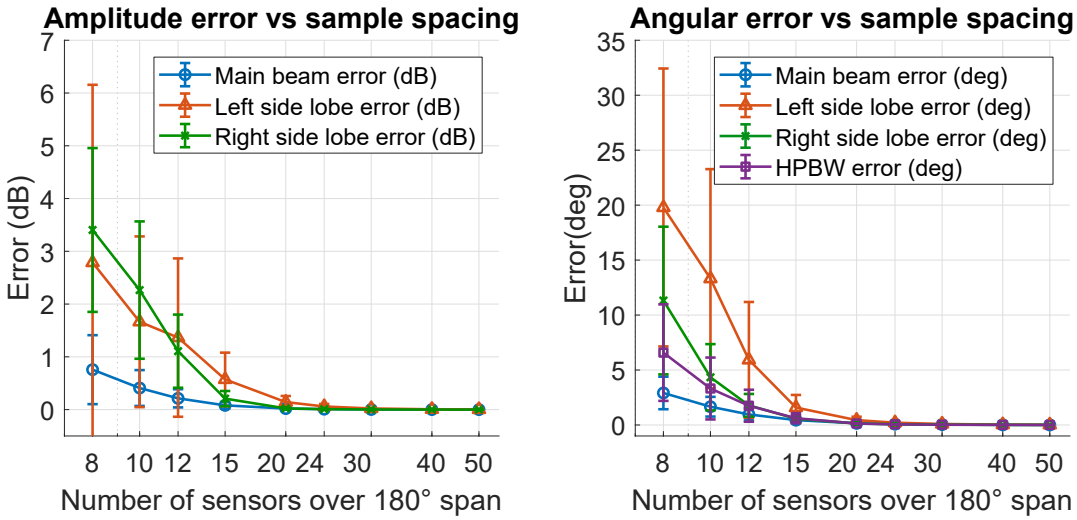

Figure 3.7: Sampling error versus amplitude (left) and angle (right) error terms. The horizontal axis shows the number of sensors over $180\,\mathrm{deg}$. The error bars show the variation for offsets of the sensor array.

With the methods of reconstructing and grading defined, a quantitative analysis is performed using simulations in MATLAB. For this, a script is made where an arbitrary radiation pattern is given as input. This pattern is then sampled and reconstructed over a 180° cross-section with a varying number of sample points. It is important to consider the sample points on various offsets, because the detector array could incidentally align on a less convenient position to reconstruct the pattern. The various pattern reconstructions (varying sample points and multiple offsets) are graded on the stated properties.

As an example, a 5×5 phased array, which is beamsteering to an arbitrary angle, is entered into the script. The corresponding radation pattern, as shown in Fig. 3.6, is graded and the results are shown in Fig. 3.7. What stands out is that there is a clear convergence point at which an accurate reconstruction is made. For the stated example, 15 to 20 points over a single cross-section would suffice.

3.3. Measurement Topology

Single-probe measurement setups measure the RF signal by feeding it into a VNA or spectrum analyzer. For a multi-probe setup, one instrument per measurement point is, obviously, too expensive. The

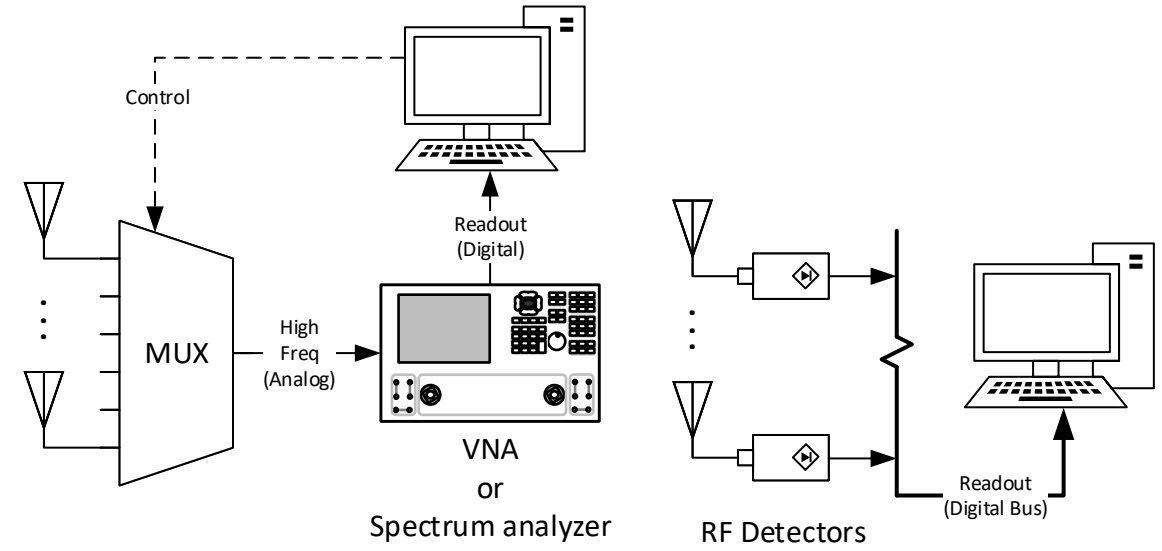

(a) Concept readout method using a MUX.

(b) Concept readout method using direct down-conversion at every element.

Figure 3.8: Two topologies for a multi-probe setup.

Table 3.1: Overview of static detector array measurement methods. Note that operating frequency is typically a bandwidth, the value is merely to give a rough indication.

Publication	Near or far field	RX-TX dist. [cm]	Freq. [GHz]	Measurement time	Remarks
[40]	NF	100	1.8	Real-time	Full sphere
[41]	NF	90	0 - 18	Real-time (Cross-section)	Single line Commercial product
[42, 43]	NF	200	2.5	5 s	Single line

most logical workaround would be to use an RF multiplexer (MUX) to connect every probe to the instrument sequentially, as shown in Fig. 3.8a. Although this is possible, the MUX and cables for mm-wave frequencies become very expensive when using many measurement points.

A very different approach would be to have a sensor positioned close to each receiving antenna, such that the high frequency circuitry is terminated as soon as possible. This concept is shown in Fig. 3.8b. A communication bus, e.g. I2C, SPI, USB, Ethernet, GPIB, etc., is used to read out each sensing element. Since there is only one value to be measured per element, there is no need for high speed readout. The biggest challenge in realizing this is to make each detector affordable while still achieving the required accuracy.

In the following chapter, several publications are shown which make use of the former method, using a MUX. The current project makes use of the latter option, using direct down-conversion.

3.4. Existing Publications

There are several publications on multi probe OTA measurement; an overview is given in Table 3.1. Although they show similarities, each one has a substantial difference with the proposed concept. Therefore, they are discussed here.

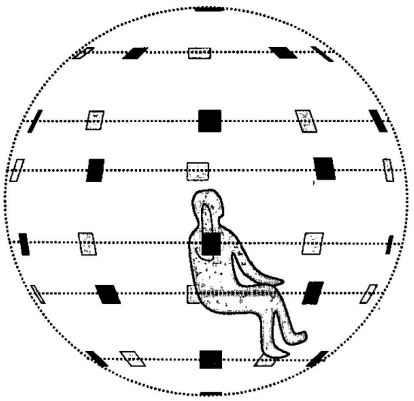

Figure 3.9: Spherical measurement setup as proposed by [40].

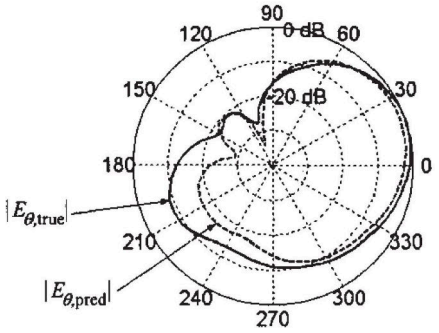

Figure 3.10: Example of reconstructed pattern (solid) compared to true pattern (dashed) [40].

The first publications found on static measurement arrays with more than three points is made around 2004 by the Helsinki University of Technology in collaboration with Nokia [40]. This setup consists of 32 patch antennas distributed over a sphere, as shown in Fig. 3.9. Each element is measured on a VNA using an RF MUX. The system is used to measure mobile phone radiations at 1.8 GHz. The tested antennas do not have narrow beams, which allows relatively large spacing of approximately 30° between detectors. From the measured pattern in Fig. 3.10, it is visible that reconstruction is accurate for the largest part of the pattern.

Another set of publications was made by the company Satimo on the StarLab setup, around 2007 [41]. The AUT is set in a single ring of probes which measures the near field radiation of the probe. There are 15 probes to cover frequencies up to 6 GHz and 16 other probes to cover 6 GHz to 18 GHz. Since only one cross-section is measured at once, the antenna is rotated to cover at all angles. The setup is shown in Fig. 3.11. In terms of measurement topology, this method is very similar to the first one; it also uses a MUX readout system.

A similar system is developed at the Aalborg University for measurement of their antenna systems [42, 43]. Here, a ring of 16 dual polarized horn antennas is used to map the radiation pattern of antennas. Various methods of reconstructing planar far field patterns are discussed. The measurement setup is shown in Fig. 3.12.

All described methods make use of the near-to-far-field expansion method. This is possible due to the focus on frequencies below 3 GHz, allowing for large antenna spacing, following Eq. 2.23. The low frequency also results in a preference for measurement in near field, since the far field at frequencies below < 3 GHz is in the range of one to ten meters, as shown in section 2.3. At mm-wave frequencies, this far field becomes measurable within a more reasonable distance. Since a near field setup requires the measurement of complex values, i.e. including phase, all methods make use of an expensive instrument such as a spectrum analyser or VNA and a multiplexing system between probes. This makes the setup more complicated, especially when moving towards mm-wave frequencies.

It is visible that only a few studies are performed on detector arrays for antenna measurements.

Figure 3.11: Starlab commercial setup [41].

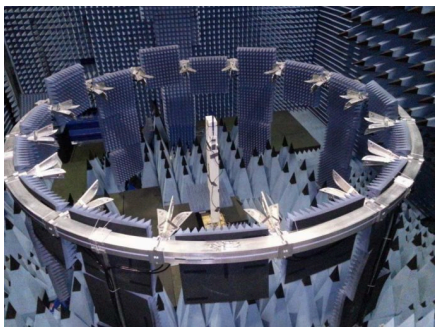

Figure 3.12: Setup of Aalborg University [42].

Even more so, only one publication on a true three dimensional setup is found. Nevertheless, the presented research shows great potential for future possibilities as measurement time is reduced drastically. These setups are still not adapted by most research facilities since it is not a well known method of measuring.

4

Development of Sensing Probes

In order to measure the radiation pattern accurately, an appropriate probe point needs to be developed. In this chapter, the various options for the complete sensor probe system are discussed, and possibilities for future expansion are given.

4.1. Link Budget

To set up an over-the-air (OTA) measurement setup or communication link, it is essential to receive the appropriate signal levels at the receiving end. To verify if the incoming signal is not too weak, a link budget is set up in which all the gain and loss components are summarized. If the signal strength is too low, detector sensitivity must be increased or additional amplifiers must be added. The link budget is set up for the proposed measurement setup and is be described below. The parameters used in this section are shown in Fig. 4.1.

Although the measurement array consists of multiple sampling points, they are assumed to be identical and therefore only one point needs to be considered for the link budget, as long as it is capable

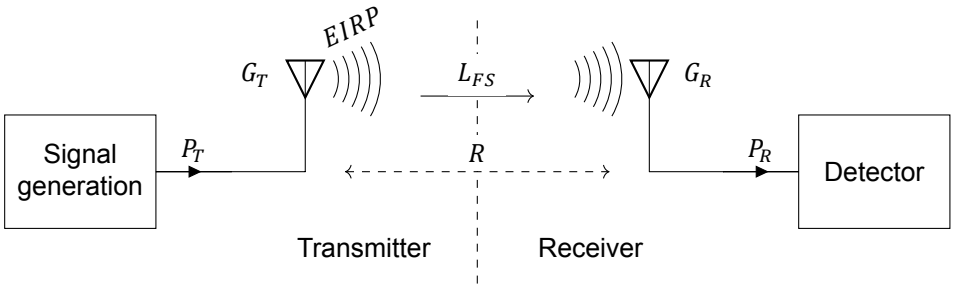

Figure 4.1: Schematic overview of the parameters related to a transmission link.

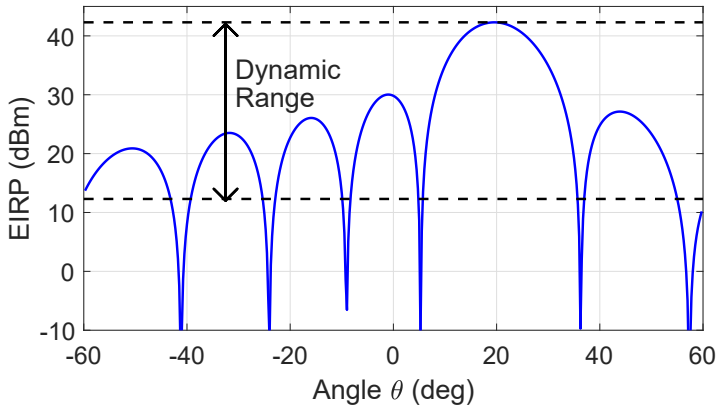

Figure 4.2: Example of a radiation pattern crossection with gain G_T shown versus angle. This 8x8 phased array pattern, beam-steering at 20°, is generated using the MATLAB Antenna toolbox. As an example, a dynamic range is shown.

of handling the power levels at the various angles, as shown in Fig. 4.2. Hence, both the peak and the lower parts of a radiation pattern need to be within the dynamic range (DR) of the receiver. These levels are depending on two parameters of the AUT: the Effective Isotropic Radiated Power (EIRP) and sidelobe levels.

The EIRP indicates the power radiated at the main beam, typically in dBm. It is be expressed as

$$EIRP[\text{dBm}] = P_T[\text{dBm}] + G_T[\text{dBi}] - L_T[\text{dB}], \tag{4.1}$$

where P_T denotes transmitted power, G_T the antenna gain and L_T losses of the transmitter. The EIRP describes how much power the receiver sees, as if it would transmitted by an isotropic antenna ($G_T = 0\,\text{dBi}$).

From the found literature in Table 2.2, a typical EIRP for recent 28 GHz phased arrays is in the range of 35 dBm to 50 dBm. For the example link budget calculation, a value of 40 dBm is used. Furthermore, to measure the complete radiation pattern, the sidelobes also need to be measured. Ideally, the complete amplitude range should be measurable, including the nulls. These asymptotes go down to zero which would require an infinite dynamic range. However, the nulls are detectable whenever the sidelobes are sufficiently visible. For this project, a measurable sidelobe level of 30 dB is set. This means that the transmitting antenna transmits in the range of 10 dBm to 40 dBm over all angles.

Having discussed how the signal is transmitted, this section examines how the signal propagates and is received by the observer. As the found transmitter power levels are expressed in EIRP, the Friis transmission equation, Eq. 2.13, is rewritten to

$$P_R = EIRP(\theta, \phi) + L_{FS} + G_R(\theta, \phi). \tag{4.2}$$

For the next example we choose a receiving antenna with $G_R = 12\,\text{dBi}$, $R = 0.5\,\text{m}$ and an effective EIRP of 10 dBm to 40 dBm. With these numbers, the detector receives a signal of approximately $-33\,\text{dBm}$ to $-3\,\text{dBm}$ at 28 GHz and $-40\,\text{dBm}$ to $-10\,\text{dBm}$ at 60 GHz. These are reasonable power

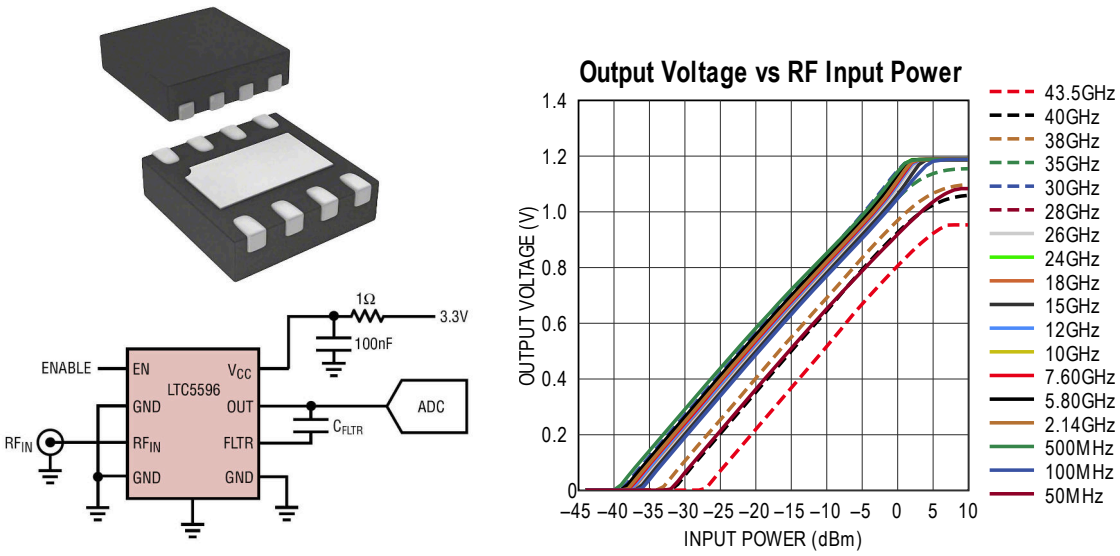

Figure 4.3: DFN8 Package (2 mm × 2 mm) and typical circuit (left) and the responsivity curve of Analog Devices LTC5596 powermeter (right), as specified in the datasheet.

levels to detect with a detector. Therefore, the measurement setup is feasible with these dimensions and transmitted power levels.

4.2. Sensing Element

In order to keep the system complexity to a minimum, it is preferred to process the high frequency signals as soon as possible. To keep the high-frequency circuitry to a minimum, the signal is measured right after the detector antenna.

A type of sensor needs to be chosen for the detector. To keep the complexity to a minimum, only power is measured. For this, a powermeter is the most logical choice. This device, also known as a radiometer, senses the effective RMS power over a large bandwidth. Note that the proposed concept allows for measurement of other properties (e.g. phase, EVM). Once again, to keep the complexity low, an off-the-shelf (OTS) component is used. The spectrum of commercially available high frequency RMS powermeters is limited, only two devices were found that cover the frequency band up to 40 GHz: LTC5596 by Analog Devices and MADT-011000 by Macom. They have a comparable dynamic range (DR) of 35 dB and 30 dB, respectively. Regardless, the Analog Devices option is preferred because it is capable of measuring signals as low as −35 dBm in contrast to −15 dBm of the Macom one.

The LTC5596 has a Linear-in-dB response in the input range of −35 dBm to 0 dBm over the frequency range of 0.1 GHz to 40 GHz, as shown in Fig. 4.3. This linear relationship eases processing as only a DC voltage up to 1.2 V has to be measured at the output. At the RF input, a coplanar waveguide (CPW) transmission line is preferred to connect the receiving antenna to the IC.

To display the working principle of this project, the described power levels and dynamic range suffice. In case more sensitive measurements are wanted, a high frequency low noise amplifier (LNA) could be added before the powermeter. Alternatively, a more sensitive powermeter or even a multi-stage setup

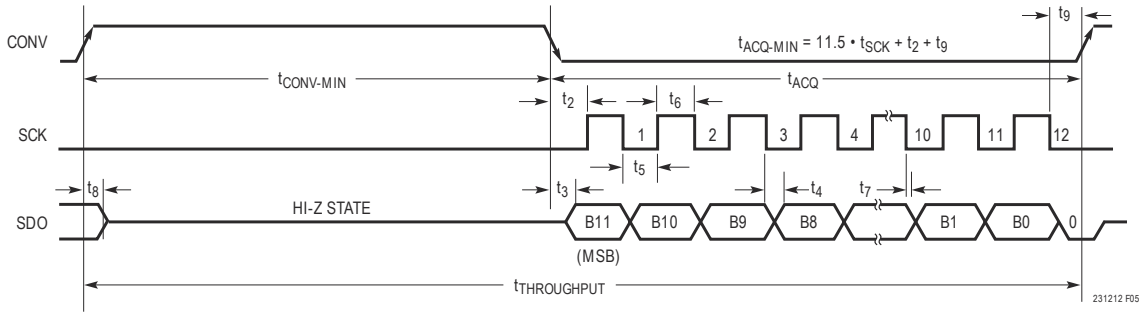

Figure 4.4: Timing diagram for readout of the ADC2312-12 ADC. The conversion (CONV) and clock (SCLK) lines are inputs and the resulting serial data is applied as output on SDO.

(i.e. one for low and one for high powers) could be researched.

4.3. ADC

In order to process the DC voltage from the powermeter, an Analog-to-Digital Converter (ADC) is implemented with every detector. This digital signal is read out in series, for which the readout protocol is discussed in the next chapter. The setup needs to read out in seconds, thus a high sample rate is not required.

The 12-bit, 500 ksps, single-ended LTC2312-12 of Analog Devices is chosen, in favor of its simplicity. The IC has only eight pins and operates at either 3.3 V or 5 V. Using a 3.3 V supply, an internal reference voltage of 2.048 V is generated, which corresponds to a resolution of 500 µV per count. Considering the responsivity slope of 34.12 dB/V of the chosen powermeter, an RF accuracy of 0.02 dBm is achieved.

The product series, which have identical pinouts, offer versions with higher digital speeds (0.5 Msps to 5 Msps) and resolution (12-/14-bit). The lowest of both options is chosen as it provides sufficient performance and is the cheapest.

The ADC outputs a ”SPI-compatible” serial communication protocol, specified in the datasheet as shown in Fig. 4.4. The conversion (CONV) pin is used to perform a conversion on a rising edge, which is read out after a falling edge. It operates slightly different from the SPI protocol, as SPI uses a Chip Select (CS) pin in place of CONV, which needs to stay high during readout.

4.4. Receiving Antenna

In many of the researched publications where a scanning antenna is used, a standard gain horn antenna or comparable solid metal antenna is used. While this is affordable in the case of one probe, it becomes very expensive for a multi-probe setup. Therefore, a more low-cost solution is considered. The scope of options is limited to PCB or on-chip antennas, as these are co-integrated with the signal processing and therefore minimize cost. Since the incoming signal is unknown, a wideband antenna is preferred which responds to any polarization. Lastly, a high gain is beneficial for compensation of path loss.

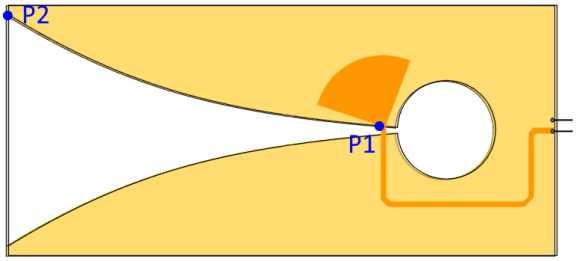

Figure 4.5: Example of a vivandi antenna. The feed line is on a separate layer. The substrate material is white in this picture. Points $P1$ and $P2$ for the exponential equation are shown. Source: `http://www.radartutorial.eu/06.antennas/Tapered%20Slot%20Antenna.en.html`

4.4.1. Vivaldi antenna Design

The stated requirements resulted in the choice for a Vivaldi antenna. This type of antenna is invented in 1978 by Peter Gibson [44], presumably named after the Italian composer. It consists of a tapered slotline which opens up in a trumpet-like shape. Its working is best understood by perceiving the antenna as a cross-section of an exponential horn antenna. An example is shown in Fig. 4.5. The antenna width and length need to be chosen to suit the frequency band and required gain level. The inner taper edges start at $P_1\ (x_1, y_1)$ and end point$P_2\ (x_2, y_2)$ are expressed by

$$f(x) = \pm\left(c_1 e^{Rx} + c_2\right) \tag{4.3}$$

with

$$c_1 = \frac{y_2 - y_1}{e^{Rx_2} - e^{Rx_1}}, \tag{4.4}$$

$$c_2 = \frac{y_1 e^{Rx_2} - y_2 e^{Rx_1}}{e^{Rx_2} - e^{Rx_1}}, \tag{4.5}$$

and taper rate R.

This type of antenna is used in many fields where a wideband and high gain receiver/transmitter is needed. It is therefore not surprising that there are many publications to improve performance [45]. Some achieve this improvement by implementing wideband line terminations, using an alternative tapering shape [46–49] or an alternative PCB layer configuration [50]. The Vivaldi antenna is used often in an array following an egg-crate structure [51–53].

Under normal operation, the Vivaldi antenna has a strong linear polarization. In order to measure any incoming polarization, a two-antenna setup is needed. The two boards need to be perfectly perpendicular to each other and ideally on the same position. The total power is determined by calculating the vector combination of the two.

With the design of any antenna, there are many geometrical freedoms and fixing these in the right order is crucial for correct operation. To design the antipodal Vivaldi antenna, a structured approach is utilized, which is discussed now.

Since the antenna is a passive component, its performance as a transmitter or receiver is identical following the rules of reciprocity. The antenna is considered to be a transmitter during the design procedure, since it is more intuitive and easier to simulate.

The RF PCB technology used is the Rogers RO4350 ceramic laminate, which is available at manufacturer Eurocircuits. The offered board thickness is 0.25 mm and 0.5 mm, the latter is chosen to minimize PCB bending. The dielectric constant is $\epsilon_R = 3.66$.

To research options for the antenna, the 3D EM simulation software suite CST by Dassault Systems is used. Initially, the setup of Fig. 4.5 is considered, where the slot of the antenna is fed by a microstrip to slot transition. Although possible, it turns out that there are multiple complexities to this technique: both the microstrip and slot need wideband termination at the open end and the slotline becomes very small (≈0.1 mm) in the selected technology. A variation of the Vivaldi antenna is preferred; the Antipodal Vivaldi antenna. Instead of having two conductors on the same layer, one is placed on either side of the PCB, hence its name. This opens up the possibility to transition into a parallel microstrip line. This avoids the need for a slot and immediately makes the in/output connection available in the metal, which is be fed into the selected IC. One of the two sides is extended into the ground plane to end up with a grounded microstrip.

To get the best antenna performance, the tapered end is modeled first as stand-alone, with a waveguide excitation on the parallel microstrip in the simulation model. It is optimized for return loss $S_{11} < -10$ dB and high gain, i.e. $G_A > 10$ dBi, in frequency band 20 GHz to 50 GHz.

The first parameter to set is the characteristic impedance of the parallel microstrip. The most important here is to match the antenna to the powermeter impedance of 50 Ω, such that $Z_S = Z_L^*$. A first approximation for the dimension is made by using a standard (grounded) microstrip calculator, this resulted in a width of 1.2 mm. Some trial using simulations resulted in $Z_0 = 50\,\Omega$ for a parallel stripline width of 0.9 mm, which is used from here on. Secondly, the inner tapers are optimized for the highest gain at the bandwidth of interest. This resulted in an inner antenna length of 30 mm × 10 mm, with taper rate $R = 0.1$. The same is done for the outer taper, which is set at 30 mm × 15 mm and $R = 0.63$. A drawing of the antenna with all the dimensions noted is added in Appendix A.

The resulting antenna is shown in Fig. 4.6, with the $S_{11} < -10$ dB shown in Fig. 4.7, indicating that almost all the energy is radiated. The oscillating trend visible on this graph is related to the remaining parasitic waves, for which the metal behaves as a transmission line. At specific frequencies, these waves are observing varying a impedance, related to the antenna's length. The radiation patterns of both polarizations is shown in Fig. 4.8.

In order to read out the received signal, a transition into the footprint of the powermeter IC is required, which prefers a grounded coplanar waveguide (GCPW). To achieve this, a gradual transition is used to minimize reflections. The bottom layer expands into the ground plane and the top layer tapers into two planes which are connected with vias to the ground plane. A close up of this is visible in Fig. 4.9.

The antenna is exited (or actually receiving) on one side of the PCB. The waves are located fully between the top layer metals. Any fields in the substrate are blocked by the wide ground plane. This

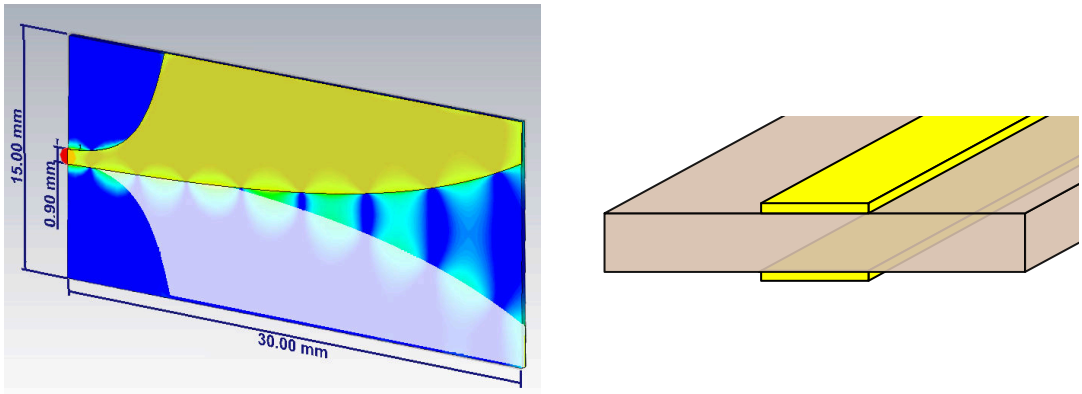

Figure 4.6: Standalone antenna taper (left) with the elecric field shown, and the parallel microstrip connection (right), the substrate is shown transparent such that the second layer is visible.

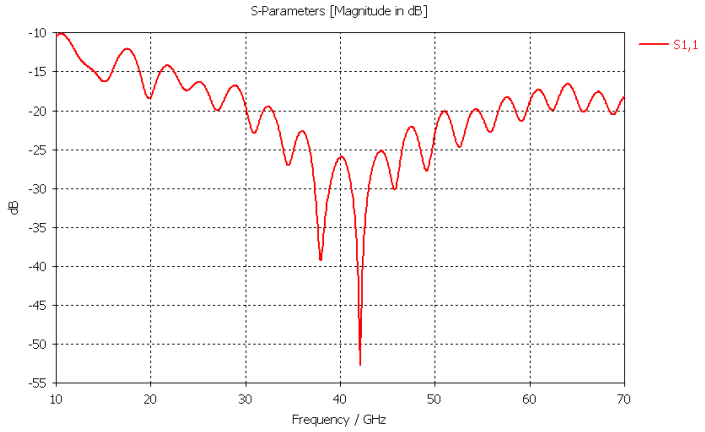

Figure 4.7: The corresponding S11 parameter of the standalone antenna taper, normalized to 50 Ω.

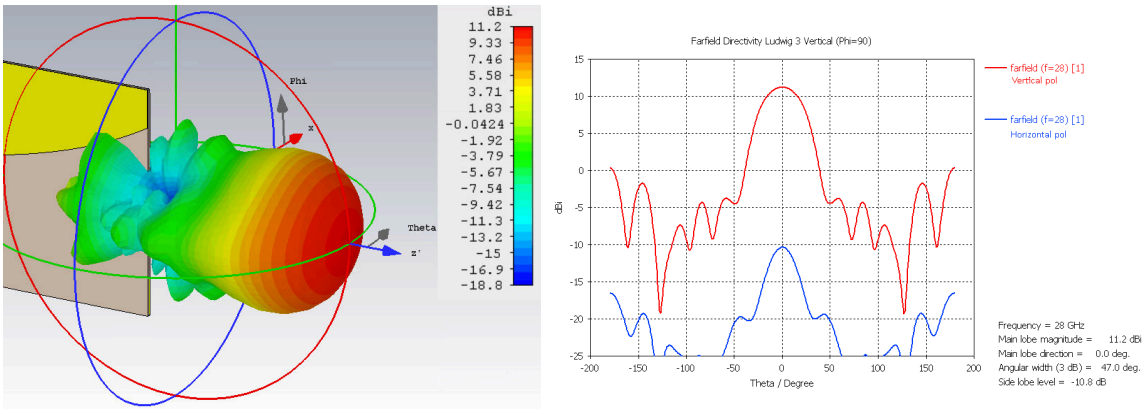

Figure 4.8: Stanalone antenna performance at 28 GHz. On the left, the 3D Radiation pattern of the co-polar signal is shown and on the right a cross section of the co-polar and cross-polar directivity (left) is shown. Note the peak gain $G_A = 11$ dBi and $SLL < -15$ dB.

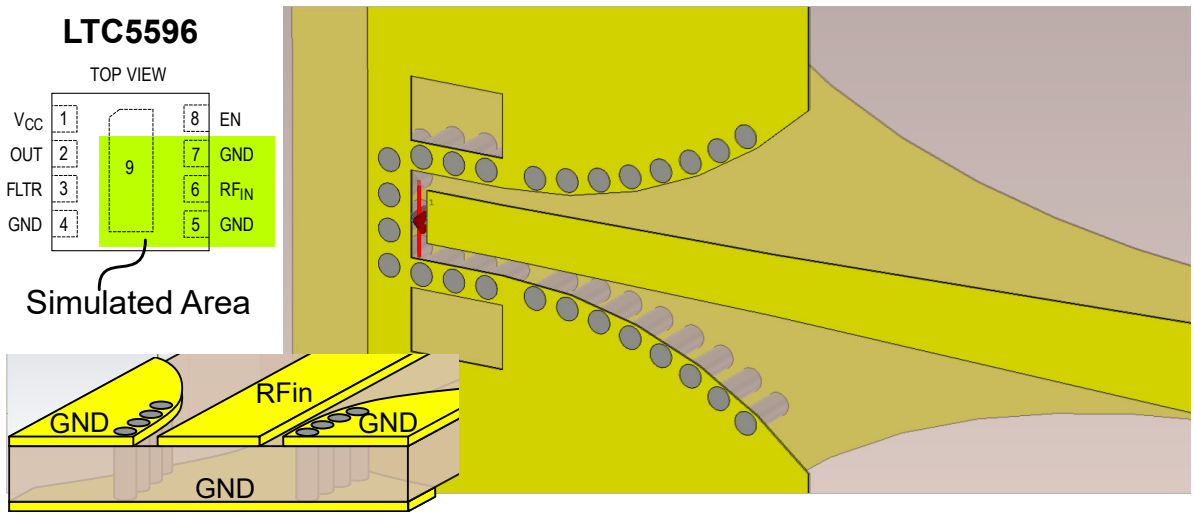

Figure 4.9: Sketch of the GCPW structure with tapering to parallel stripline. The lumped feedpoint for simulation is positioned on the red arrow.

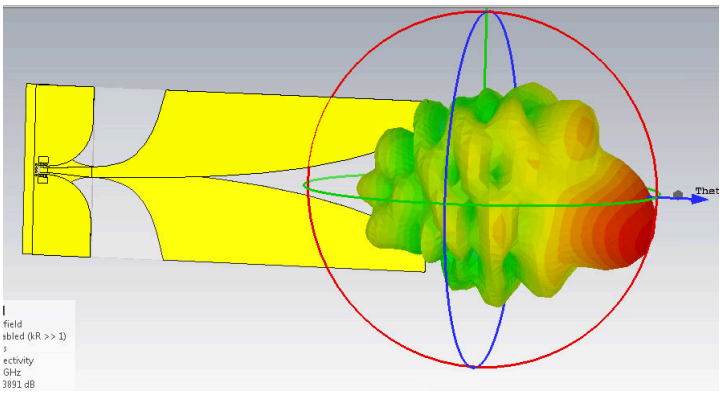

Figure 4.10: Short connection between GCPW and antenna, resulting in a slanted main beam.

results in a unbalanced signal, while the antenna expects a balanced signal. Therefore, the region between the GCPW and the antenna needs to be considered as a balun (balanced-to-unbalanced transition). Making this connection very short results in an unsymmetrical antenna pattern; the main beam is not centered. An example of this is visible in Fig. 4.10. Extending the interconnect a bit (approximately 10 mm), as shown in Fig. 4.11, results in a properly balanced circuit.

The final design made for the antenna is shown in Fig. 4.12. Two other improvements are visible, inspired by some of the previously stated publications on Vivaldi antennas.

In many publications, the substrate at the radiating side is extended to create a dielectric lens [50, 54]. To test this hypothesis, an experimental simulation is made in which a 100 mm extension is added, as shown in Fig. 4.13. This results in a big improvement of 10 dB radiation pattern as shown in Fig. 4.14. This long addition proves how the dielectric lens tunnels the waves toward the center. To implement this on the antenna in a more practical way, a length of 25 mm is added such that a 3 dB improvement in gain is obtained.

Secondly, a comb structure is applied on the outer edges. Ideally, this region should not contain

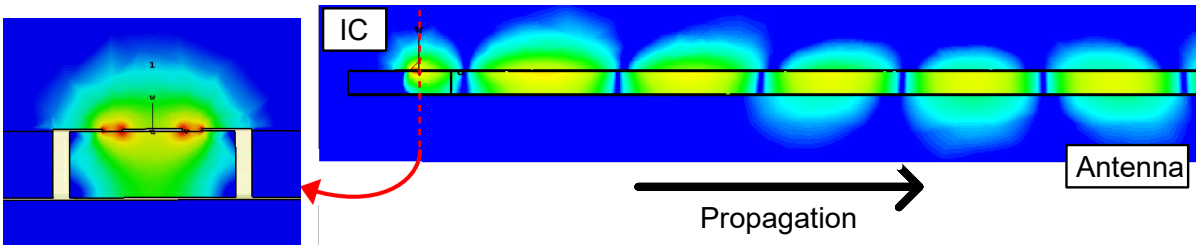

Figure 4.11: Cross-section of an extended mircrostrip line, showing the electric fields in the transition from unbalanced to balanced.

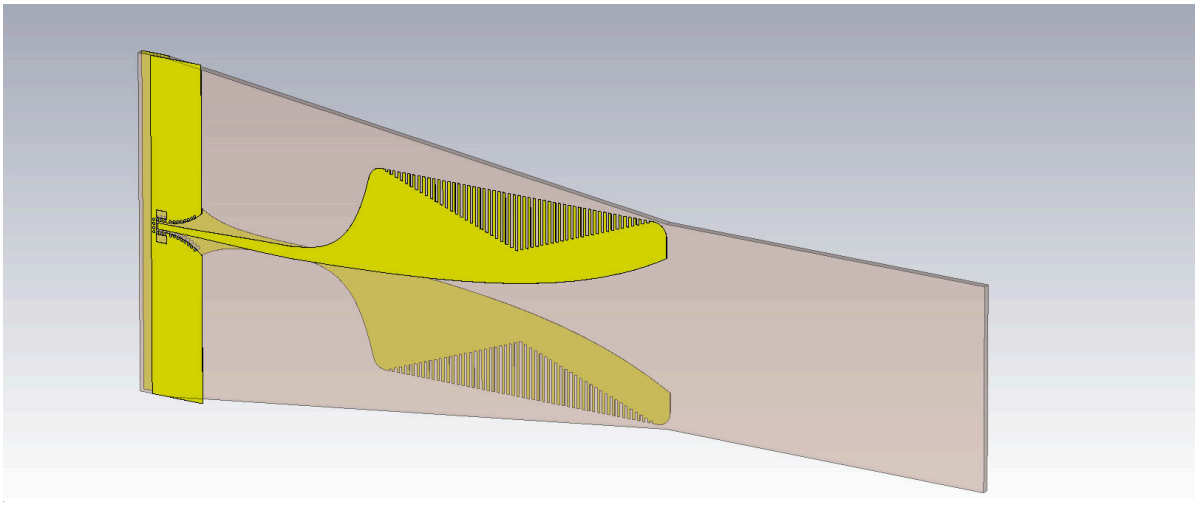

Figure 4.12: Full antipodal vivaldi design, as modeled for simulation in CST. The substrate is shown transparent.

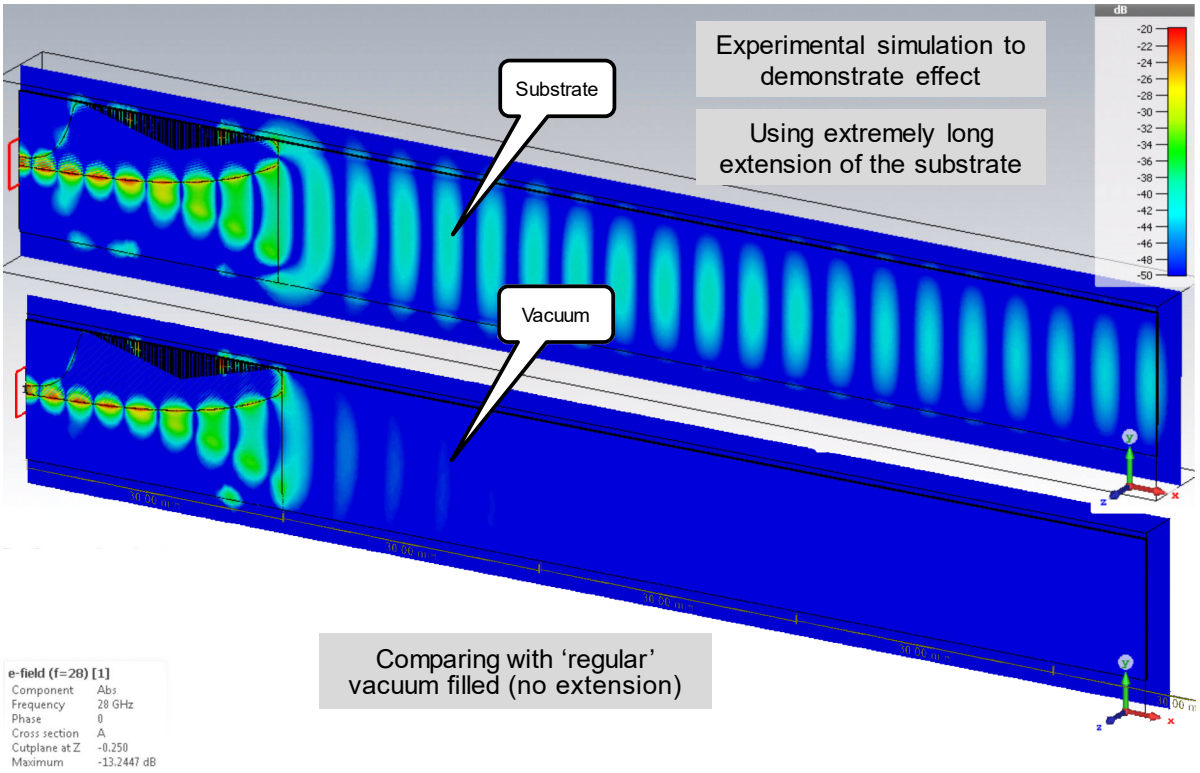

Figure 4.13: Extending the substrate for 100 mm results in the electric field shown on top. For reference, the bottom antenna shows the fields without any extension. To assure correct simulation, both cases are running in the same bounding box.

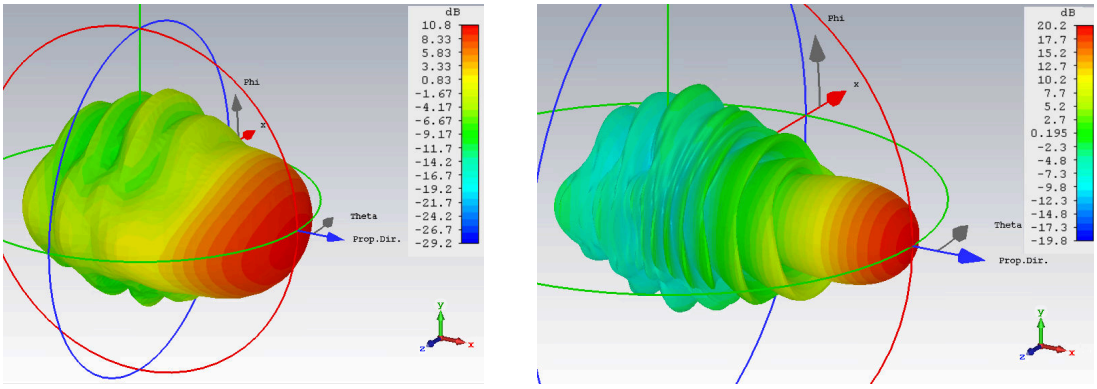

Figure 4.14: Impact of adding the experimental substrate extension. Left shows the pattern without an extension and right shows it with 100 mm extra. A significant improvement in gain of 10 dB is visible.

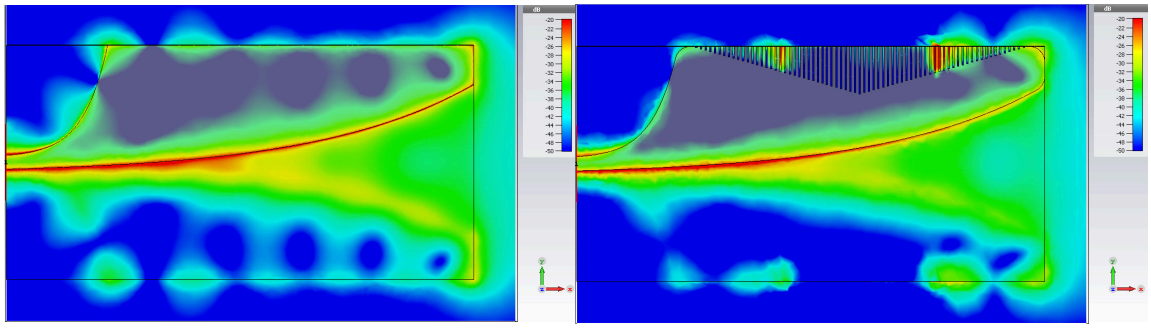

(a) Vivaldi antenna without corrugation. transmitted Waves are folding back around the sides creating unwanted parasitics.

(b) Vivaldi antenna with corrugation on the sides.

Figure 4.15: The average E-field is shown on the antenna for 28 GHz.

any fields at all; the waves should be radiated instead of curving around. In practice, a small part of the energy curves around the sides, as shown in Fig. 4.15a. This results either in radiation at the sides or power returned to the input, which are both unwanted. To terminate any remaining waves, slots of $\lambda/4$ length and 0.2 mm width are placed here. Since the antenna operates at a wide band of frequencies there are various lengths used, up to 4 mm. In Fig. 4.15b, it is visible that the waves are blocked at a specific wavelength. The impact of this improvement is shown in Fig. 4.16. The sidelobes are reduced significantly and the gain improves with a few decibel, presumably due to better input matching.

The simulated performance of the antenna is discussed now. The copolar and crosspolar radiation patterns are shown in Fig. 4.17. A cross-polarization isolation of 20 dB is achieved. Furthermore, the return loss S_{11} and realized gain G_{re} are shown in Fig. 4.18. All of these properties are within requirements and the high realized gain of 15 dB is very beneficial for measuring weaker parts of the AUT.

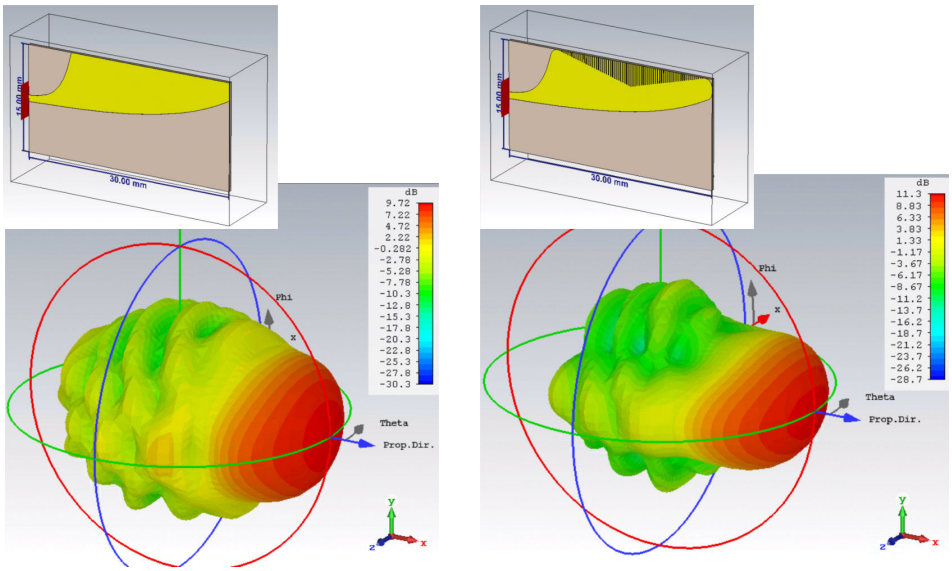

Figure 4.16: Impact of adding the side combs on the board, left versus right. The absolute value of the realized gain at 28 GHz is shown.

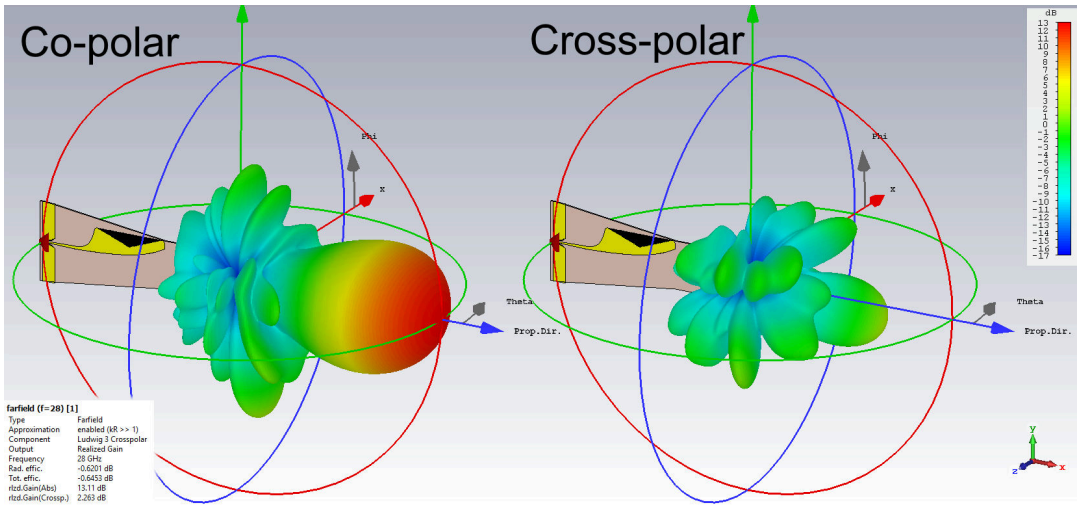

Figure 4.17: Radiation pattern of copolar (left) and crosspolar (right) patterns. The realized gain is shown.

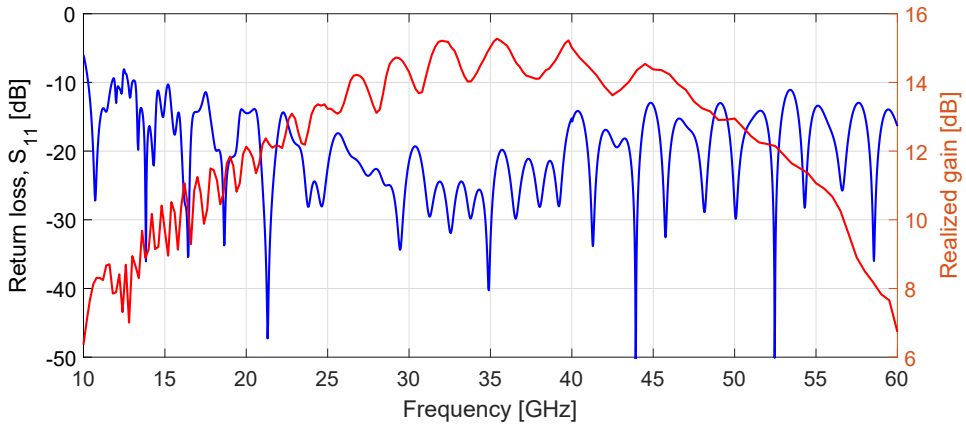

Figure 4.18: The simulated return loss and realized gain of the full antenna design.

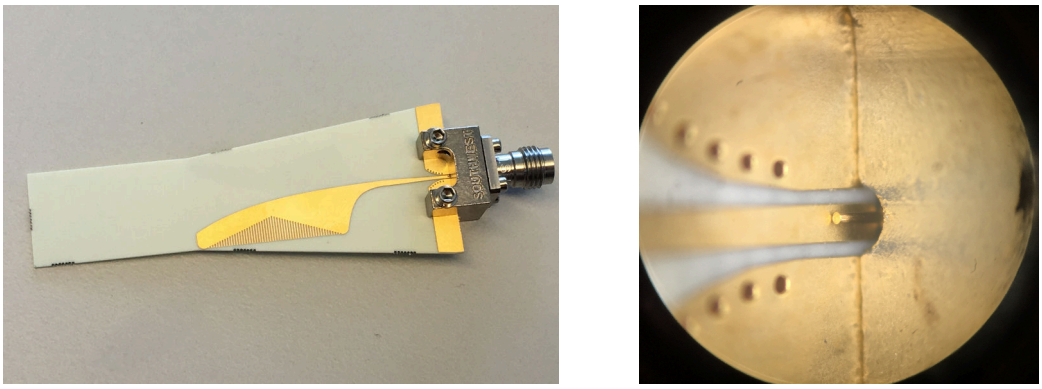

Figure 4.19: Standalone vivaldi antenna. Identical to the full antenna, except that it is cut at the IC pad edge. A micrograph of the connector to PCB interface is also shown.

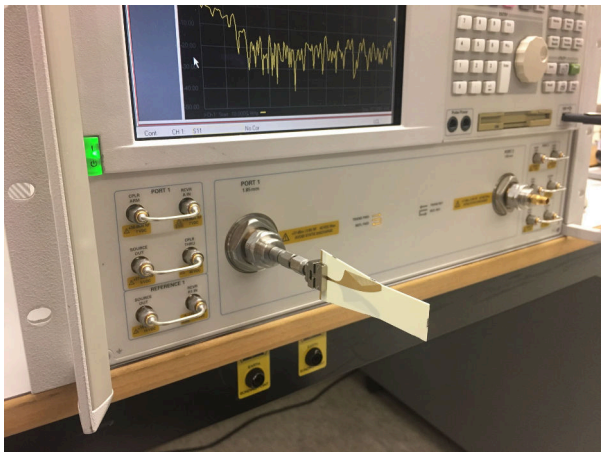

Figure 4.20: Configuration for measuring S_{11}.

4.4.2. Antenna fabrication and verification

The antenna is realized on the earlier described RO4350 substrate. The fully populated board does not easily allow verification of radiation performance, since the antenna feeds directly into the powermeter. Therefore, a standalone antenna with a coaxial connector is also fabricated and is discussed first. A picture of it is shown in Fig. 4.19 and the full layout is added in Appendix A. By cutting the board at the IC pads, the GCPW is accessible on the edge. The connector used is a female 1.85 mm end launch connector by Southwest Microwave, model 1892-04A-5. It is mounted on the side of the board and the feed is press-fit on the PCB, without any soldering. Coincidentally, the GCPW structure dimensions exactly match up with the connector. The 1.85 mm coax is capable of operation up to 67 GHz.

The performance of the standalone antenna is verified using the Agilent E8361A 67 GHz VNA. To measure the impedance matching quality, the antenna is directly connected to the instrument, as shown in Fig. 4.20. After one-port calibration, the return loss S_{11} is measured as shown in Fig. 4.21. It corresponds with the simulations and is far below -10 dB over a wide bandwidth.

In order to measure the realized gain, an antenna link is made with two identical Vivaldi antennas,

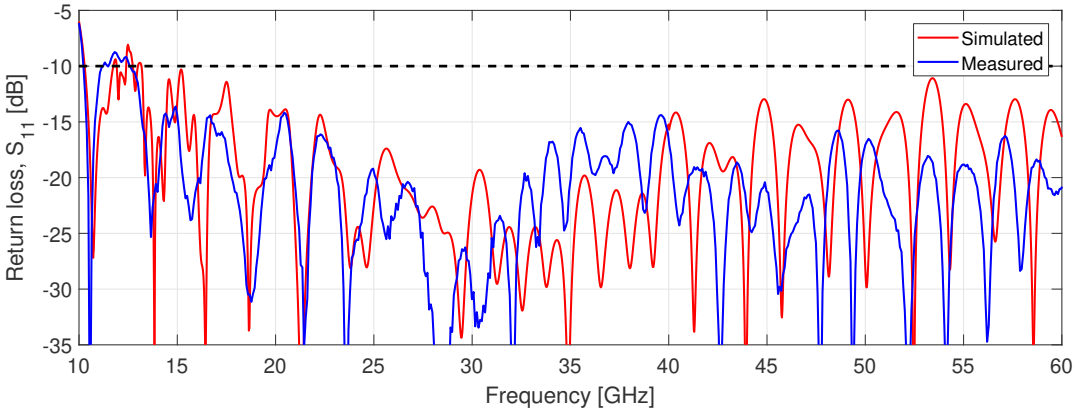

Figure 4.21: Simulated versus measured return loss with the required $S_{11} < -10$ dB indicated.

as shown Fig. 4.22. The gain is calculated by rewriting Eq. 2.13 such that

$$G_T + G_R = P_R - P_T - L_{FS}. \tag{4.6}$$

Since we use two identical antennas it holds that $G_T = G_R$. Also, the insertion loss is set as $S_{21} = P_R - P_T$ which results in

$$G_A(R) = \frac{S_{21}(R) - 10\log_{10}\left[\left(\frac{\lambda}{4\pi R}\right)^2\right]}{2}. \tag{4.7}$$

The distance R is referred from the antennas phase center. This term is used in antenna design to describe the effective point from which the antenna starts to radiate.

The realized gain is obtained by aligning the antennas and positioning them at distances ranging from 15 mm to 215 mm, such that multiple values of $S_{21}(R)$ are measured. After calibrating the twoport system, the dataset of Fig. 4.23 is obtained. Analysis of the dataset showed that distance R is 25 mm from the antenna end, as shown in Fig. 4.22. Fig. 4.24 shows that this value results in good alignment of the S_{21} traces. Notice that the aperture plane is at the end of the metal, even though the dielectric taper is tunneling the waves. To get to the final gain curve, the average of the lines is taken, which is shown in Fig. 4.25. Note that the calculated value is not antenna gain in dBi, but the realized gain, which includes impedance mismatching and losses. The decrease of approximately 1 dB originates in the connector loss and mismatch, which are not taken into account with the simulation.

The last property to characterize of the standalone antenna is the radiation pattern. The designed antenna is a prime candidate for characterization in the proposed multi-probe setup. However, the setup is not functional if the sub-components are not finished. Thus, the pattern is measured using an existing scanning measurement setup. To get acquainted with measurement procedures, the antenna is placed in two different setups. These are the setups developed at TU Delft and TU Eindhoven of section 2.4, measuring in near field and far field, respectively. Since the setups are already explained, they are not discussed here. The used setups are shown in Fig. 4.26 and Fig. 4.27, respectively.

For the near field scanning setup a planar measurement plane is used. This requires probe com-

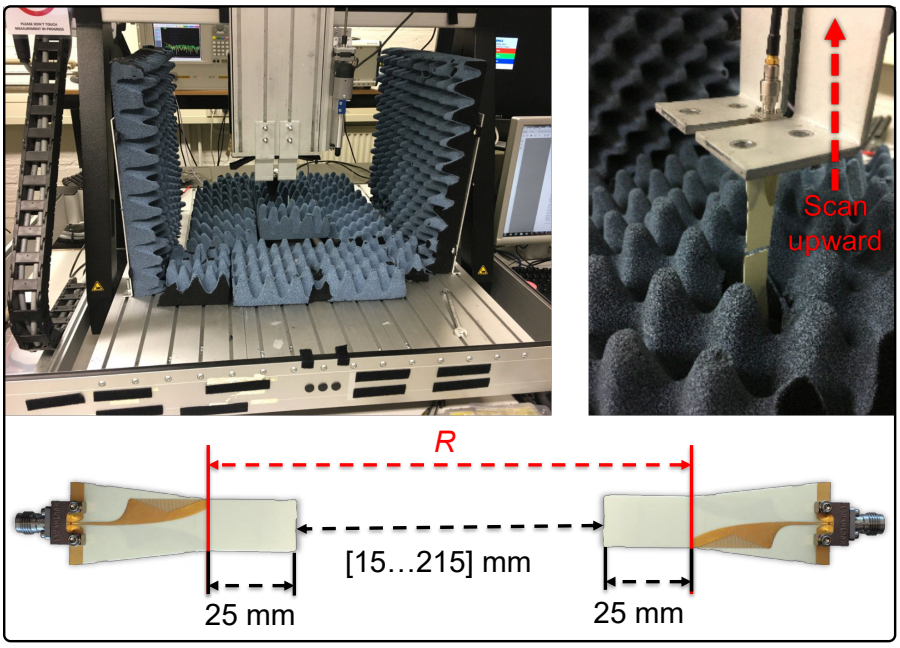

Figure 4.22: Setup used to characterize the antenna gain. Setting the phase center for path loss calculations to the shown distance R.

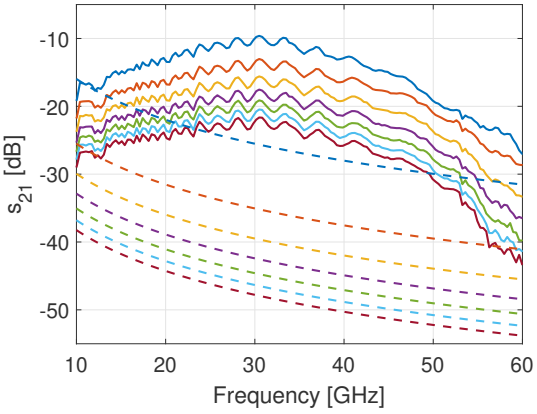

Figure 4.23: Measured S_{21} (solid) and corresponding calculated free space loss (dashed) when stepping distance from 15 mm to 215 mm, top to bottom.

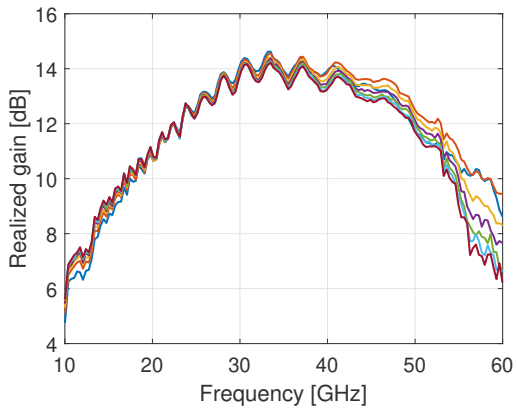

Figure 4.24: Measured realized gain, calculated by compensating distance sweep with its corresponding free space loss.

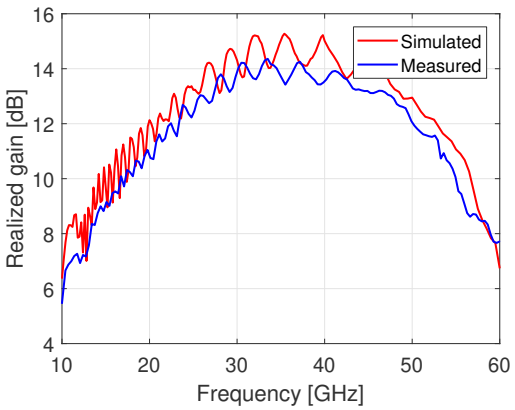

Figure 4.25: Final measured realized gain versus simulated realized gain.

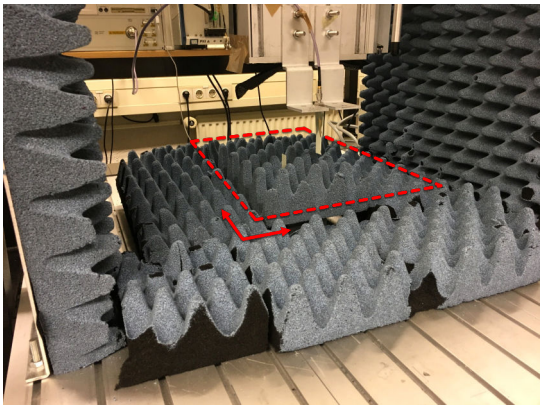

Figure 4.26: Near field Radiation pattern measurement setup of TU Delft [26], with installed Vivaldi antennas. The antenna on top scans over the indicated planar area.

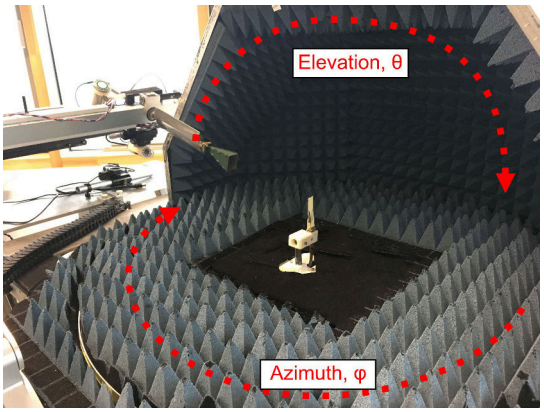

Figure 4.27: Far field Radiation pattern measurement setup of TU Eindhoven [34]. Setup with the Vivaldi antenna is shown. The gantry with 20 dB standard gain horn probe is rotated over the AUT.

pensation, since the probe angle of incidence depends on position. At the moment of measuring, there was no antenna available which covers the frequency band of interest. For this reason, the used probe is the same Vivaldi antenna. Since the antennas transmit and receive at the same angle, the only probe compensation required is to halve the S_{21} parameter. One inaccuracy that arises with this choice is that it is not possible to face two antennas from the same angle at all times; it is mirrored in either the X or Y direction. Therefore, the measurement results are not reliable for any non-symmetrical antenna pattern. Since the Vivaldi pattern is not symmetric apart from the main beam, the result shows some deviation. Furthermore, the data points at outer angles (i.e. $|\theta| > 45°$) are not very accurate since near field pattern requires filtering with a tukey window such that no harmonics appear when calculating the near-to-far-field transformation. This spatial windowing lowers the outer lobes a bit. Since these discrepancies alter the results, the measurement is only used for a rough verification.

The measurement performed on the far-field setup by TU Eindhoven [34] is considered to be more reliable. The data processing is very straight forward, since the probe antenna always has the same gain (i.e. it is always centered) the far field pattern is measured immediately.

The resulting two cross-sections of $\phi = 0°$ and $\phi = 90°$ are shown in Fig. 4.28, where $\phi = 90°$ is the cross-section aligned with the PCB board plane. Remember that the TU Eindhoven dataset is considered to be the valid measurement. The results look very promising; the main beam is quite similar to the simulated one, the side lobe level is at the expected $SLL < 15$ dB and the cross polarization isolation $XPD \approx 20$ dB at $\theta = 0°$.

4.5. Sensor Integration

The antenna, powermeter and ADC are combined in a single PCB assembly. To measure both polarizations, every measurement point consists of two antenna boards, perpendicular to each other. A 90° angle is preserved by soldering the two board edges together. Each board has an angled pinheader connector to feed power and communication. An image of the board is shown in Fig. 4.29.

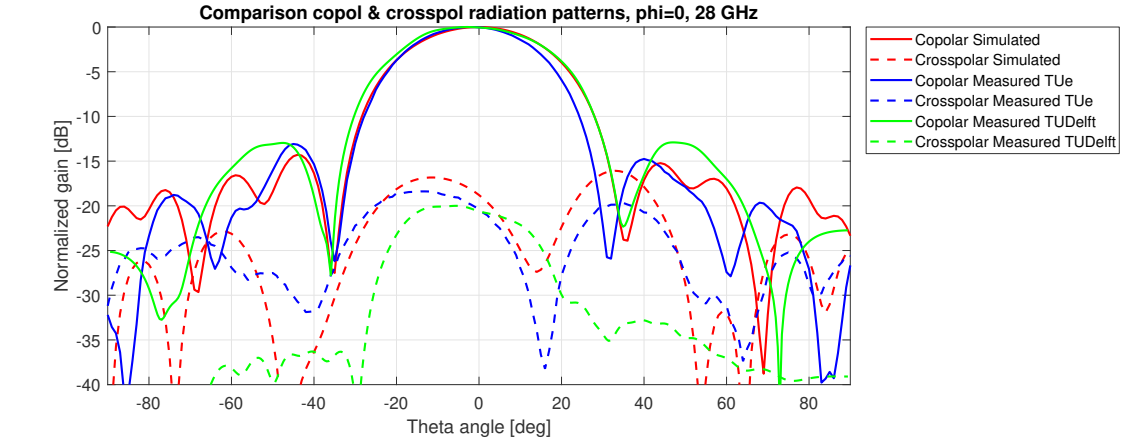

(a)

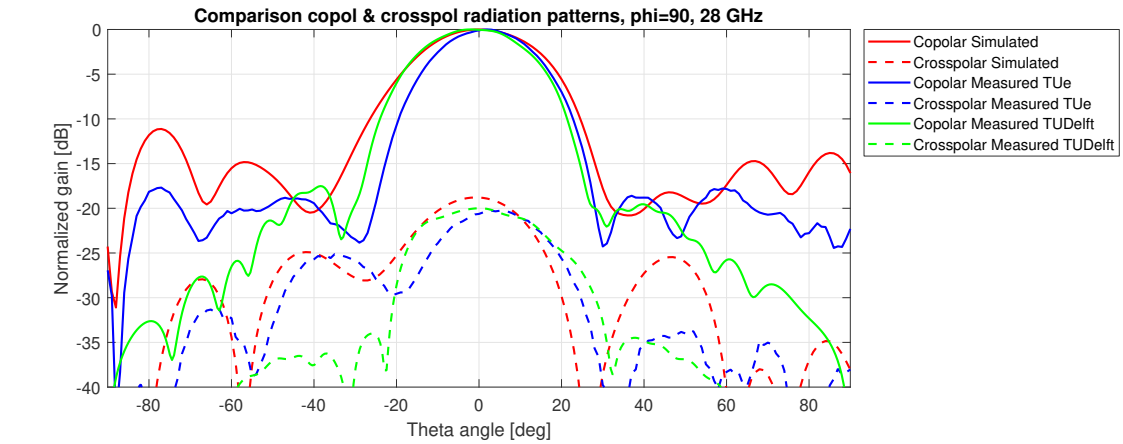

(b)

Figure 4.28: Measured radiation patterns using both measurement setups. Both the copolar and crosspolar patterns are shown.

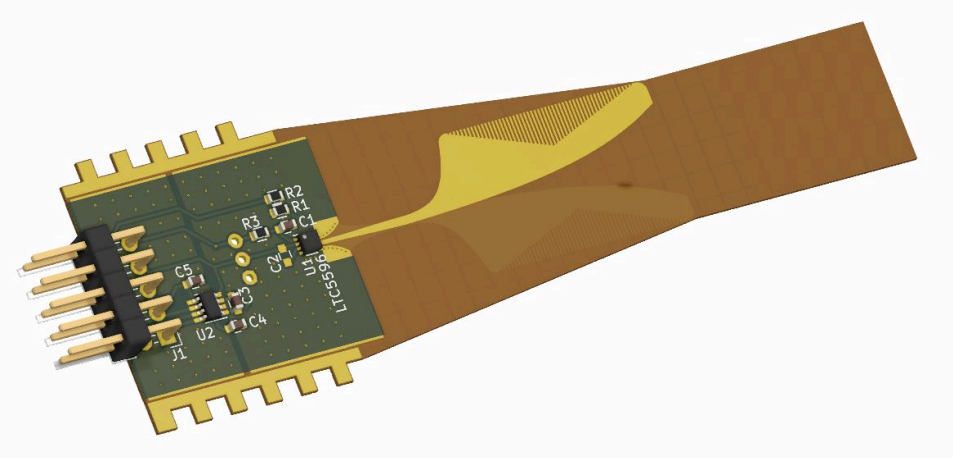

Figure 4.29: Developed Vivaldi powermeter board. On the connector, the ADC is read using the SPI connection. 3D preview made using KiCAD.

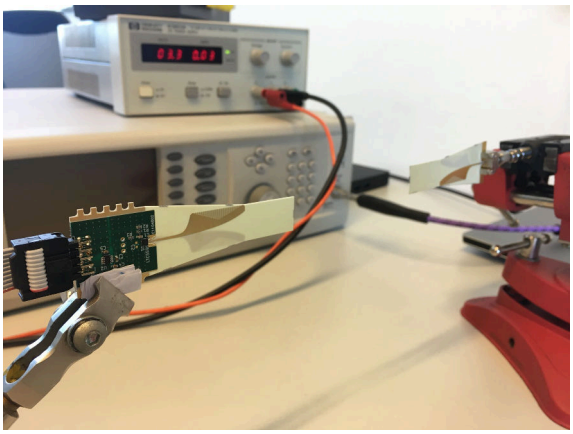

Figure 4.30: Test setup for the powermeter board. The receiving board on the left contains the powermeter and ADC, whereas the transmitting board on the right is a standalone antenna. The edge to edge distance is 10 cm.

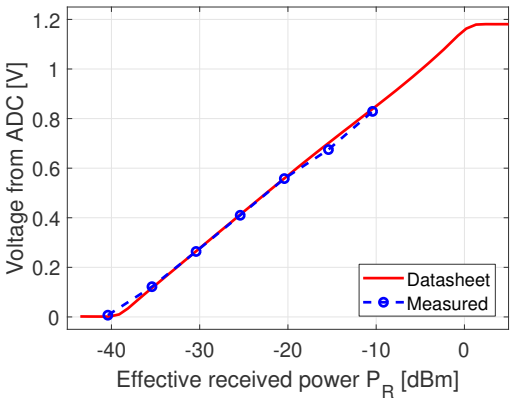

Figure 4.31: Measured power levels versus effective received power.

To verify proper performance of the board, a test setup is made where an input RF signal is varied in power. This way, the dynamic range of the powermeter with ADC is tested. The setup is shown in Fig. 4.30. A 28 GHz sine wave is generated on the Anritsu MG3694A 40GHz signal generator and transmitted using a standalone Vivaldi antenna. Using a spectrum analyzer the cable losses $L_c = 1.5\,\text{dB}$ are measured. With the known distance between the phase centers of $R = 15\,\text{cm}$ and the realized gain $G_T = G_R = 13\,\text{dB}$ (from Fig. 4.25), the effective received power P_R at the powermeter relative to the signal generator power level P_{SG} is calculated following

$$P_R = P_{SG} - L_c + G_T + G_R + 10\log_{10}\left[\left(\frac{\lambda}{4\pi R}\right)^2\right]. \tag{4.8}$$

The resulting power levels are shown in Fig. 4.31. The signal generator is able to generate signals P_{SG} from $-20\,\text{dBm}$ to $10\,\text{dBm}$, corresponding to P_R of approximately $-40\,\text{dBm}$ to $-10\,\text{dBm}$ using the stated equation. Within this range, the powermeter is able to measure the data correctly, as visible in Fig. 4.31. There is very good agreement with the specified responsivity curve at 28 GHz of Fig. 4.3. Unfortunately, the higher power range is not measurable with this setup, but it is found that this also works properly during measurements later on.

5

Dome Prototype

The developed sensors are used to set up the semi-spherical detector array. Two arcs with each 15 measurement points are made. This results in 29 probes, since the arcs have the center point in common. Each measurement point consists of two powermeter boards and one 'parentboard' on which the ADC value is transferred to the readout bus. This full setup is shown in Fig. 5.1.

5.1. Physical Setup

To mount these in a variable manner, a mounting rail is designed with holes at every degree. These are designed in Autodesk Fusion 360 and 3D printed on the Creality Ender 3. Fig. 5.2 shows how each arc consists of 20° segments which are pushed into one another. By designing the interconnects with tight tolerances, no screws are needed to secure the structure, although the holes are available in case this is required. For this project, the measurable far field distance is set at 50 cm, which allows measurement of a 5 cm aperture, or the category 1 of Fig. 2.8 at 28 GHz. To achieve a measurement distance of at least 50 cm, the dome radius is set at 60 cm to compensate for the Vivaldi antenna length.

Thanks to the chosen arc design, the angular distribution of the elements is chosen freely. In this case, the 15 boards on each arc are distributed over 180°, excluding the outermost $\theta = \pm 90°$ as these points do often not receive any power at all by an AUT. This resulted in the angular step size of 11.25° which is rounded to 11° such that it fits on the mounting rail. Therefore, the actual sample range coverage is $\pm 77°$. The parentboards are mounted with four bolts and spacers, which assures the boards to be perpendicular to the AUT. The antenna boards are connected using two 2x5 pin headers. This, in combination with the 90° soldered powermeter boards results in a very rigid setup and therefore guarantees that the main beam of the antennas always focuses on the arc center.

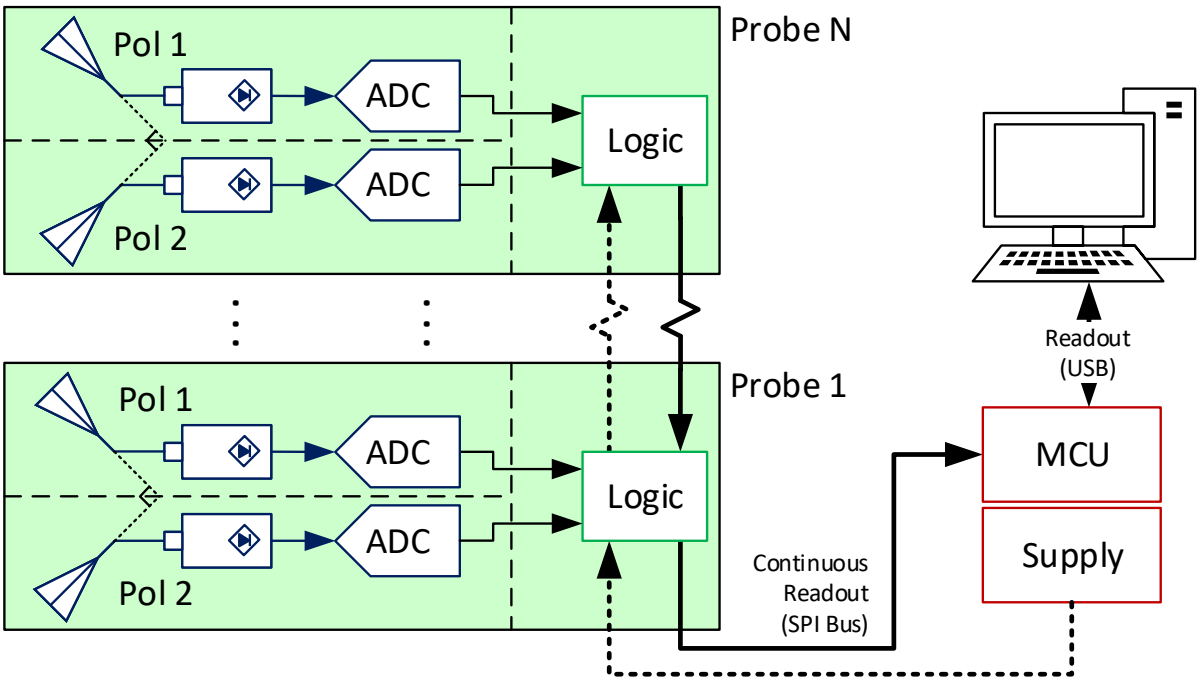

Figure 5.1: Setup used to read out all the antenna points.

Figure 5.2: Model of the 3D printed segments which are interlocked to make an arc, as shown on the right.

5.2. Communication and Control

The SPI protocol offered by the chosen ADC needs to be handled and read out in a convenient matter. To minimize complexity, a solution is created which does not require a microcontroller or FPGA at every measure point. The available ADC communication protocol supports the use of many boards in parallel, using the master-slave principle. Only the slave which receives a 'high' on the Chip Select (CS) pin is available. This enables the use of one clock and data bus which is common to every ADC.

One issue that arises with this principle is that every ADC needs an independent CS pin, which does not comply with the intended modular principle. To resolve this, a fragmented shift register topology is used to enable the boards one after the other. This is implemented using cascaded 74HC574 flip-flops; a single 'enable' bit is fed into the first board, after which it is shifted to the next board with a clock pulse. The powermeter is only needed during ADC readout; it is turned off using the enable (EN) pin while it is not needed. This is done with another shift register circuit, parallel to the shift register for the ADC. The explained topology is visualized in Fig. 5.3. The full PCB layout and timing diagram are added in Appendix A.

All these logic functions are implemented with discrete IC's on a PCB for every measurement point, which is called the 'parentboard' from here on. These boards are then daisy-chained such that easy assembly is possible without having to feed cables to every separate board for power and readout, as illustrated in Fig. 5.4. The chain of boards are interconnected using flatcables and fed into a single microcontroller unit (MCU). The MCU reads out the required number of boards and the data is acquired through a serial (UART) port on a PC, using the USB connection.

Almost any type of MCU would suffice for the readout of this system, since it only comprises of raising and lowering a few pins at the right time. In this case, a STM32Nucleo development board is used. In particular, the STM32L432KC is used. The board code is made using the online IDE mbed by ARM [55], which allows an Arduino-level of programming.

The microcontroller PCB is also the starting point for the 3.3 V supply line on each board. All the components chosen are able to operate at this voltage. The largest power consumer is the powermeter, which typically drains 30 mA when active. Furthermore, the ADC uses 3 mA and the current consumption of the parentboard logic IC's are negligible. Since only one powermeter is enabled at the time, the total current stays under 100 mA. Although the MCU is capable of supplying this, some extra margin is taken by adding a dedicated low-dropout voltage regulator (LDO) on the microcontroller board. A lab supply generates 5 V, which is regulated to 3.3 V by the LDO.

5.3. Physical Setup

The full setup requires a large amount of PCBs to be fabricated. To produce this efficiently, the boards are ordered in panels of six per parentboard panel and eight per powermeter board panel, allowing for semi-mass production. Also, a solder screen is added to apply the solderpaste easily. This allowed for fabrication and verification of all the 29 parentboards and 58 powermeter boards within one week. The

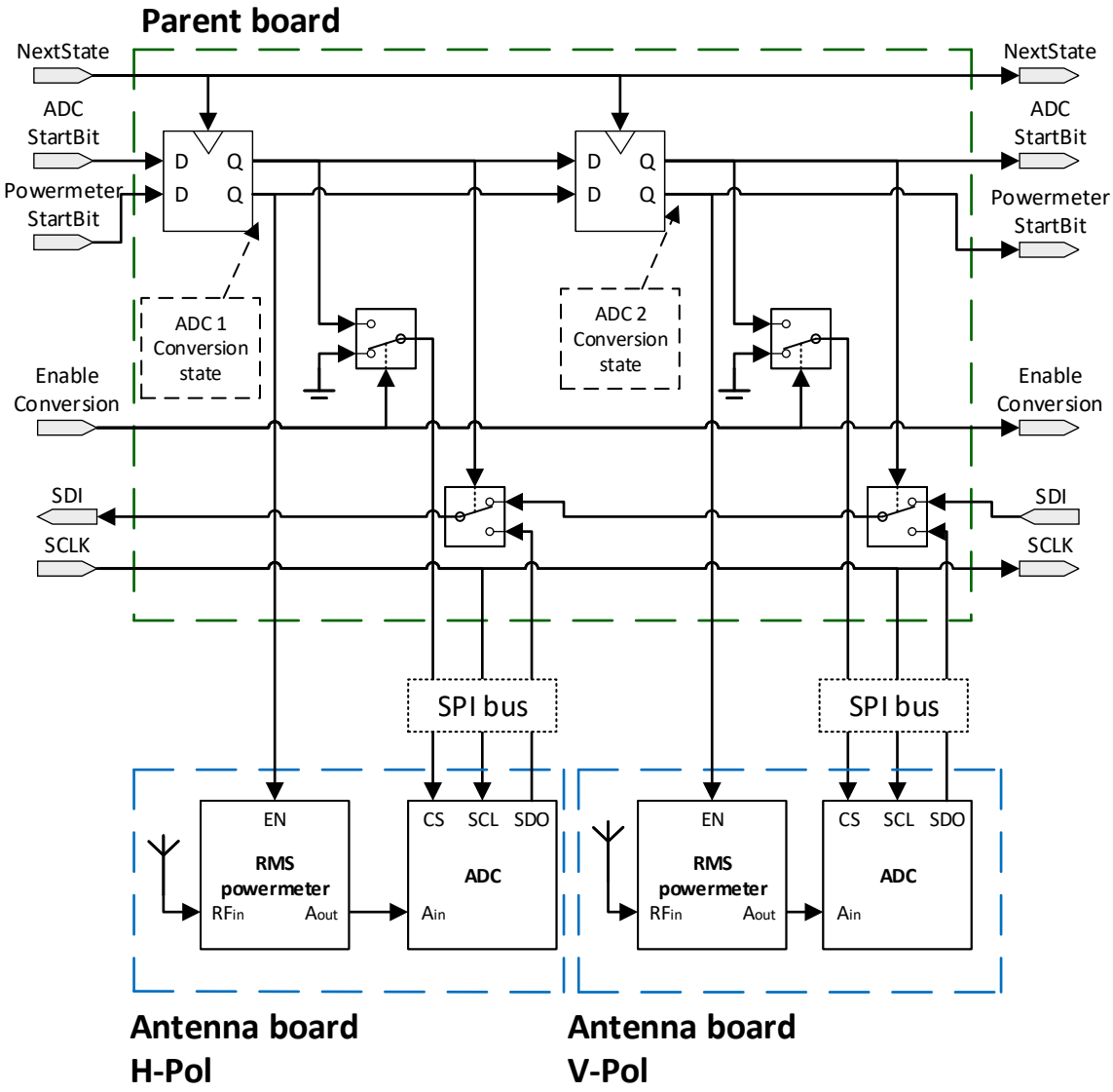

Figure 5.3: Flowchart of the designed readout circuitry. Each parentboard has identical in/outputs to adjacent boards (left/right) such that daisy-chaining is possible.

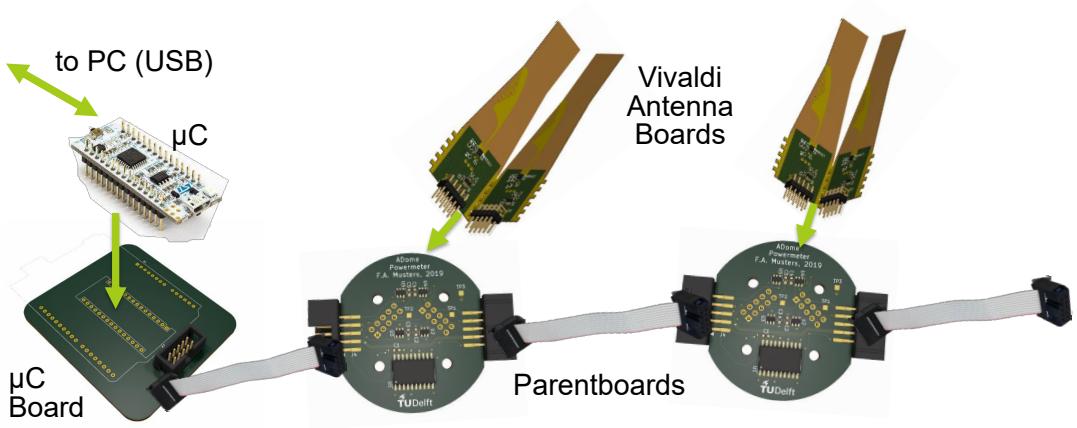

Figure 5.4: Illustration of complete assembly.

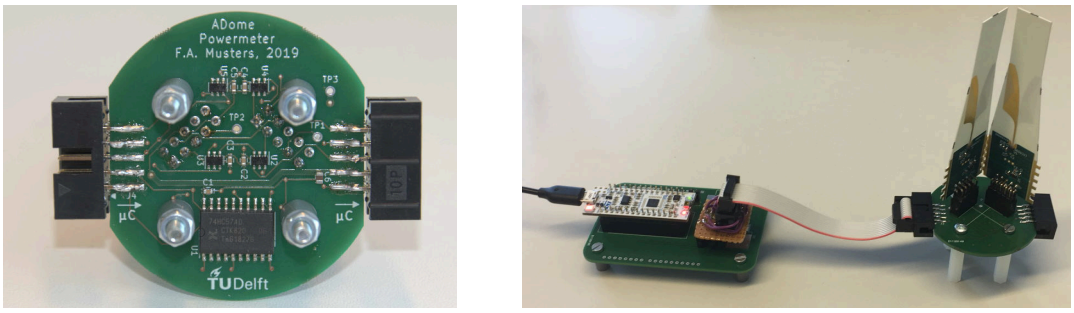

Figure 5.5: Picture of realized parentboard PCB. The parentboard diameter is 5 cm.

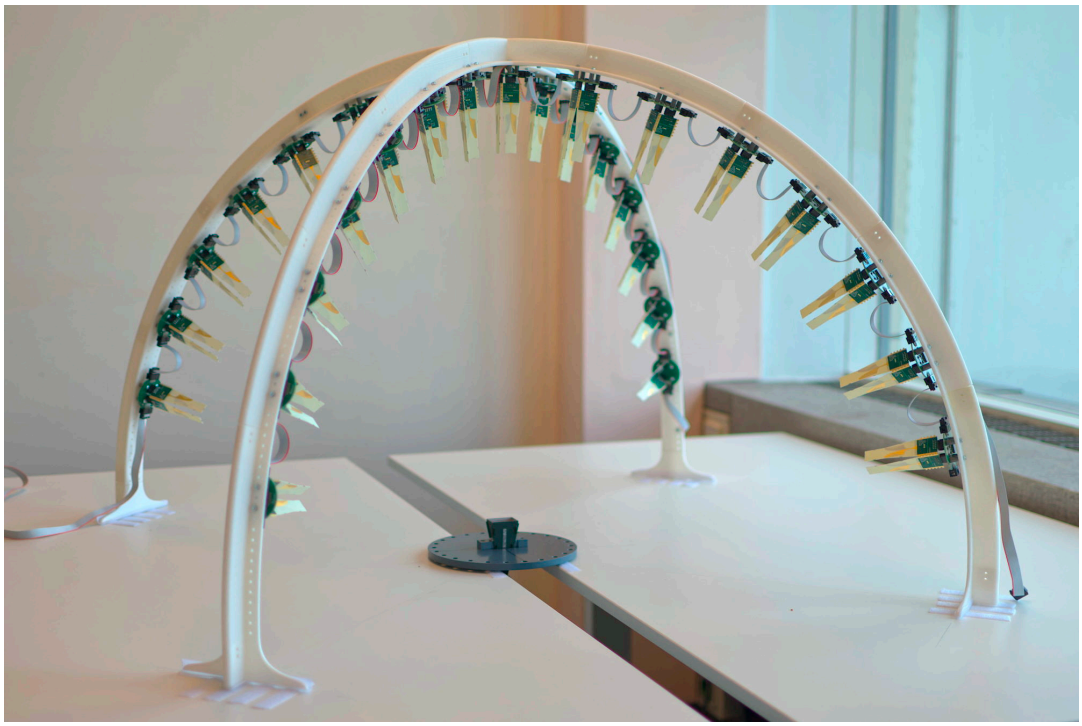

Figure 5.6: Complete prototype setup, including all connections. The setup is build on two desks, enabling a AUT holder to be positioned between them. In this case, a standard gain horn antenna is installed.

most difficult component to place is the powermeter IC, due to the eight pads being only on the bottom and its small size of 2 mm × 2 mm.

A picture of the fully assembled setup is shown in Fig. 5.6. Since the 3D printed frame tends to sag a bit, adhesive Velcro is used on the foots and table, making exact positioning possible and resulting in a sturdy setup.

The powermeter boards are read out using the proposed communication standards, the code is added in Appendix B. Since the boards are all connected through the ribbon cables, only the microcontroller board needs other connections, which are shown in Fig. 5.8. The two arcs are connected in series through one long ribbon cable, such that they act as one long string of boards for readout.

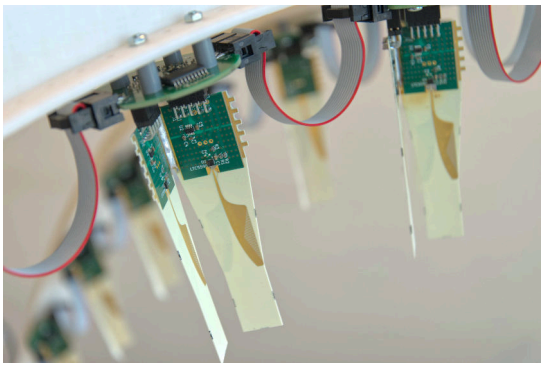

Figure 5.7: Closer view of the measurement boards.

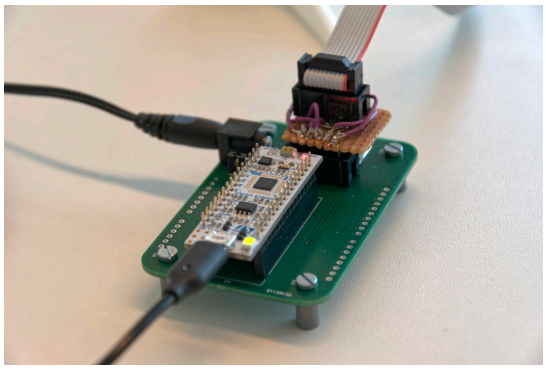

Figure 5.8: The developed microcontroller board. The micro-USB connection enables readout on the PC. The jack connection on the side allows power supply and the ribbon cable connects to the chain of powermeter boards.

Figure 5.9: Signal generator used for AUT signal generation. On top, the power supply for the amplifier is visible.

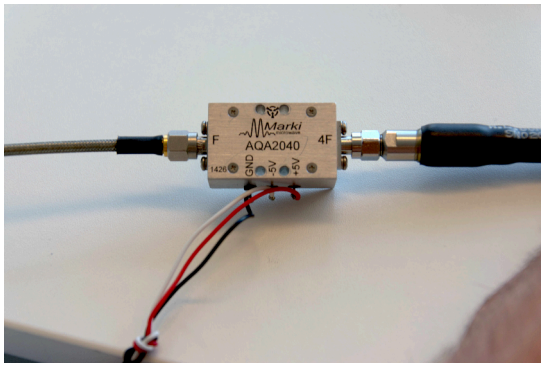

Figure 5.10: The AQA-2040RF amplified quadrupler.

5.4. Radiation Pattern Generation

The continuous wave (CW) signal for the AUT is generated with the Anritsu MG3694A 40GHz signal generator. In the powermeter verification of subsection 4.4.2 it is already observed that the maximum power output of 10 dBm only resulted in partial coverage of the dynamic range. In the full setup, this would mean that the sidelobes of the radiation pattern are below the detectable range of the powermeter. To amplify the transmitted signal, an RF amplifier is used. Since there is no separate amplifier available at the frequency band of interest, the microwave amplified quadrupler AQA-2040RF of Marki Mirowave is used. This device multiplies the input frequency by four and amplifies the input signal to 20 dBm. Therefore, the signal generator is set to 7 GHz to achieve 28 GHz at the AUT. The signal generator and supply for the amplifier are shown in Fig. 5.9 and the AQA-2040RF amplifier is shown in Fig. 5.10.

The generated signal is received at every powermeter, which is acquired by the microcontroller sequentially through every ADC. The 12-bit digital value is directly converted back into the corresponding analog voltage by

$$V_{ADC} = \frac{\text{counts}}{2^{12} - 1} \cdot V_{ref}, \tag{5.1}$$

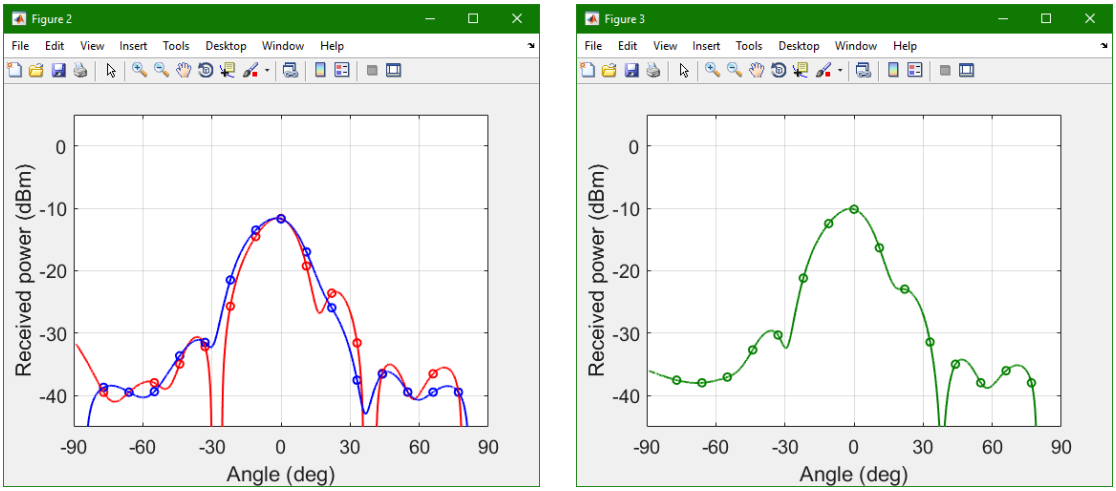

(a) The markers indicate the values measured at the two polarization boards (red/blue), the line is a interpolation between those points.

(b) The calculated vector sum of the two polarization boards. On this combined dataset, a new interpolation is performed

Figure 5.11: GUI in MATLAB used for real-time acquisition. The shown patterns are obtained within one second and updated continuously. The possible amplitude range is between −40 dBm to 0 dBm.

where $V_{ref} = 2.048\,\mathrm{V}$. This process is performed continuously. Optionally, any noise on the measurement can be averaged using a moving average filter. Using a serial COM port over USB, the ADC values is read out on request. To automate this, a MATLAB script is developed which polls the data automatically. This enables the real-time acquisition and plotting of datapoints.

The voltage in the range of 0 V to 1.2 V is converted to the measured logarithmic RF power of −40 dBm to 0 dBm by the responsivity curve shown in Fig. 4.3. Since each measurement point consists of two powermeter boards, one for each polarization, these are be received separately. To get to the absolute RMS power, the vector combination of the linear voltages is calculated using

$$P_{tot,lin} = \sqrt{P_{a,lin}^2 + P_{b,lin}^2}, \tag{5.2}$$

where $P_{a,lin}$ and $P_{b,lin}$ are the linear measured powers in watts of both polarizations.

In order to reconstruct the full radiation pattern from the measured points, an one or two dimensional interpolation is performed, for either a single cross-section or a full radiation pattern. Note that the spline interpolation is performed on the linear scale, as discussed in section 3.2.

A example of the MATLAB readout interface visible in of the powermeters is shown in Fig. 5.11. This interface updates continuously, taking less then one second to read out. Here it is visible why the amplifier is added; even with this improvement, the highest amplitude is still 10 dBm below the limit, resulting in a dynamic range of only 20 dB.

5.5. Verification of Measured Pattern

Using the described methods, the radiation pattern of a standard gain horn and Vivaldi antenna are obtained. These are shown in Fig. 5.12. The antennas are mounted in a disk with holes every 15°,

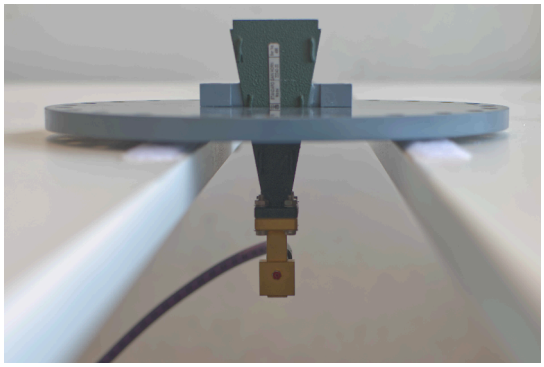

(a) Standard gain horn antenna with 20 dBi gain. Model 22240-20 by Flann Microwave.

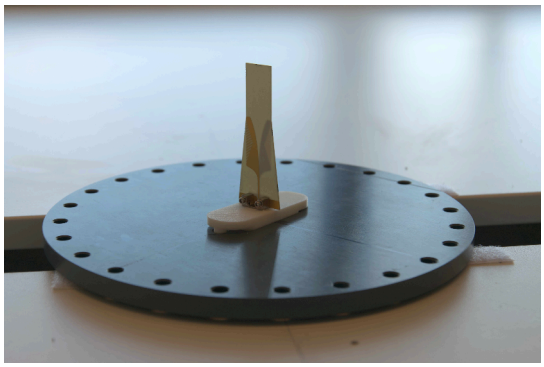

(b) Standalone Vivaldi antenna used as AUT.

Figure 5.12: The two AUTs used to test the setup.

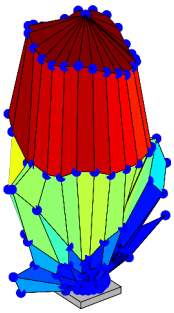

(a) Pattern acquired by sampling on the blue markers.

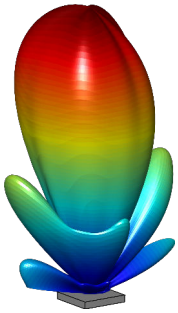

(b) Reconstructed pattern by interpolation on the linear domain.

Figure 5.13: Measurement performed on the standard gain horn antenna.

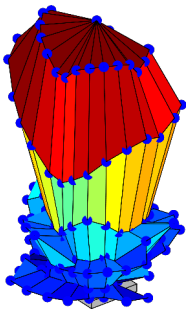

(a) Pattern acquired by sampling on the blue markers.

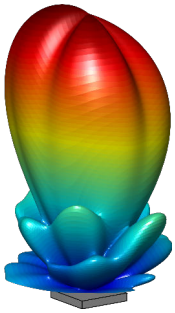

(b) Reconstructed pattern by interpolation on the linear domain.

Figure 5.14: Measurement performed on the Vivaldi antenna.

which is kept in place using adhesive Velcro. The absolute value of the two boards are taken as the resulting value. To emulate the measurement of a fully covering dome, the AUT is rotated in steps of 15°, of which the position is verified using the holes. This resulted in the 3D datasets shown in Fig. 5.13a and Fig. 5.14a. By performing a 2D interpolation on this data, the plots shown in Fig. 5.13b and Fig. 5.14b are obtained. Note that the interpolation is performed in the linear domain, resulting in the reconstruction of nulls. Since the dataset to interpolate is defined on the range of $\phi = [0, 360]\,\mathrm{deg}$ and $\theta = [0, 90]\,\mathrm{deg}$, the slope of the lines at the top point $\theta = 0°$ is discontinuous. This could be improved by using a different interpolation technique.

To better compare the measurements with known data, the acquired $\phi = 0°$ and $\phi = 90°$ cross-sections are considered versus the actual patterns in Fig. 5.15. In general, the reconstruction resembles the expected pattern. Most of the measurement points are accurate, but occasionally a deviation is visible. The accuracy is not always on point, specifically on regions with a large slope. This could be caused by the assumption that the two polarizations boards are on the same point, while in reality they have an offset of appoximately 2° from each other. Note that this data does not have any form of calibration, therefore any static offsets to the devices is not compensated for.

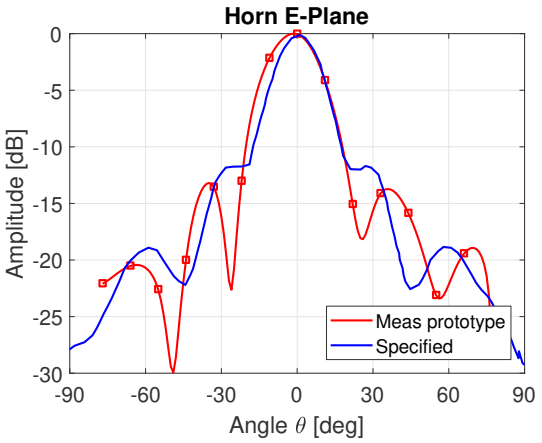

(a) The measured E-plane of a 20 dB standard gain horn, compared to the datasheet specification of a similar horn.

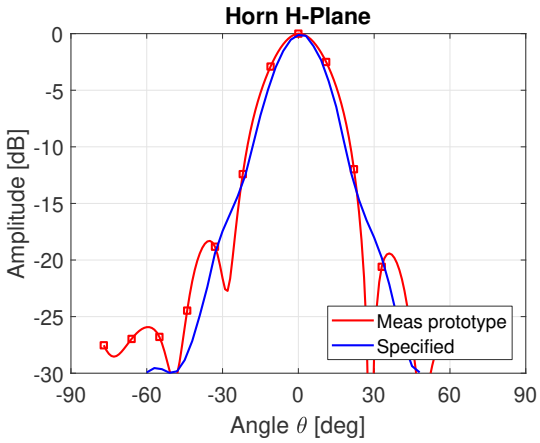

(b) The measured H-plane of a 20 dB standard gain horn, compared to the datasheet specification of a similar horn.

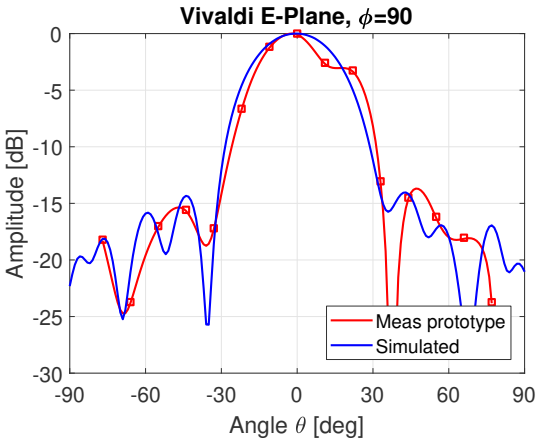

(c) The measured E-plane of a standalone Vivaldi antenna board, compared to the datasheet specification of a similar horn.

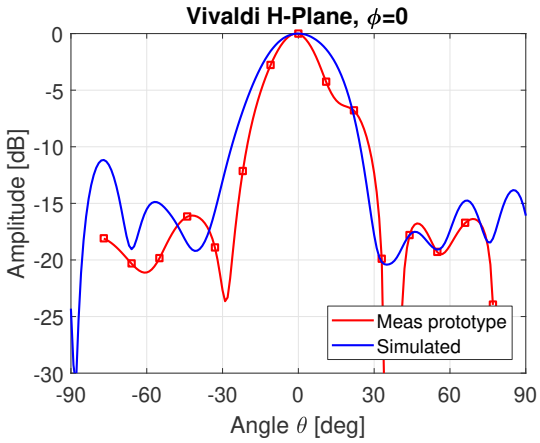

(d) The measured H-plane of a standalone Vivaldi antenna board, compared to the datasheet specification of a similar horn.

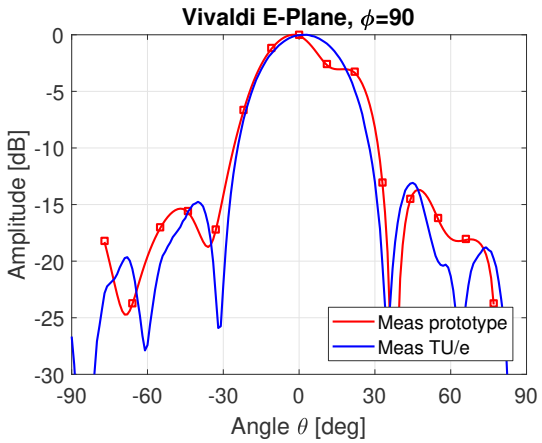

(e) The measured E-plane of a standalone Vivaldi antenna board, compared to the measurement performed on the TU Eindhoven setup.

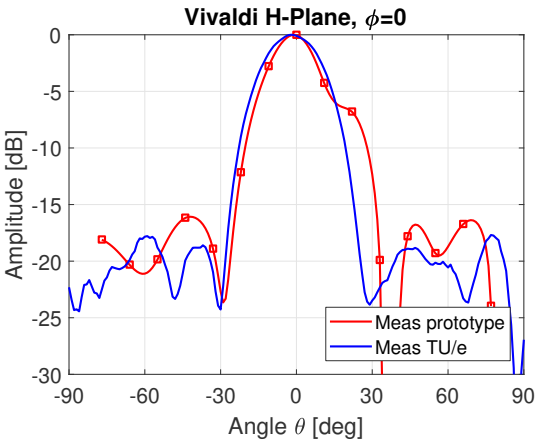

(f) The measured H-plane of a standalone Vivaldi antenna board, compared to the measurement performed on the TU Eindhoven setup.

Figure 5.15: Measured data compared with known values. The red markers on all figures show the measured value and the red line in between is interpolated. They are compared to the blue line which is obtained from other sources. All the datapoints are shown in absolute value.

6

Conclusion

This project served as a pioneering study on the feasibility of a static multi-probe measurement setup. In this process, a variety of aspects for building this setup have been discussed. By analyzing the constraints involved with over-the-air (OTA) testing at mm-wave frequencies, a clear tradeoff between antenna size and measurement chamber size is found. Furthermore, the measurements must be performed in the far field, since a near-field probing setup requires a spatial probe coverage which is unreachable with a fixed array and requires complex values for the measurement points. There is not a universal setup which covers all the needs for an OTA setup since variation in the aperture size, antenna pattern and power levels of the AUT influences measurement properties such as measurement distance, the number of sampling points and powermeter sensitivity. Therefore, a high modularity in the design of the probe points is beneficial for adapting to the measurement needs.

In order to show that measurement of these antenna patterns is possible in the explained conditions, a proof-of-concept measurement setup is developed. This consists of designed high gain Vivaldi antennas with commercial off-the-shelf direct-downconverting RF powermeters which cover a frequency band from 10 GHz to 40 GHz. Two of these antennas, one for each polarization, make up one measurement point. These are mounted on a dome structure, consisting of two arcs, with a variable positioning system. All the acquired datapoints are read out via ADCs and a custom SPI bus, making real-time readout on a PC possible without the need of any high-cost instruments.

The setup is capable of acquiring a radiation pattern within one second. Without any form of calibration, a reasonable antenna pattern reconstruction is found, even though some parts of the antenna pattern are below the detectable range of the used powermeter.

There are a few publications related to building a multi-probe setup for OTA characterization setups. However, from a measurement point of view, these all show fundamental differences with the developed

setup. To begin with, all these studies make use of a VNA to which the multiple probes are multiplexed, which makes the setup very expensive. Furthermore, the setups do not offer the level of flexibility in configuring the setup that the prototype has.

The performed research serves as a solid foundation for reconfigurable, high speed and low cost characterization of mm-wave antenna systems. With the development of the presented setup as a proof-of-concept, the development of a fully developed measurement setup shows great potential for a big innovation in rapid development of new devices for the upcoming 5G standard, such that the predicted antenna measurement bottleneck for 5G testing systems is reduced.

6.1. Future Work

Achieving a properly functioning prototype is an important milestone for continuing research on this topic. By making the well-considered choices, the measurement setup could be fully realized within the thesis period. In the process of developing this prototype, there have been made intentional shortcuts in order to keep the focus on realizing a working setup. This leaves space for an increase in measurement accuracy in many different aspects. A selection of possible improvements is discussed here.

- **Detector improvement:** On the RF Analog Design part, a higher dynamic range powerdetector could be designed such that a larger range of the radiation pattern can be mapped and a broader range of power levels is visible. Alternatively, other properties apart from RMS power could be measured, such as signal phase, instantaneous EVM or interference ruggedness. More complex measurements could be placed on a single point only, such as the position where the main beam is expected.

- **Physical setup:** Regarding the geometry of the measurement setup, an extension of the dual-arc setup to a fully covered semi-sphere could be produced, such that real 3D radiation pattern generation is possible. This includes analysis of efficient sensing probe distribution and practical mounting structures. Alternatively, possibilities for verification of known antenna patterns by using a minimal number of sampling points can be researched. This could be interesting for verification of mass produced devices where a further reduction in cost would be interesting.

- **Antenna design:** In terms of antenna design, a dual-polarized probe antenna setup with the phase centers of both polarizations at the same physical position would be benificial for measurement accuracy, in contrast with the current offset of approximately 2°. Alternatively, these offsets could be taken into account for reconstruction such that this could not result in a measurement error.

- **Calibration procedure:** The current setup does not include any form of calibration; the values that are read from the powermeters are used as a result, without any form of compensation. This already shows that the setup is able to resemble patterns as is. To get the setup close to the level

of accuracy that instruments such a VNA offer, a calibration procedure is recommended. In the most simple form, this could consist of a responsivity calibration, where every antenna is placed in a test fixture with a well-known source transmitting power. By the generation of a lookup-table (LUT), many of the fabrication inaccuracies can already be compensated for. Alternatively, an on-board calibration procedure could be performed in which the powermeter switches to a known source.

- **Reconstruction:** Finally, regarding the radiation pattern reconstruction, more effective options for interpolation could potentially improve measurement accuracy without adding extra points. It might be possible that certain assumptions can be taken on the shape of a particular antenna type to realize this.

Bibliography

[1] I. Cisco Systems, “Cisco Visual Networking Index: Forecast and Trends, 2017–2022,” 2019.

[2] R. N. Clarke, “Expanding mobile wireless capacity: The challenges presented by technology and economics,” *Telecomm. Policy*, vol. 38, no. 8-9, pp. 693–708, 2014.

[3] M. J. Marcus, “5G and ’IMT for 2020 and beyond’ [Spectrum Policy and Regulatory Issues],” *IEEE Wirel. Commun.*, vol. 22, no. 4, pp. 2–3, 2015.

[4] D. H. Archer and M. J. Maybell, “Rotman Lens Development History at Raytheon Electronic Warfare Systems 1967-1995,” *IEEE Antennas Propag. Soc. Int. Symp.*, pp. 31–34, 2005.

[5] O. G. Vendik and Y. V. Yegorov, “The first phased-array antennas in Russia: 1955-1960,” *IEEE Antennas Propag. Mag.*, vol. 42, no. 4, pp. 46–52, 2000.

[6] A. Jain, “Radar for Global Oceanography,” *IEEE Trans. Antennas Propag.*, vol. AP-27, no. 4, pp. 535–538, 1979.

[7] A. I. Zaghloul, Y. Hwang, R. M. Sorbello, and F. T. Assal, “Advances in Multibeam Communications Satellite Antennas,” *Proc. IEEE*, vol. 78, no. 7, pp. 1214–1232, 1990.

[8] W. Hong, Z. H. Jiang *et al.*, “Multibeam Antenna Technologies for 5G Wireless Communications,” *IEEE Trans. Antennas Propag.*, vol. 65, no. 12, pp. 6231–6249, 2017.

[9] J. S. Herd and M. David Conway, “The Evolution to Modern Phased Array Architectures,” *Proc. IEEE*, vol. 104, no. 3, pp. 519–529, 2016.

[10] S. Han, C. L. I, Z. Xu, and C. Rowell, “Large-scale antenna systems with hybrid analog and digital beamforming for millimeter wave 5G,” *IEEE Commun. Mag.*, vol. 53, no. 1, pp. 186–194, 2015.

[11] D. C. Kim, S. J. Park, T. W. Kim, L. Minz, and S. O. Park, “Fully Digital Beamforming Receiver with a Real-Time Calibration for 5G Mobile Communication,” *IEEE Trans. Antennas Propag.*, vol. 67, no. 6, pp. 3809–3819, 2019.

[12] K. A. Remley, J. A. Gordon *et al.*, “Measurement Challenges for 5G and Beyond,” *IEEE Microw. Mag.*, vol. 18, no. 5, pp. 41–56, 2017.

[13] “NSI-MI Technologies.” [Online]. Available: https://www.nsi-mi.com/

[14] J. A. Gordon, D. R. Novotny *et al.*, “Millimeter-Wave Near-Field Measurements Using Coordinated Robotics,” *IEEE Trans. Antennas Propag.*, vol. 63, no. 12, pp. 5351–5362, 2015.

[15] E. McCune, *Practical Digital Wireless Signals*. Cambridge: Cambridge University Press, 2010. [Online]. Available: http://ebooks.cambridge.org/ref/id/CBO9780511674648

[16] H. T. Friis, “Noise Figures of Radio Receivers,” *Proc. IRE*, vol. 32, no. 7, pp. 419–422, 1944.

[17] IEEE Antennas and Propagation Society, “IEEE Standard for Definitions of Terms for Antennas,” *IEEE Std 145-2013*, vol. 2013, p. 50, 2014.

[18] C. A. Balanis, *Antenna Theory: Analysis and Design*. John Wiley & Sons, 2005.

[19] F. Ulaby, E. Michielssen, and U. Ravaioli, *Fundamentals of Applied Electromagnetics*, 7th ed., 2015.

[20] Keysight, “OTA Test for Millimeter-Wave 5G NR Devices and Systems - White Paper,” 2018.

[21] D. M. Pozar, *Microwave Engineering*. John Wiley & Sons, 2009.

[22] “IEEE Standard Test Procedures for Antennas,” *ANSI/IEEE Std 149-1979, Reaffirmed 2008(R2008)*, 1979.

[23] D. T. Paris, W. M. Leach, and E. B. Joy, “Basic Theory of Probe-Compensated Near-Field Measurements,” *IEEE Trans. Antennas Propag.*, vol. 26, no. 3, pp. 373–379, 1978.

[24] A. D. Yaghjian, “An Overview of Near-Field Antenna Measurements,” *IEEE Trans. Antennas Propag.*, vol. 34, no. 1, pp. 30–45, 1986.

[25] R. Johnson, H. Ecker, and J. Hollis, “Determination of far-field antenna patterns from near-field measurements,” *Proc. IEEE*, vol. 61, no. 12, pp. 1668–1694, 2008.

[26] M. Alonso-Delpino, M. D. Rosa, M. Simeoni, M. Spella, C. De Martino, and M. Spirito, “A planar near-field setup for millimeter-wave system-embedded antenna testing,” *IEEE Antennas Wirel. Propag. Lett.*, vol. 16, no. 8, pp. 83–86, 2017.

[27] R. G. Yaccarino and Y. Rahmat-Samii, “Phaseless bi-polar planar near-field measurements and diagnostics of array antennas,” *IEEE Trans. Antennas Propag.*, vol. 47, no. 3, pp. 574–583, 1999.

[28] 3GPP, “TR 38.810; NR; Study on test methods,” Tech. Rep. 38.810, 2019. [Online]. Available: https://portal.3gpp.org/desktopmodules/Specifications/SpecificationDetails.aspx?specificationId=3218

[29] H.-j. Steiner, T. Fritzel, A. Geise, C. Schmidt, and M. Paquay, “First results of innovative Mobile Near-Field Antenna Measurement System for extreme large DUTs,” in *2015 9th Eur. Conf. Antennas Propag.*, 2015, pp. 1–5.

[30] A. Geise, T. Fritzel, and M. Paquay, “Ka-band measurement results of the irregular near-field scanning system PAMS,” in *Proc. 2017 Antenna Meas. Tech. Assoc. Symp.*, 2017.

[31] Z. M. Tsai, Y. C. Wu, S. Y. Chen, T. Lee, and H. Wang, “A V-band on-wafer near-field antenna measurement system using an IC probe station,” *IEEE Trans. Antennas Propag.*, vol. 61, no. 4, pp. 2058–2067, 2013.

[32] D. Titz, F. Ferrero, C. Luxey, and G. Jacquemod, “Measurement Setup for 60 GHz Probe-fed Antennas,” pp. 3121–3124, 2011.

[33] K. Van Caekenberghe, K. M. Brakora *et al.*, “A 2-40 GHz probe station based setup for on-wafer antenna measurements,” *IEEE Trans. Antennas Propag.*, vol. 56, no. 10, pp. 3241–3247, 2008.

[34] A. C. Reniers and A. B. Smolders, “Guidelines for millimeter-wave antenna measurements,” *2018 IEEE Conf. Antenna Meas. Appl. CAMA 2018*, pp. 1–4, 2018.

[35] K. Kibaroglu, M. Sayginer, and G. M. Rebeiz, “A Low-Cost Scalable 32-Element 28-GHz Phased Array Transceiver for 5G Communication Links Based on a Beamformer Flip-Chip Unit Cell,” *IEEE J. Solid-State Circuits*, vol. 53, no. 5, pp. 1260–1274, 2018.

[36] B. Sadhu, Y. Tousi *et al.*, “A 28-GHz 32-Element TRX Phased-Array IC with Concurrent Dual-Polarized Operation and Orthogonal Phase and Gain Control for 5G Communications,” *IEEE J. Solid-State Circuits*, vol. 52, no. 12, pp. 3373–3391, 2017.

[37] H. T. Kim, B. S. Park *et al.*, “A 28-GHz CMOS Direct Conversion Transceiver with 2x4 Antenna Array for 5G Cellular System,” *IEEE J. Solid-State Circuits*, vol. 53, no. 5, pp. 1245–1259, 2018.

[38] S. Zihir, O. D. Gurbuz, A. Kar-Roy, S. Raman, and G. M. Rebeiz, “60-GHz 64- and 256-elements wafer-scale phased-array transmitters using full-reticle and subreticle stitching techniques,” *IEEE Trans. Microw. Theory Tech.*, vol. 64, no. 12, pp. 4701–4719, 2016.

[39] T. Sowlati, S. Sarkar *et al.*, “A 60-GHz 144-Element Phased-Array Transceiver for Backhaul Application,” *IEEE J. Solid-State Circuits*, vol. 53, no. 12, pp. 3640–3659, 2018.

[40] T. A. Laitinen, C. Icheln, and P. Vainikainen, “Rapid Spherical 3-D Field Measurement System for Mobile Terminal Antennas,” *Proc. 20th IEEE Instrum. Technol. Conf.*, pp. 20–22, 2003.

[41] L. J. Foged, L. Duchesne, L. Durand, F. Herbiniere, and N. Gross, “Small antenna measurements in spherical nearfield systems,” *2nd Eur. Conf. Antennas Propag. (EuCAP 2007)*, p. 593, 2007.

[42] W. Fan, J. O. Nielsen *et al.*, “Antenna pattern impact on MIMO OTA testing,” *IEEE Trans. Antennas Propag.*, vol. 61, no. 11, pp. 5714–5723, 2013.

[43] W. Fan, J. O. Nielsen, and G. F. Pedersen, “Estimating discrete power angular spectra in multi-probe OTA setups,” *IEEE Antennas Wirel. Propag. Lett.*, vol. 13, pp. 349–352, 2014.

[44] P. Gibson, “The Vivaldi Aerial,” *1979 9th Eur. Microw. Conf.*, pp. 101–105, 2007.

[45] J. Shin and D. H. Schaubert, “A parameter study of stripline-fed vivaldi notch-antenna arrays,” *IEEE Trans. Antennas Propag.*, vol. 47, no. 5, pp. 879–886, 1999.

[46] M. Moosazadeh and S. Kharkovsky, “A Compact High-Gain and Front-to-Back Ratio Elliptically Tapered Antipodal Vivaldi Antenna With Trapezoid-Shaped Dielectric Lens,” *IEEE Antennas Wirel. Propag. Lett.*, vol. 15, pp. 552–555, 2016.

[47] A. M. De Oliveira, M. B. Perotoni, S. T. Kofuji, and J. F. Justo, “A palm tree Antipodal Vivaldi Antenna with exponential slot edge for improved radiation pattern,” *IEEE Antennas Wirel. Propag. Lett.*, vol. 14, pp. 1334–1337, 2015.

[48] M. H. Hoang, K. Yang, M. John, P. McEvoy, and M. Ammann, “Ka-band vivaldi antenna with novel core element for high-gain,” *IET Conf. Publ.*, vol. 2017, no. CP732, pp. 2–5, 2017.

[49] B. Biswas, R. Ghatak, and D. R. Poddar, “A Fern Fractal Leaf Inspired Wideband Antipodal Vivaldi Antenna for Microwave Imaging System,” *IEEE Trans. Antennas Propag.*, vol. 65, no. 11, pp. 6126–6129, 2017.

[50] D. K. Chandrappa and A.-R. Sebak, “Design of High-Gain Ka-Band Antipodal Vivaldi Antenna excited by Printed Ridge Gap Waveguide,” *2018 18th Int. Symp. Antenna Technol. Appl. Electromagn.*, vol. 0, pp. 1–2, 2019.

[51] L. Guo and Y. F. Qiang, “Design of a Compact Wideband Dual-Polarization Antipodal Vivaldi Antenna Array,” *2018 IEEE Int. Conf. Comput. Electromagn. ICCEM 2018*, pp. 1–3, 2018.

[52] E. W. Reid, L. Ortiz-Balbuena, A. Ghadiri, and K. Moez, “A 324-element vivaldi antenna array for radio astronomy instrumentation,” *IEEE Trans. Instrum. Meas.*, vol. 61, no. 1, pp. 241–250, 2012.

[53] D. H. Schaubert and T.-H. Chio, “Wideband Vivaldi Arrays for Large Aperture Antennas,” *Perspect. Radio Astron. Technol. Large Antenna Arrays*, pp. 49–57, 1999.

[54] J. T. Case, M. Moosazadeh, and S. Kharkovsky, “Microwave and millimetre wave antipodal Vivaldi antenna with trapezoid-shaped dielectric lens for imaging of construction materials,” *IET Microwaves, Antennas Propag.*, vol. 10, no. 3, pp. 301–309, 2015.

[55] “ARM - Mbed.” [Online]. Available: mbed.com

A

Board Designs

A.1. Vivaldi Standalone Antenna Board Layout

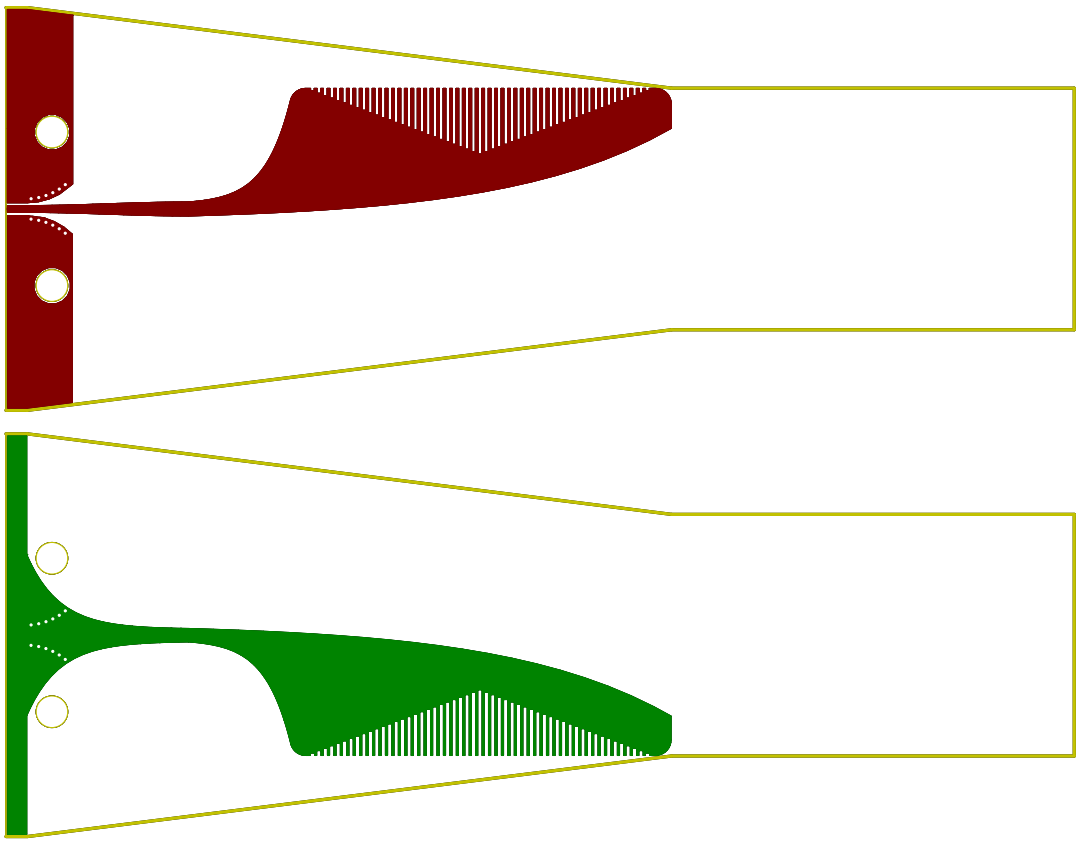

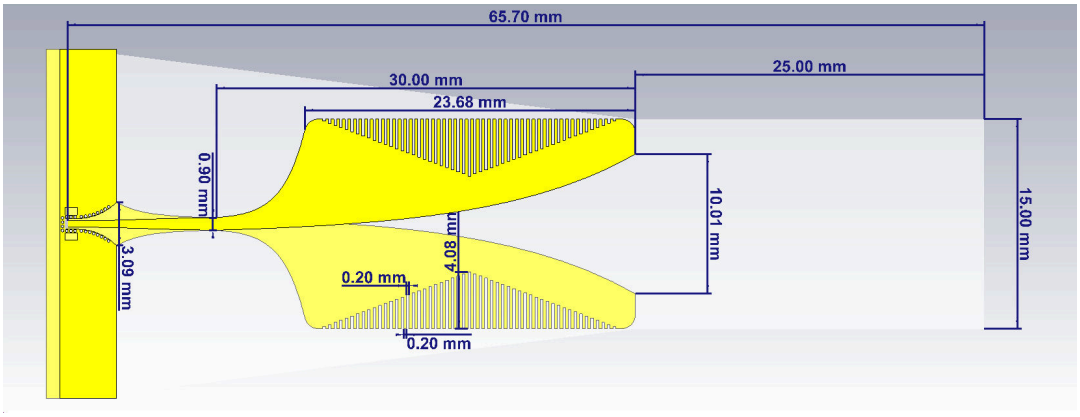
65.70 mm
30.00 mm
25.00 mm
23.68 mm
0.90 mm
10.01 mm
15.00 mm
3.09 mm
4.08 mm
0.20 mm
0.20 mm

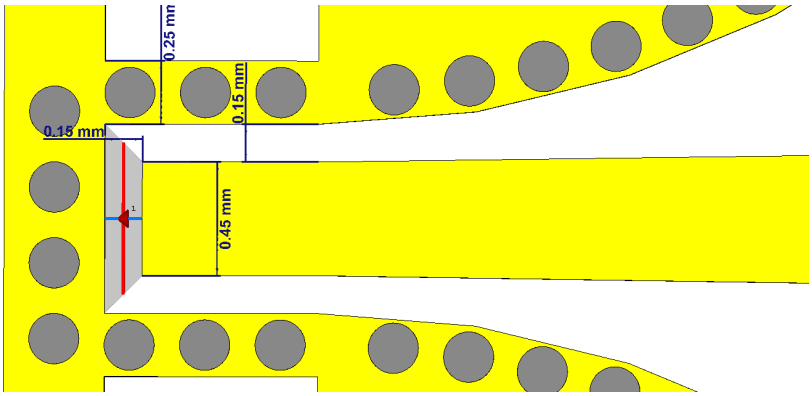
0.25 mm
0.15 mm
0.15 mm
0.45 mm

A.2. Full Powermeter Board Design

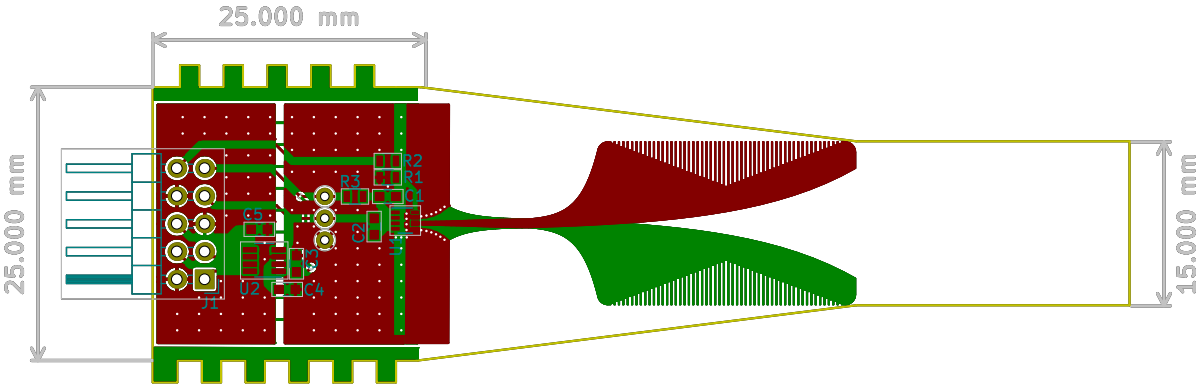

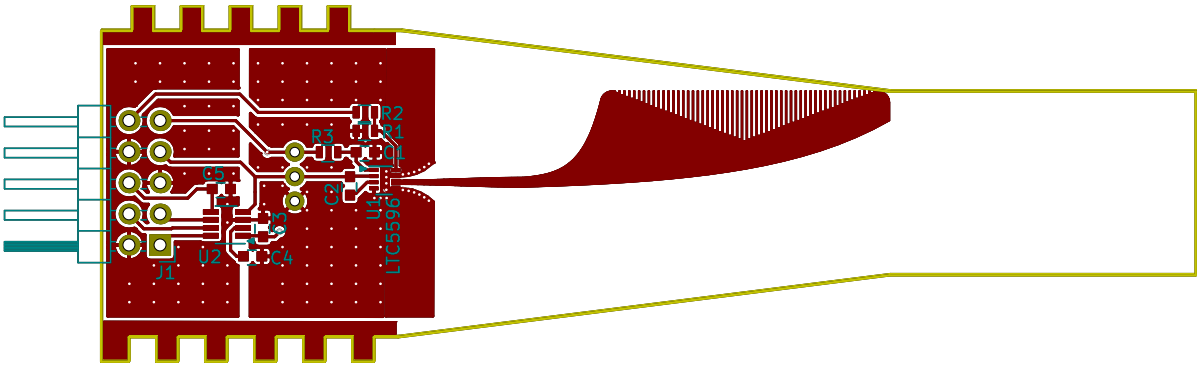

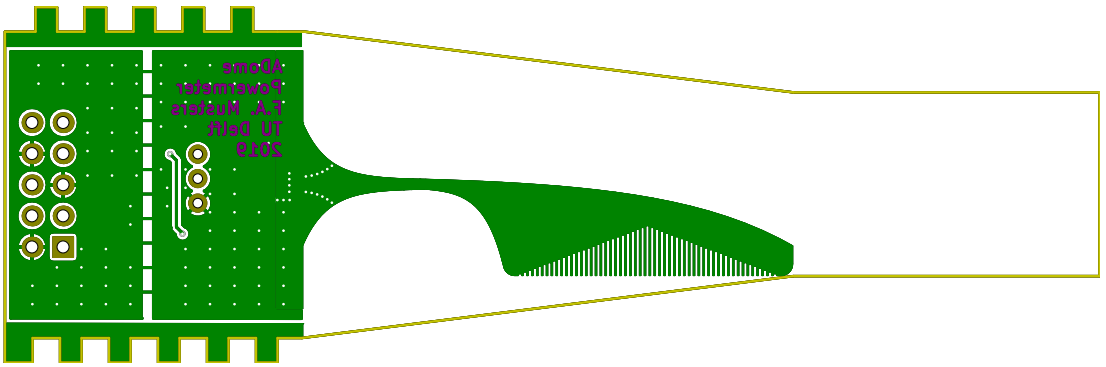

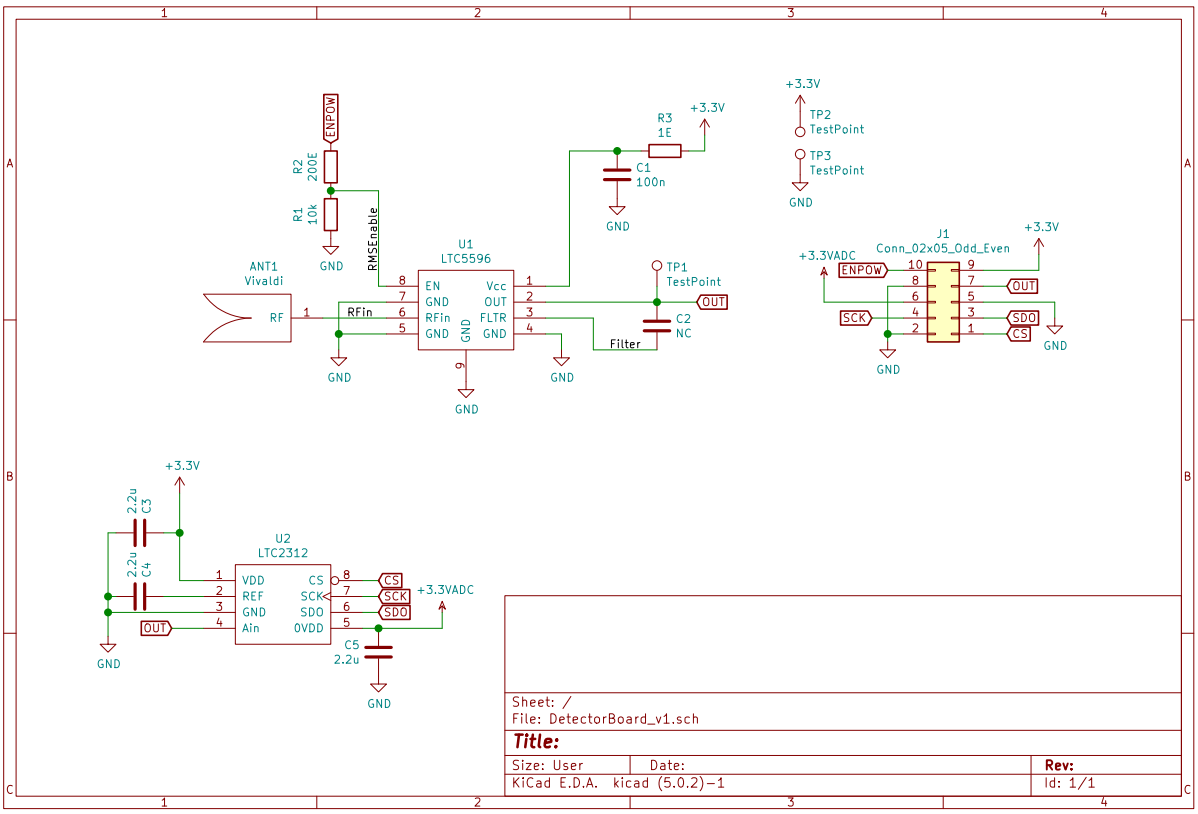
ENPOW
R2
200E
R1
10k
GND
RMSEnable
U1
LTC5596
ANT1
Vivaldi
RF
RFin
EN
GND
RFin
GND
Vcc
OUT
FLTR
GND
GND
GND
GND
R3
1E
+3.3V
C1
100n
GND
TP1
TestPoint
OUT
C2
NC
Filter
GND
+3.3V
TP2
TestPoint
TP3
TestPoint
GND
J1
Conn_02x05_Odd_Even
+3.3VADC
ENPOW
SCK
OUT
SDO
CS
+3.3V
GND
GND
+3.3V
2.2u
C3
2.2u
C4
U2
LTC2312
VDD
REF
GND
Ain
CS
SCK
SDO
OVDD
CS
SCK
SDO
+3.3VADC
OUT
C5
2.2u
GND
Sheet: /
File: DetectorBoard_v1.sch
Title:
Size: User
Date:
Rev:
KiCad E.D.A. kicad (5.0.2)-1
Id: 1/1

A.3. Parentboard Design

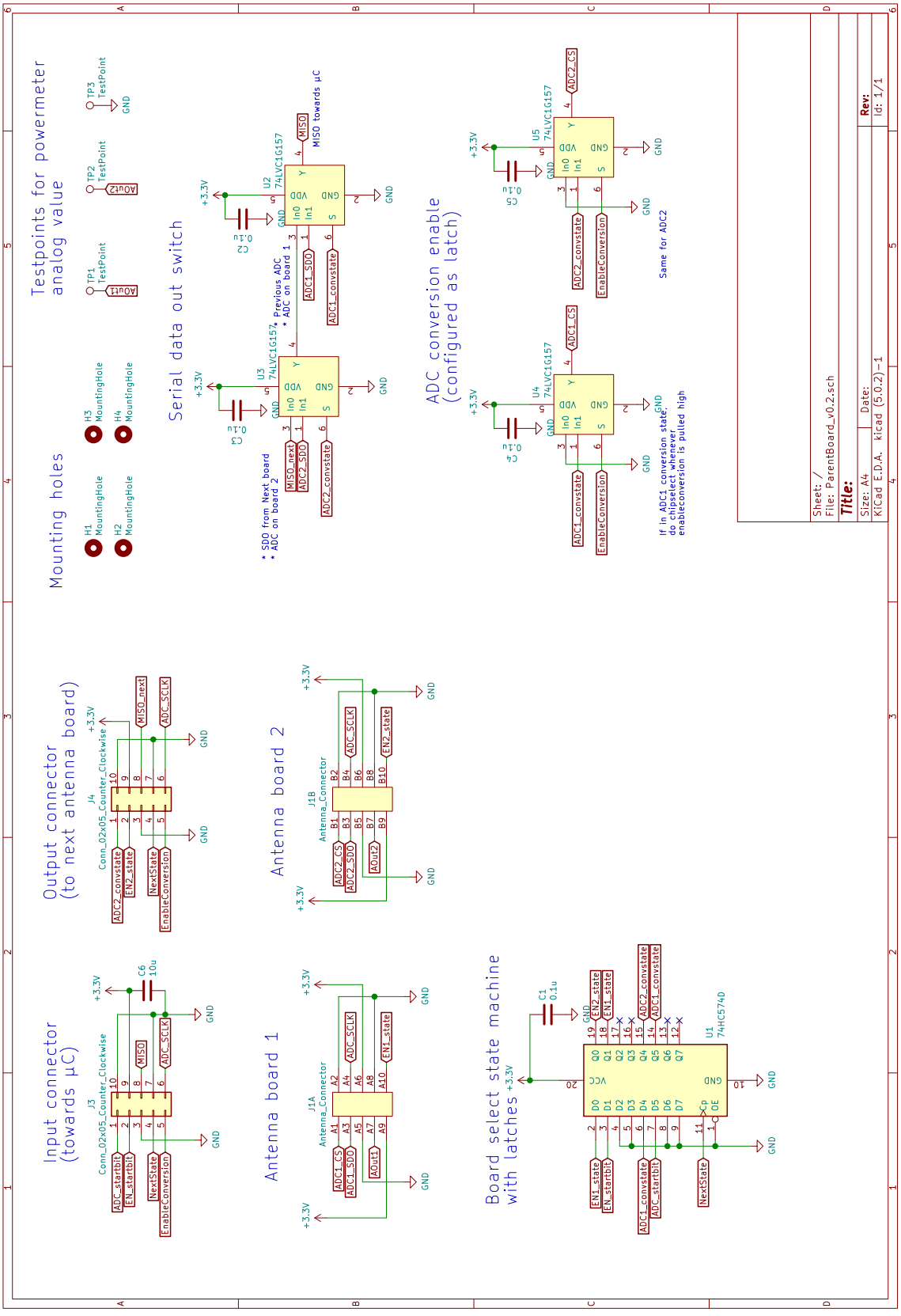

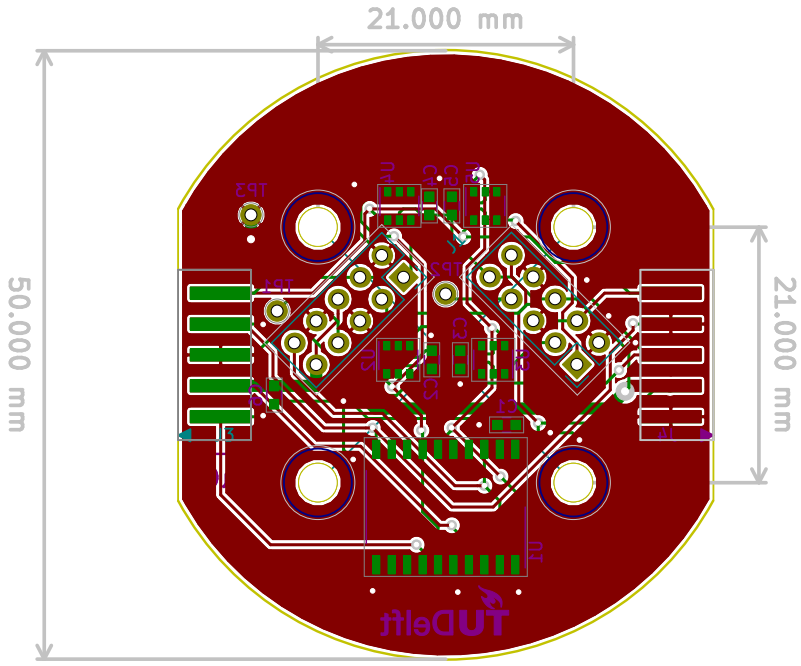
21.000 mm
50.000 mm
21.000 mm
TUDelft

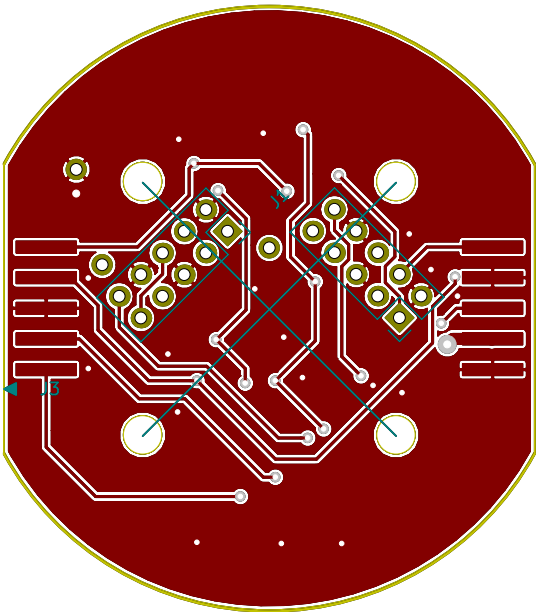

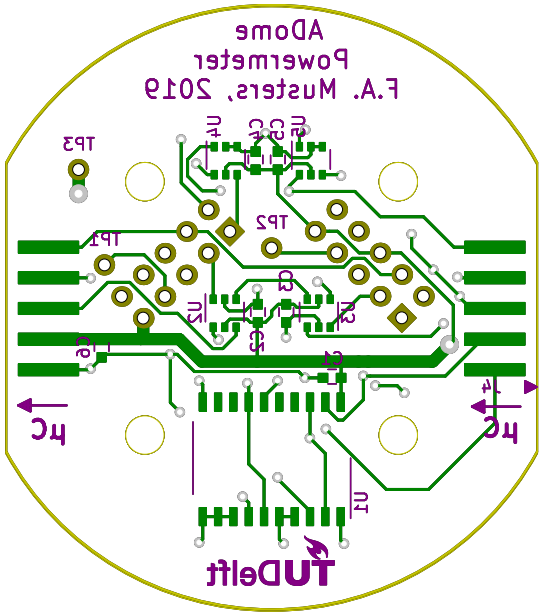
ADome
Powermeter
F.A. Musters, 2019
I²C
I²C
TUDelft

Parentboard sampling readout

Timing diagram

Ferry Musters - May 2019 - TU Delft

	Comm state:	Bitshift ADC state	Enable ADC1 conv	Read ADC1	Shift to ADC2	Enable ADC2 conv	Read ADC2	Goto next board		
	ADC selection:								**To next?**	**Next board input:**
	PWRMTR_startbit	1	0	0	0	0	0	0		
	ADC_startbit	1	0	0	0	0	0	0		
	nextstate	1	0	0	0	0	1	0	OUT→	ADC_nextstate
	State_ADCconv1	0	1	1	1	1	1	0		
	State_PWRMTR1	0	1	1	1	1	1	0		
	State_ADCconv2	0	0	0	0	0	0	1	OUT→	ADC_startbit
	State_PWRMTR2	0	0	0	0	0	0	1	OUT→	PWRMTR_startbit
	SPI Readout:									
Min 1.2ns	ADC_ENA_CONV	0	0	0	1	0	0	0	OUT→	ADC_ENA_CONV
Pulse 12x	ADC_SPI_CLK	0	0	0	X	X	0	0	OUT→	ADC_SPI_CLK
12 bits	ADC_SPI_MISO	0	0	0	X	X	0	0	← IN	ADC_SPI_MISO

A.4. Bill of Materials

Bill Of Materials - Adome thesis demonstrator

Ferry Musters, TU Delft, June 2019

Prices are an indication, actual prices will vary slightly

2 Arcs

15 *Sampling points per arc*

29 Total sampling points (all arcs)

10% Extra pieces

64 Total antenna boards (2 per sampler

Vivaldi detector board

Mouser	Manufacturer	Component	Description	Qty	Qty Total	Price/pc	Cost
	Eurocircuits	*PCB*	RF pool RO4350 0.5mm thick	1	64	€ 7.19	
584-LTC5596IDCTRMPBF	Analog Devices	LTC5596IDC#TRMPBF	RMS powermeter 40GHz 35dB DR	1	64	€ 49.44	€ 3,164.16
584-C2312CTS8-12TMPF	Analog Devices	LTC2312CTS8-12#TRMPBF	ADC 12-bit 500ksps SOT-32	1	64	€ 3.14	€ 200.96
200-TSW10508FDRA	Samtech	TSW-105-08-F-D-RA	Male header 2.52mm 2Row 10Pin (2x5) angled	1	64	€ 0.63	€ 40.19
81-GRM188R61E225KA2J	Murata	GRM188R61E225KA12J	Cap MLCC 2.2uF 0603	3	200	€ 0.06	€ 11.00
581-06033G104Z	AVX	06033G104ZAT2A	Cap MLCC 0.1uF +- 0.1pF 25V 0603	1	100	€ 0.06	€ 6.30
603-RC0603FR-071RP	Yageo	RC0603FR-071RP	Res 1Ohm 1% 0603	1	100	€ 0.02	€ 1.60
603-AC0603FR-07200RL	Yageo	AC0603FR-07200RL	Res 200Ohm 1% 0603	1	100	€ 0.01	€ 0.70
603-RC0603FR-0710KL	Yageo	RC0603FR-0710KL	Res 10kOhm 1% 0603	1	100	€ 0.01	€ 0.50
						Total	**€ 3,425**

Antenna Parentboard

32 Boards total

Mouser	Manufacturer	Component	Description	Qty	Qty Total	Price/pc	Cost
	Eurocircuits	*PCB*	PCB standard pool FR-4 1.55mm thick	1	32	€ 3.42	
771-74HC574D-T	Nexperia	74HC574D	Octal D-type flip-flop; positive edge-trigger; 3-state	1	32	€ 0.39	€ 12.58
771-74LVC1G157GV-G	Nexperia	74LVC1G157GV	Single 2-input multiplexer	4	128	€ 0.31	€ 39.17
710-61301021821	Würth	61301021821	Female header 2.52mm 2x5 pins	2	64	€ 0.68	€ 43.52
710-61201021621	Würth	61201021621	Male header 2.54mm Shrouded 10Pin (2x5) Straight	2	64	€ 0.48	€ 30.72
710-61201023021	Würth	61201023021	Connector Female IDC 10pin (2x5)	2	64	€ 0.41	€ 26.24
517-3365/10FT	3M Electronic	3365/10-CUT-LENGTH	Flat Cables .050 10 COND. 28AWG ROUND 1PC=1FT	1	32	€ 0.31	€ 9.79
80-C0805C106K8P	Kemet	C0603C106M8PACTU	Cap MLCC 10uF 10VDC X5R 0603 20%	1	32	€ 0.16	€ 5.02
581-06033G104Z	AVX	06033G104ZAT2A	Cap MLCC .1uF 25V Y5V 0603	5	160	€ 0.09	€ 13.92
749-SRS-4-410	Bivar	SRS-4-410	Spacer PVC M3, 0.41inch (1.04cm)	4	128	€ 0.10	€ 12.29
						Total	**€ 193**

Microcontroller board

2 Boards total

Mouser	Manufacturer	Component	Description	Qty	Qty Total	Price/pc	Cost
	Eurocircuits	*PCB*	PCB proto pool FR-4 1.55mm thick	1	2	€ 31.03	
511-NUCLEO-L432KC	STMicroelectronic	NUCLEO-L432KC	ARM STM32 Nucleo-32 dev board STM32L432KC	1	2	€ 9.37	€ 18.74
511-NUCLEO-L476RG	STMicroelectronic	NUCLEO-L476RG	ARM STM32 Nucleo-64 dev board STM32L476RG	1	2	€ 12.71	€ 25.42
709-GST25E12-P1J	Mean Well	GST25E12-P1J	Wall Mount AC Adapter 25W 12V 2.08A Euro plug		1	€ 13.68	€ 13.68
701-SPX29300T-L-33TR	MaxLinear	SPX29300T-L-3-3/TR	LDO Voltage Regulators 3A LOW DROPOUT 3.3V	1	2	€ 1.54	€ 3.08
80-C0805C106K8P	Kemet	C0603C106M8PACTU	Cap MLCC 10uF 10VDC X5R 0603 20%	2	4	€ 0.16	€ 0.63
710-61201021621	Würth	61201021621	Male header 2.54mm Shrouded 10Pin (2x5) Straight	1	2	€ 0.48	€ 0.96
992-15FX1-254MM	Gravitech	15Fx1-254mm	2.54MM 0.1" 15-PIN FEMALE HEADER	2	4	€ 1.06	€ 4.24
517-929400-01-36-RK	3M Electronic	929400-01-36-RK	Headers FULL STICK HDR/36POS/1ROW	1	2	€ 2.24	€ 4.48
490-PJ-036AH-SMT-TR	CUI	PJ-036AH-SMT-TR	DC Power Connectors Power Jacks	1	2	€ 1.19	€ 2.38
854-KIT-ZW-20X3	BusBoard	KIT-ZW-20x3	Jumper Wires ZIPWIRE KIT 20cm 120 WIRES ASSORTED		1	€ 13.33	€ 13.33
						Total	**€ 87**

Grand total **€ 3,706**

B

Software for Protoype Readout

B.1. Microcontroller Code

```
/// **** TUD_ADome_Full_Readout ****
/// Readout procedure for chain or pwoerdetector boards for the ADome project.
/// Built for STM32Nucleo boards on arduino nano or uno headers
/// Based on chain of LTC5596 powermeters and LTC2312 12/14-bit ADC with
/// custom readout logic to chain the SPI(ish) communcation protocol of ADC.
///
/// F.A. Musters 2019

#include "mbed.h"
#include <string>

// Pin definitions
DigitalIn miso(D3);
DigitalOut sclk(D4);
DigitalOut EnableConversion(D5);
DigitalOut NextState(D6);

DigitalOut PowermeterStartbit(D9);
DigitalOut ADCStartbit(D10);

Serial pc(SERIAL_TX, SERIAL_RX, 115200);
DigitalOut nucleoled(LED1);

Timer t;
int timeOfLastSample = 0;

// Set conversion variables
const float vref = 2.048; //ADC reference voltage (full ADC code is this voltage)
const int ADC_bits = 12; //number of ADC bits to convert back
int movingaveragesize = 1; // Average the read value with X size

int numOfBoards = 1; //can be varied by input
int sampleDelayUs = 10; // can be varied by input
float movingaverage[100]; //averaged sample values antennas

//Define function handles, implemented after main
void init();
void sendShiftStartbits();
void selectNextAntenna();
void performADCConversion();
int readADCBits();
```

```
float countsToVoltage(float);
void updateSerialCommunication();

// MAIN
int main()
{
    init();
    t.start();

    while(true) {
        //start shift register from beginning to measure first board
        sendShiftStartbits();
        t.reset(); //start at 0 to avoid overflowing
        timeOfLastSample = 0;
        // Read out every board
        int currentboard = 0;

        while(currentboard < numOfBoards*2) {
            //make sure the current board is enabled long enough. If so, readout
            if( t.read_us() - timeOfLastSample > sampleDelayUs) {
                int adc_single = readADCBits(); // Read out 12 or 14 bits value from adc
                    of both antennas
                timeOfLastSample = t.read_us();
                movingaverage[currentboard] = movingaverage[currentboard] * (1- 1/(float)
                    movingaveragesize) + (float)adc_single / (float)movingaveragesize;
                currentboard++;
                selectNextAntenna(); //move readout shift register to next antenna
            }
            //wait_us(sampleDelayUs); // Wait a 'long' time to stabilize next device.
            updateSerialCommunication(); //Check on any received commands
        }
    }
}

// SUBFUNCTIONS

void init()
{
    // Make sure signals are low at beginning
    sclk = 0;
    EnableConversion = 0;
    NextState = 0;
    PowermeterStartbit = 0;
    ADCStartbit = 0;
}

// Send out the Startbit for both the ADC readout and the powermeter enable
// This works as a shift register, thus every 'NextState' pulse will move it
// to the next device to read it out
void sendShiftStartbits()
{
    // Old devices could still be on, first clear out any old points
    // by pulsing next state often (shift register)
    //for(int i = 0; i < 200; i++){
    //    selectNextAntenna();
    //}

    // Now, actually start sending the start bits on the shift register
    //set bits high on GPIO
    ADCStartbit = 1;
    PowermeterStartbit = 1;
    //Give pulse to shift register GPIO
    selectNextAntenna();
    //set bits low on GPIO
    ADCStartbit = 0;
    PowermeterStartbit = 0;
    wait_us(1);
}

void selectNextAntenna()
{
    //Give pulse on GPIO (high then low)
    NextState = 1;
    wait_us(1);
    NextState = 0;
    wait_us(1);
}
```

```
// Perform conversion by raising chip select / conversion pin
// Give pulse and wait short time to allow conversion (min 1.4 ns)
void performADCConversion()
{
    EnableConversion = 1;
    wait_us(1);
    EnableConversion = 0;
    wait_us(1);
}

int readADCBits()
{
    performADCConversion();
    // Read out all the bits one by one by pulsing SCLK and readout on MISO
    int adc_read_value = 0;
    for(int i=0; i<ADC_bits ; i++) {
        sclk = 1; //serial clock is global for all boards
        adc_read_value += (miso > 0) << (ADC_bits  - i - 1);
        sclk = 0;
    }
    return adc_read_value;
}

float countsToVoltage(float counts)
{
    // This calculates the input as a fraction of the reference voltage (dimensionless)
    float voltage = counts / ((1 << ADC_bits) -1);
    // Multiply fraction by Vref to get the actual voltage at the input (in volts)
    voltage = voltage * vref;
    return voltage;
}

void updateSerialCommunication()
{
    bool measureFlag = false; //Flag to indicate if measure command is received

    if(pc.readable()) { //If something is received, handle the command
        char command = ' ';
        int value = 0;
        pc.scanf("%c", &command);
        pc.scanf("%d", &value); //pc.printf("%c %d\r\n", command, value)

        if(command == 'm' || command == 'M') measureFlag = true; // Readout value
        if(command == 'b' || command == 'B') numOfBoards = value; // set Boards
        if(command == 'd' || command == 'D') sampleDelayUs = value; // set sample delay
            time
        if(command == 'a' || command == 'A') movingaveragesize = value; // set sample
            delay time
    }

    if(measureFlag) {
        measureFlag = false; //handled flag
        nucleoled = !nucleoled; //toggle LED to indicate readout
        char outtext[1000] = "";
        for(int i=0; i<numOfBoards*2; i++) {
            char str[100] = "";
            float voltage = countsToVoltage(movingaverage[i]);
            sprintf(str, "%3.4f, ", voltage);
            strcat(outtext, str);
        }
        pc.printf("%s\r\n",outtext);
        //pc.printf("%3.4f, %3.4f, %3.4f, %3.4f\r\n", voltage[0], voltage[1], voltage[2],
            voltage[3]);
    }
}
```